

OPTICAL AND THERMAL DYNAMICS OF LONG WAVE QUANTUM CASCADE LASERS

A DISSERTATION SUBMITTED TO
THE GRADUATE SCHOOL OF ENGINEERING AND SCIENCE
OF BILKENT UNIVERSITY
IN PARTIAL FULFILLMENT OF THE REQUIREMENTS FOR
THE DEGREE OF
DOCTOR OF PHILOSOPHY
IN
PHYSICS

By
Sinan Gündoğdu
September 2018

Optical and thermal dynamics of long wave quantum cascade lasers

By Sinan Gündođdu

September 2018

We certify that we have read this dissertation and that in our opinion it is fully adequate, in scope and in quality, as a dissertation for the degree of Doctor of Philosophy.

Ođuz Gölseren(Advisor)

Atilla Aydınlı (Co-Advisor)

Mehmet Parlak

Ceyhun Bulutay

Onur Tokel

Rařit Turan

Approved for the Graduate School of Engineering and Science:

Ezhan Karařan
Director of the Graduate School

ABSTRACT

OPTICAL AND THERMAL DYNAMICS OF LONG WAVE QUANTUM CASCADE LASERS

Sinan Gündoğdu

Ph.D. in Physics

Advisor: Oğuz Gülseren

Co-Advisor: Atilla Aydınli

September 2018

Quantum Cascade Lasers (QCLs) are coherent light sources that make use of intraband transitions of wavefunction engineered semiconductor quantum wells. They have been designed to emit light in a wide spectral range; from mid-wave infrared to terahertz. Long wave QCLs are a subject of interest for some applications such as remote detection of harmful chemicals. These applications demand higher optical powers at room temperature. In this thesis we demonstrate simulation, design, fabrication and characterization of long-wave QCLs that emit light around $9.2\mu m$. To increase optical power and enhance thermal performance, we explore the optical and thermal properties of QCLs. Thermal characteristics of QCLs are analyzed by finite element methods. We developed a spectral technique that relies on analysis of Fabry-Perot modes to measure cavity temperatures experimentally. By combining the simulations and experimental results we scrutinized the thermal properties of QCLs, and estimated the active region thermal conductivity. To increase the optical power, we conducted optical calculations and investigated the sources of loss. As a result of a search for alternative electrical passivation materials, we fabricated HfO_2 passivated lasers and demonstrated about to two-fold reduction in optical loss and increase in optical power.

Keywords: Quantum Cascade Lasers, Semiconductor Lasers.

ÖZET

UZUN DALGABOYLU KUANTUM ÇAĞLAYAN LAZERLERİN OPTİK VE ISIL DİNAMİKLERİ

Sinan Gündoğdu

Fizik, Doktora

Tez Danışmanı: Oğuz Gülseren

İkinci Tez Danışmanı: Atilla Aydınlı

Eylül 2018

Kuantum Çağlayan Lazerler (KÇL'ler) dalga fonksiyonu mühendisliği ile tasarlanmış kuantum kuyularının bant-içi geçişlerinden yararlanan eşevreli ışık kaynaklarıdır. Orta kızılaltından terahertz frekanslarına kadar geniş bir tayfta ışık yayan tasarımlar bulunmaktadır. Uzun dalgaboylu KÇL'ler zararlı kimyasal bileşiklerin uzak mesafeden algılanması gibi bazı uygulama alanlarından dolayı ilgi konusudur. Bu tezde $9.2 \mu m$ civarında ışık yayan uzun dalgaboylu KÇL'lerin simülasyonları, tasarımı, üretimi ve karakterizasyonu gösterilmiştir. Optik gücü arttırmak ve ısıl randımanı iyileştirmek amacıyla KÇL'lerin optik ve ısıl özellikleri incelenmiştir. KÇL'lerin ısıl özellikleri sonlu eleman metodları ile tahlil edilmiştir. KÇL oyuk sıcaklıklarının deneysel olarak ölçülmesi için Fabry-Perot modlarının analizine dayanan tayfölçüm tabanlı bir teknik geliştirilmiştir. Simülasyon ve deneysel sonuçların birleştirilmesi ile KÇL'lerin ısıl özellikleri incelenmiş ve aktif bölgenin ısıl iletkenliği hesaplanmıştır. Optik gücü arttırmak için optik hesaplamalar yapılarak optik kaybın kaynakları araştırılmıştır. Alternatif elektriksel izolasyon malzemelerinin araştırılması sonucunda HfO_2 pasivasyonlu lazerler üzütilmiş, optik kayıpta iki kata yakın azalma ve optik güçte artış gösterilmiştir.

Anahtar sözcükler: Kuantum Çağlayan Lazerler, Yarıiletken Lazerler.

Acknowledgement

In 2012, we found a company, to built medical laser devices. When I worked with a laser diode for the first time, I was unskilled about lasers and optics. At that time, I wished to understand what I was doing and to be able to build a laser from scratch. Atilla Hoca is the one who has made this wish real for me. Even though there were apparent difficulties, he applied for a project for me. He shouldered the burden and responsibility of such an arduous task. I would not achieve this goal if it were not for him. I believe he is a significant contributor to science and technology in Turkey, and I hope he will continue to be so, for a long time.

My long-standing friend and colleague, Seval Arslan, is a vital contributor to this work. She has been a part of this in many aspects, from fabrication to mask design, from measurement to data analysis. She supported me not only regarding experimental work, but also valuable discussions, and her friendship.

I want to thank my friend Dr. Hadi Sedaghat Pisheh for his excellent work in the fabrication and testing of the lasers. I know I could not come this far if it were not for his thorough experimental abilities. Dr. Abdullah Demir made a significant impact on this work. His contribution includes fabrication design, optimization, and consultation.

I thank my advisor and the head of the Department of Physics, Prof. Oğuz Gülseren for his help, guidance and incentive attitude during my time in Bilkent. I also thank Prof. Mehmet Parlak, Prof. Ceyhun Bulutay, Asst. Prof. Onur Tokel and Prof. Raşit Turan for agreeing to review my thesis and their valuable comments.

I am grateful to Prof. Carlo Sirtori and Dr. Maria Amanti for inviting me to Laboratoire Matériaux et Phénomènes Quantiques in Paris Diderot University and hosting me in their lab, initiating me in QCLs. I also thank Prof. Carlo Sirtori and Dr. Ariane Calvar for QCL crystals and help in designs. Collaborating with them was a great honor and pleasure.

I thank my friend and our colleague from METU, Mete Günöven for many measurements and building experimental setups. I also appreciate METU and his advisor Prof. Raşit Turan for lending of equipment.

I thank my team members and friends, Rahim Bahari, Ertuğrul Karademir, Abdullah Muti, and Enes Seker for their help. I learned many things from them.

I want to express my gratitude to Murat Güre, Ergün Karaman and Elvan Ögün for their constant administrative and technical support.

I commemorate our beloved friend Dr. Emel Sungur. I know if she were still with us, so many things would be better.

I thank my corporate partners Mustafa Kemal İşen, DCP and Vestel Ventures for being patient with me during my Ph.D. and for their financial and moral support.

I thank Turkish Scientific and Technological Research Agency (TUBITAK) for financial support under grant no: SANTEZ, 0573.STZ.2013-2. I also thank National Metrology Institute for the lending of the integrating sphere, an essential tool for measuring the laser power.

I thank Ermaksan A. Ş., and particularly my skilled physicist friends Seval Şahin, Muhammet Genç for their help in fabrication. I thank them for their supportive talk and for believing in me. I also thank Seçkin Akıncı for his assistance on ICP-RIE.

Last but not least, I want to thank my family. My mother, father, and sister have always been exceptionally supportive of me and my education. I know I am so fortunate to have such a family. Finally, I thank my smart and hardworking physicist girlfriend Yağmur for waiting for me in Korea during my never-ending Ph.D. and encouraging me all this time.

Contents

1	Introduction	1
2	Modeling of QCLs	11
2.1	Electronic modeling of active region	12
2.2	Optical waveguide modeling	16
2.3	Thermal modeling	18
2.3.1	CW operation	20
2.3.2	Pulsed operation	22
3	Experimental	24
3.1	Epitaxial growth of quantum cascade lasers	24
3.1.1	Characterization of QCL crystals	27
3.2	Fabrication of QCLs	30
3.2.1	Process development	30
3.2.2	Mounting QCL chips	35
3.3	QCL characterization techniques	39
3.3.1	Spectral characterization	39
3.3.2	Thermal measurements	43
3.3.3	Near field measurements	44
3.3.4	Voltage-current-power measurements	45
4	Characterization of QCLs	50
4.1	Electro-optical characterization	50
4.2	Spectro-temporal measurements	58
4.3	Thermal characterization	68

5	Optical Loss Management in Long-Wave QCLs	75
5.1	Measurement of loss	76
5.2	Sources of loss in QCLs	77
5.2.1	Dielectric loss	77
5.2.2	Plasmonic loss	79
5.2.3	Free carrier absorption	80
5.3	Low loss waveguides	81
A	Active region designs	96
A.1	InGaAs/AlInAs based InP949	96
B	Fabrication Lab Flow	98
B.1	Nextnano.QCL input file for InP949	105

List of Figures

1.1	Electronic transition scheme of a QCL.	3
1.2	Active region and injector region of a QCL (one period).	3
1.3	Common schemes for QCL active region designs.	4
1.4	Diagonal (a) and horizontal (b) radiative transition in a QCL. . .	5
1.5	Three phonon resonant design emitting at $9\mu\text{m}$	5
1.6	Band gaps and lattice constants of various III-V semiconductors.	8
2.1	Flow diagram of the Nextnano.QCL calculations [1].	12
2.2	Band offsets of the InP949 QCL structure and the calculated wave- functions.	14
2.3	Density of states as a function of position and energy at 400mV and 100K.	15
2.4	Color map of electric fields of TM modes of a $30\mu\text{m}$ wide cavity. .	17
2.5	Effective indices of the eigenmodes of the QCL cavity.	18
2.6	CW thermal calculation results of the QCLs with various ridge widths.	21
2.7	Maximum temperatures in steady state calculations as a function of ridge width, for epi-down and epi-up configurations.	22
2.8	Calculated time-dependent temperatures at varied ridge widths for epi-up and epi-down configurations, for pulsed operation.	22
3.1	Schematic layout of a molecular beam epitaxy system.	25
3.2	SEM image of InGaAs/AlInAs based QCL crystal.	27
3.3	SEM image of GaAs/AlGaAs based QCL crystal.	28
3.4	Photoluminescence spectrum of InGaAs/AlInAs based QCL crys- tal (InP949) in the range of $1.25\text{-}1.8\mu\text{m}$	29

3.5	Fabrication process of QCLs from section view.	32
3.6	Fabrication steps of QCLs. Top view.	33
3.7	Optical microscope image of a QCL after opening the contact windows.	34
3.8	Optical microscope image of a QCL facet.	35
3.9	Schematics of soldering and bonding of a QCL.	35
3.10	Pick-and-place machine for placing and soldering lasers.	36
3.11	A finished laser, soldered and wire bonded.	36
3.12	Drawing of submount for epi-down mounting	37
3.13	Epi-down mounted QCL	38
3.14	FTIR spectrometer (Bruker Vertex 70V) and the optical path in external source measurement mode.	39
3.15	FTIR spectrum of a QCL in pulsed operation at various voltages. Waveguide width is 12 μm , cavity length is approximately 3 mm.	41
3.16	Fourier filtering to separate longitudinal FP modes.	43
3.17	Measured and calculated cavity temperatures as a function of time for various waveguide widths.	44
3.18	Experimental setup for near-field measurements.	45
3.19	Thermal camera of a QCL mounted on a LN-cooled dewar below threshold (a) and above threshold (b).	46
3.20	Experimental setup for pulsed Voltage current and power measurement.	47
3.21	Voltage and current waveforms of 1 μs pulse recorded by an oscilloscope.	48
4.1	Voltage-current-power characteristics of QCLs with 2mm cavity length and various widths.	51
4.2	Diagram of alignment of band energy levels under increasing electric field resulting negative differential resistance.	52
4.3	Turn-down voltage of the lasers with cavity length of 1.5mm as a function of temperature.	53
4.4	Turn-down voltage of the lasers with cavity length of 1.5mm as a function of temperature.	54

4.5	Optical power of Si ₃ N ₄ passivated QCLs as a function of pulse width and duty cycle.	57
4.6	Voltage-current-power characteristics of QCLs with 2 mm long cavity length with mirror at the back facet.	58
4.7	Time resolved spectrum of a QCL with 20 μm waveguide width and 3.8mm cavity length at 2 μs long 16V voltage pulse.	59
4.8	Time resolved spectrum of a QCL with 24μm waveguide width and 1.8mm cavity length at various 2 μs long pulse voltages.	60
4.9	Time resolved spectrum of a QCL with 12μm waveguide width and 1.8mm cavity length at varied 2 μs long pulse voltages.	61
4.10	Spectrum of 1.5mm long QCLs as a function of applied voltage at -170°C.	63
4.11	Spectrum of 1.5mm QCLs various voltages as a function of applied voltage at -155°C.	64
4.12	Spectrum of 1.5mm QCLs various voltages as a function of applied voltage at -140°C.	65
4.13	Spectra of 1.5mm QCLs as a function of applied voltage	66
4.14	Frequency splitting of 1.5 mm 12 μm laser at -140 °C as a function of laser power.	67
4.15	Time resolved spectrum of a QCL displaying shift of longitudinal FP modes at two different biases.	68
4.16	Shift of the Fabry-Perot modes as a function of heatsink temperature.	69
4.17	Time resolved average cavity temperatures at different heatsink temperatures.	70
4.18	Time resolved temperatures at different duty cycles (a). Initial temperatures as a function of duty cycle (b).	71
4.19	Simulated and measured time resolved cavity temperatures at various electrical input powers.	72
4.20	Average temperature as a function of in plane (k_x) and out of plane (k_y) thermal conductivities	73
5.1	Extinction coefficient of Si ₃ N ₄ and HfO ₂	78
5.2	Absorbance of AlN thin films compared to and Si ₃ N ₄	79

5.3	Loss of the fundamental TM mode of waveguides with varied width, as a function of dielectric thickness. © 2018 IEEE.	80
5.4	Current-power characteristics of HfO ₂ passivated QCLs with 1.8, 2.5 and 3.8mm cavity length and various thicknesses.	82
5.5	Inverse of slope efficiency as a function of cavity length. © 2018 IEEE.	83
5.6	Lasing threshold current density as a function of cavity width for Si ₃ N ₄ and HfO ₂ passivated QCLs. © 2018 IEEE.	84

List of Tables

2.1	Oscillator strengths of transitions.	13
2.2	Doping, thickness and refractive indices of InP949 epicrystal layers.	17
2.3	Thermal conductivity and specific heat parameters of QCL layers	19
4.1	Parameters derived from current-voltage-power measurement of QCL	56

Chapter 1

Introduction

Quantum cascade lasers (QCLs) are semiconductor lasers that can emit coherent light from mid-infrared to terahertz wavelengths. These lasers are made from many layers of ultrathin binary, ternary and quaternary epitaxial compounds of III. and V. column elements of the periodic table such as GaAs, AlGaAs, AlInAs. Typically, AlInAs/InGaAs based QCLs emit light at 3.5-24 μm and AlGaAs/GaAs based systems are used for 8-23 μm and 64-225 μm . QCLs generate coherent light similar to laser diodes, but laser diodes amplify light generated during recombination of electrons and holes, while QCLs make use of interband transitions, i.e. electronic transitions between the energy states within the conduction band of the material (Fig. 1.1), hence there is no need for holes to generate light. QCLs are, therefore, unipolar devices.

Enabling physics and technologies for the realization of QCLs have been developed over the course of past 50 years. In 1970, Esaki and Tsu discussed semiconductor "superlattices" by periodic growth of epitaxial semiconductor layers [2]. Kazarinov and Suris put forward the idea of stimulated amplification of light from intersubband transitions of quantum wells for the first time [3] in 1971. First intersubband laser was demonstrated by Faist et. al. in 1994 [4]. Concept of lasing from intersubband emission was actually put forward long before the invention of QCL. A cyclotron laser based on radiative transition of electrons

between the Landau levels of semiconductors had been realized [5, 6].

A typical QCL consists of an active region, generating the light and an optical cavity required for feedback to amplify light. The active region of a quantum cascade laser, called a stage, consists of a number of very thin epitaxial layers that determine the energy levels of electron transport as well as that of the lasing transition. A number of layers are doped preceding the lasing region and is called the injector layer. This stage also contains layers that make up the energy levels that rapidly empty the lower lasing energy levels to maintain population inversion. Finally, a number of layers are doped. Typically a QCL repeats this stage many times to increase optical power output (Fig. 1.1) The same potential that injects electrons into QCL structure bends the energy bands so that the lower energy state of one period become aligned with the upper energy state of the next period. Therefore, an electron that makes a transition from the upper energy state to a lower energy state by emission of a photon makes another fast transition to yet another lower energy state, finally tunneling out to the high energy state of the next stage. Although shortest wavelength that a laser diode can emit (without the use of nonlinear effects) is determined by the band gap of the material, for QCL's there is no band gap limit. The emission wavelength is determined by the energy states in the quantum wells which can be tuned by thickness and composition of the layers. The emission wavelength is determined by the difference between the designated upper energy level and the lower laser level, which are formed by the combined energy levels of coupled quantum wells. We can, thus, vary the thickness of quantum wells and the emission wavelength can become longer, but there are many challenges in producing a long wavelength QCL; specifically lasing at high temperatures. They are generally cooled down to liquid nitrogen or liquid helium temperatures for lasing to take place. Further, for these long wavelength lasers, lifetimes of the higher energy states are longer, so that care must be taken to assure lasing.

For lasing to take place, population inversion should occur, which means number of electrons in the higher lasing state (state 3 in Fig. 1.2) should be larger than the number of electrons in the lower lasing state (state 2 in Fig. 1.2). To

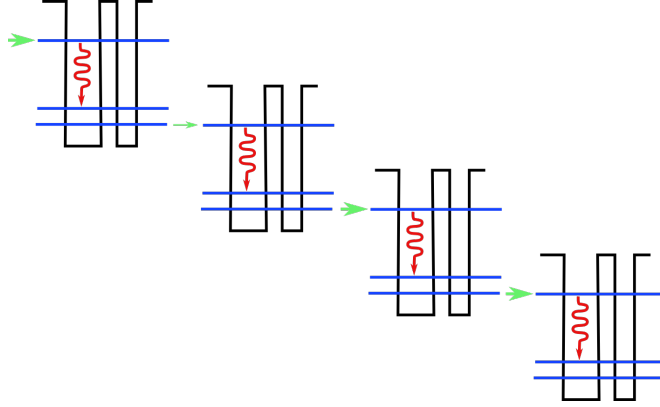


Figure 1.1: Electronic transition scheme of a QCL.

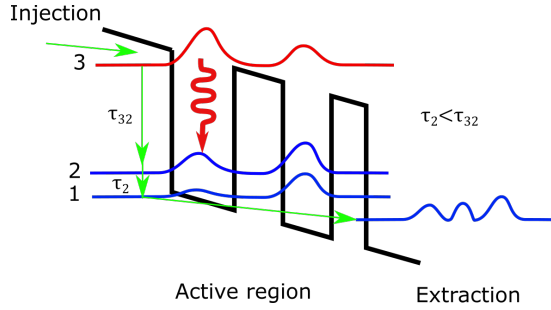


Figure 1.2: Active region and injector region of a QCL (one period).

A radiative transition occurs between states 3 and 2. Fast transitions occur between states 2 and 1. Then the electron moves to the next period via the injector region

ensure population inversion, QCLs are designed in a way that radiative transition time (τ_{32} in Fig. 1.2.) is sufficiently longer than the non radiative transition draining the lower lasing state (τ_2 in Fig. 1.2.). Given two wavefunctions in the quantum wells the transition probability is proportional to the dipole matrix element;

$$z_{mn} \propto \int f_m^*(z) \frac{d}{dz} f_n(z) dz \quad (1.1)$$

where $f_m(z)$ and $f_n(z)$ are the wavefunctions of the respective electronic states involved in the laser transition.

There are many approaches for the electronic design of a QCL. Fig. 1.3 shows some of the more common schemes for the active region design. These are: a) two quantum well design with vertical lasing transition and a phonon scattering,

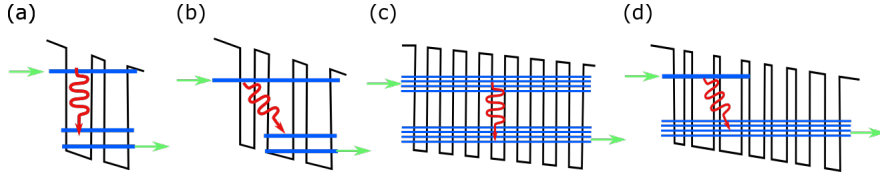


Figure 1.3: Common schemes for QCL active region designs.

b) three quantum well-based design with diagonal lasing transition followed by tunneling to the next stage after scattering from an optical phonon, c) radiative transition between the superlattice minibands, d) "bound-to-continuum" design, i. e. radiative transition from a bound upper state to a miniband. Fig.1.4 shows the details of diagonal and horizontal transitions in two different QCL designs with three quantum well active regions. In Fig. 1.4, the injector region is a chirped superlattice and active region is made up of three quantum wells. Laser transition occurs between the states shown in red. Since the upper energy state and the lower energy state are localized in different quantum wells, these transitions are called diagonal transitions. Due to the fact that the wavefunctions are separated in space, dipole matrix element of transition from upper to lower state is smaller, and the lifetime of the transition is relatively long (1.6 ps). However, the lower state has the same energy as another adjacent state in the injector region, it, therefore, tunnels into the injector region easily. In this region, there are three lower energy states. These states are separated by an energy difference close to the optical phonon energy of the material. The electron scatters from optical phonons consequently to the lowest energy state of the injector and tunnels to the next active region. Fig. 1.4.b is an example of a vertical transition. In this case, the transition will have the lifetime of a vertical transition, but since the lower wavefunction extends into the injector region, which is a superlattice, the electron will empty the lower energy state fast enough.

A challenge for QCL design is making them operate efficiently at relatively high temperatures. When QCL was first invented in 1994, it was operated at 90K maximum [4]. Due to the escape time of the electrons in the lowest energy level of the active region to the injector, electrons accumulate at the lowest energy level of the active region, and a portion of these electrons is thermally excited to the lower lasing state. This is called thermal back-filling, and detrimental

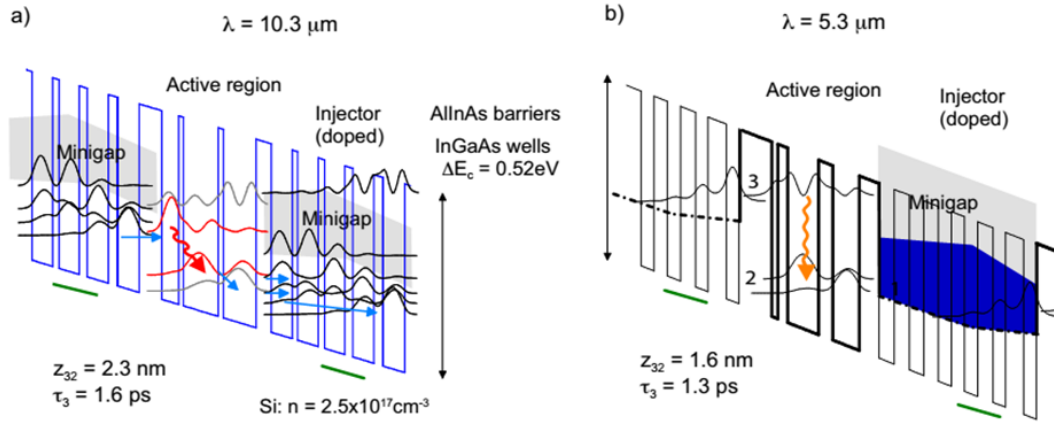


Figure 1.4: Diagonal (a) and horizontal (b) radiative transition in a QCL.

[7]

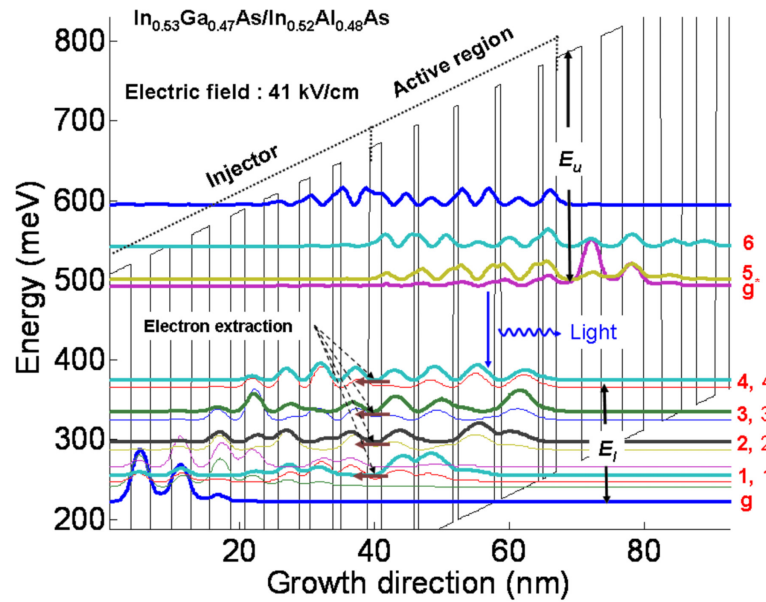


Figure 1.5: Three phonon resonant design emitting at $9\mu\text{m}$.

Reprinted from [Appl. Phys. Lett. 94, 011103 (2009)], with the permission of AIP Publishing.

to the population inversion. To prevent this, an approach is making use of the resonant phonon scattering. Lower energy states of the active region are separated by a longitudinal-optical (LO) phonon energy so that an electron in the lower lasing state makes a resonant and, therefore, fast transition to the next energy level. Generally, active regions are designed for two or three successive phonon scattering which prevents thermal back-filling, efficiently. Fig. 1.5 shows the 3-phonon resonant design from [8]. Lasing occurs between the states g and 4, and the electron in state 4 scatters into state 3, 2 and 1, then finally tunnels into the upper lasing level of the next stage. The energy difference between the consecutive lower states is around 30 meV. Due to fast phonon scattering, the effective lifetime of the lower lasing state is about 0.14 ps. In this work, we mainly used a 3 phonon resonant design similar to this one, and the layers are shown in Appendix A.1. Calculated band structure and energy states are shown in Chapter 2.1.

It is also possible to design an active region using the electronic energy levels of a superlattice. In a superlattice, energy states within the conduction band form a new band gap which is called a minigap. Electronic states with energies below and above the minigap are called minibands. In this superlattice active region, radiative transitions occur between the mini bands. Within the minibands, there are many states with energies close to each other. A transition may occur from any energy state of the upper miniband to the lower miniband. In the lower miniband, the states are emptied fast, since there are many empty states. However, the drawback of this approach is that it requires higher currents to initiate lasing.

QCLs can be engineered to have more than one lasing wavelength [9, 10]. The radiative transition with different wavelengths may occur in different quantum well regions. In this case, the electric field of each region within the QCL will be inhomogeneous, and design will be complicated. If transitions may also occur in the same region, but between different states, and the electric field along the epitaxial layers would be homogeneous. Multi-wavelength QCLs also may exhibit nonlinear effects [11, 12].

For THz frequency QCLs, generally, GaAs/AlGaAs based designs are made.

Due to the low energy difference between the lasing states, these lasers operate at lower temperatures. In general, the maximum operating temperature has the trend $T = \hbar\omega/k_B$ [22]. THz QCLs is an active research topic due to the need for compact and high brightness source at these frequencies.

Wavelength tunability of QCLs is an active research area. There are many areas of technology where coherent infrared light sources would be of interest. Most notably, vibrational and rotational modes of absorption in molecules are in this wavelength region, yet currently used broadband or tunable radiation sources, such as globar and free electron laser are bulky and have low brightness. With tunable QCLs compact infrared absorption spectrometers would be possible. In the mid-infrared region, 1.5cm^{-1} tuning is possible with current, $10\text{-}200\text{cm}^{-1}$ with temperature, and about 100 cm^{-1} with an external grating element. In the THz region, tuning is easier with built structures. Since THz wavelengths are longer, these lasers are less sensitive to mechanical tolerances of the microfabrication processes. These lasers may be tuned with an integrated grating reflector [13] or by moving an adjustment lever made out of silicon, which changes the effective index of the laser cavity when it is close enough to it [14].

Similar to laser diodes, QCLs are fabricated in the form of long and thin waveguide structures. This structure is called the “ridge waveguide” and guides the light along the optical axis. The two ends of the waveguide are flat, and these ends form the laser cavity. One end can be coated by a highly reflective coating, and the laser light exits the device out of the other end. For QCL devices, typically, metallic mirrors with a layer of insulator is used, since metal has low absorption at long wavelengths [15]. Using a highly reflective mirror decreases the threshold current for lasing since it will increase the spontaneously emitted photon density within the cavity.

QCL wafers are grown epitaxially and typically on GaAs, InAs or InP substrates. Molecular beam epitaxy (MBE) is the first approach used to fabricate a QCL wafer. Lasing wavelength of a design depends on the material system used. MBE uses an ultrahigh vacuum chamber to grow highly crystalline films. Another popular method is metalorganic vapour phase epitaxy (MOCVD). This

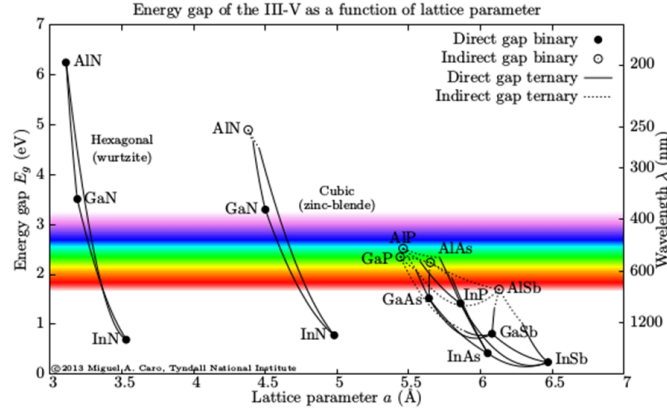


Figure 1.6: Band gaps and lattice constants of various III-V semiconductors.

[16]

method uses organometallic precursors in the gas form. These gases disintegrate on the hot surface of the substrate in the reaction chamber. MOCVD does not require high vacuum but it is less precise in terms of film thickness, thus thicker designs are more suitable to be grown by MOCVD.

During the layer growth, if the lattice constant of the film material does not match the lattice constant of the substrate, compressive or tensile stresses occur. The stress on the films accumulate as the thickness increases and may cause deformations or cracks. Therefore, stress limits the maximum thickness of the QCL structure. Material system is composed of different semiconductor layers forming the barriers and the quantum wells which determines the range of wavelengths that a QCL design can emit. Compositions of the layers and hence the band offsets, as well as the thickness of each layer, is critical in the design. For a given material system, as the wavelength of emission gets shorter, upper lasing level approaches the band edges which results in electron leakage from the quantum wells raising threshold current and eventually suppressing lasing transition. Therefore, for shorter wavelengths, larger band offsets are required. Fig. 5. Shows the band gap energies of some III-V semiconductors with their lattice constants. At the NIR region (2.5-4 μm) designs with strained lattices are used [17, 18, 19]. In the MWIR (4-5 μm), strain-balanced designs are used [20, 21, 22]. In this case, compressive and tensile stresses of the films are fine-tuned to balance each other. In the LWIR (8-12 μm) lattice matched InGaAs/AlInAs based designs are used

[8, 23] The composition of the alloys are tuned to match the lattice constants, therefore, these designs have no stress.

Many applications of QCLs have been realized and many more are being explored. They range from spectroscopy, (chemical weapon detection, breath analysis [24], air pollution analysis, medical imaging, leak detectors, end-point detectors for dry etch process, free space communications, explosive and poisonous gas detectors and defense against heat-seeking weapons, (DIRCM). Applications of THz lasers are mainly focused on ground penetration and detection beyond obstructions.

This thesis consists of 4 main sections; In the modeling chapter (2), we used calculation tools such as Comsol Multiphysics and Nextnano to examine electronic, optical and thermal properties of QCLs. Using Nextnano, we calculated the band structure and wavefunctions of the active region as well as energies of the states and oscillator strengths of the transitions. We used Comsol Multiphysics for optical and thermal calculations and built parametric optical and thermal models of the QCL waveguides. We calculated the optical modes of various waveguide geometries and built a model for calculation of the loss due to dielectrics and metals in the laser structure. Using the thermal models, we calculated the spatial and temporal temperature rise for both continuous-wave and pulsed mode. We also examined the effect of epi-up and epi-down mounting on temperature rise. In the experimental chapter (3), we described the techniques used to fabricate and characterize QCLs, such as current-voltage and spectral characterization methods. We fabricated QCLs with various geometries, passivation materials, and facet mirrors. For optoelectronic characterization in pulsed mode, we built an experimental setup that enables fast time-dependent measurements of laser current, voltage, and optical power. For spectral measurements, we used fast, time-resolved, step-scan Fourier transform infrared spectroscopy to obtain high spectral and temporal resolution spectra. In the characterization chapter (4), we study the optoelectronic and spectral results of QCL characterization techniques. We analyzed the current-voltage characteristics and its relationship with waveguide geometry and temperature. We examined spectral modes of QCLs with various geometries at varied temperature and voltages. Using Fabry-Perot modes

for the first time, we measured the in-situ cavity temperatures in pulsed mode. Combining the optical and thermal models with experimental time-resolved temperatures, we estimated the thermal conductivity of the active region. In Chapter 5, we review the sources of optical loss in QCLs waveguides and demonstrate the low loss waveguides with experimental and simulated data. We fabricate and test HfO₂ and Si₃N₄ passivated low loss QCLs. Using the relationship between cavity length and waveguide loss, we found that HfO₂ passivated lasers have about half the loss of Si₃N₄ passivated lasers. We measured up to 500 mW optical peak powers in HfO₂ passivated lasers.

Chapter 2

Modeling of QCLs

We study the modeling of our QCLs in 3 separated sections; the first is the modeling of the electronic energy levels. For modeling of electronic states, we used the nextnano software, and calculated the relevant wavefunctions, as well as corresponding energies and oscillator strengths involved in lasing using Nextnano software [1]. These calculations are crucial for the epitaxial crystal design of a QCL.

The second part of modeling is the calculation of optical modes, effective indices, and losses. For this purpose, we used the Comsol wave optics module. Optical calculations aid the design of the waveguides and understanding the sources of optical loss. Using the optical model, in this chapter, we discuss the strategies to reduce loss in the waveguide in chapter 5.

The third part of this chapter is the thermal modeling. For thermal calculations, we used heat transfer in solids module of Comsol. Using these models, we calculated the cavity temperatures in steady state and as a function of time. Thermal simulations help us to understand the effect of QCL structure and mounting techniques on laser heating. We also used these simulations in combination with the experimental cavity temperatures as will be shown in section 4.3, to deduce the thermal conductivity as well as operational constraints on the active region.

2.1 Electronic modeling of active region

Modeling a QCL requires the calculation of the electronic energy levels that make up the QCL. This requires the solutions of Schroedinger equation along with the Poisson's equation for a structure with many ultrathin semiconductor layers of known composition and doping. Luckily, there are commercial software that attempt to do this. In this thesis, we explore the Nextnano.QCL software in an attempt to determine the relevant wavefunctions and energy levels of a QCL structure lasing around $9.15 \mu\text{m}$ with three-phonon extraction scheme.

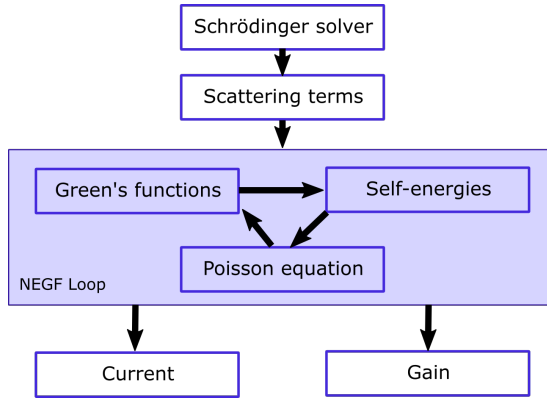


Figure 2.1: Flow diagram of the Nextnano.QCL calculations [1].

Nextnano software uses non-equilibrium Green's function (NEGF) approach (also known as Keldysh or Kadanoff-Baym formalism) to simulate quantum transport in QCLs. It includes longitudinal polar-optical phonon scattering (polar LO phonon scattering, acoustic phonon scattering, charged impurity scattering, interface roughness scattering, alloy scattering, and electron-electron scattering). The formalism used in the software also allows the use of coherent transport effects i.e: resonant tunneling and the like. Figure 2.1 summarizes the working framework of the software.

In the NEGF approach, scattering processes are described in terms of self-energies. Self-consistent calculations of self-energies and Green's functions are done and both elastic and inelastic scattering processes are included within the self-consistent Born approximation under periodic boundary conditions. NEGF is typically used for "open systems", i. e. devices with two semi-infinite contacts.

To calculate the Green's functions and the self energies, a set of partial differential equations has to be solved [25];

$$G^R = (E\hat{I} - \hat{H}_0 - \Sigma^R)^{-1}, \quad (2.1)$$

$$G^< = G^R \Sigma^< G^{R*}, \quad (2.2)$$

$$\Sigma^< = G^< D^<, \quad (2.3)$$

$$\Sigma^R = G^R D^R + G^R D^< + G^< D^R \quad (2.4)$$

Here, G^R is the retarded and $G^<$ is the lesser Green's functions and Σ^R and $\Sigma^<$ are called retarded and lesser self energies. H_0 is the Hamiltonian of the electronic structure and defined as;

$$\hat{H}_0 = \frac{-\hbar^2}{2} \partial_z \frac{1}{m^*(z, E)} \partial_z + \frac{\hbar^2 k^2}{2m^{\parallel}(z, E)} + V(z) \quad (2.5)$$

where z is the coordinate in perpendicular direction of layers, m^* is the effective mass, m^{\parallel} is the effective mass of the subband, $V(z)$ is the potential due to energy bands and charge distribution and;

$$V(z) = V_c(z) - e\Phi(z) \quad (2.6)$$

where $V_c(z)$ is the conduction band edge potential and $\Phi(z)$ is the electrostatic potential. To solve this set of equations, generally iterative methods are used [25].

State	1	2	3	4	5
1	-	0.91	0.050	0.41	0.16
2	0.91	-	0.62	0.0089	0.051
3	0.050	0.62	-	0.49	0.17
4	0.41	0.0089	0.49	-	0.43
5	0.16	0.051	0.17	0.43	-

Table 2.1: Oscillator strengths of transitions.

For band structure and wavefunction calculations we used the Nextnano.QCL software. This software solve Schroedinger and Poisson equations of the given band structure using a self-consistent non-equilibrium Green's function solver.

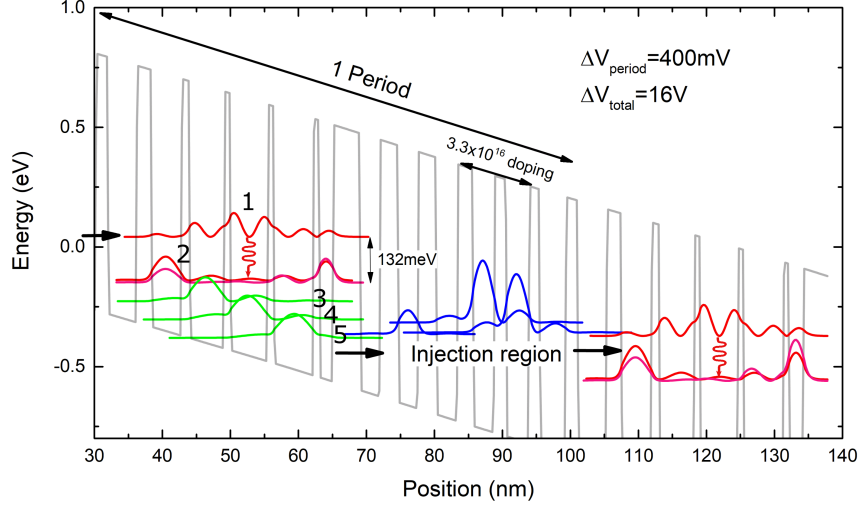


Figure 2.2: Band offsets of the InP949 QCL structure and the calculated wavefunctions.

Inputs for the software are material layers, thicknesses of the layers, electric field, conduction band energies and masses of each material. Fig. 2.2. is the calculated band structure and the wavefunctions of the active region of InP949 design. This is a 3 phonon resonant structure similar to the given in [8]. Layer thicknesses and doping levels of this design are listed in Appendix A.1. Nextnano.QCL input file for the design is given in appendix B.1 Bias voltage is 0.4V per period (16V on 40 periods). Gray lines shows the conduction band offsets; barriers are AlInAs, and wells are InGaAs layers. Each wavefunction has an offset according to their energy level. Wavefunction 1 is the upper level of the laser. Lasing transition occur between the state 1 and 2. Energy difference between these two states are 132 meV, which corresponds to $9.4 \mu\text{m}$ in wavelength. Below the state 2, there are 3 other states, then the upper level of the next period, state 1'. Energy difference between 2-3, 3-4 and 4-5 are about 40 meV, which is close to optical phonon energies in AlInAs/InGaAs. In AlInAs, AlAs-like longitudinal optical (LO) phonon energy is about 45 meV and InAs-like LO phonon energy is about 30 meV [26]. Fast non-radiative transitions due to phonon scattering facilitates transfer between states 2-3, 3-4 and 4-5, emptying the lower lasing state 2. This mechanism promotes population inversion. Due to three consecutive phonon

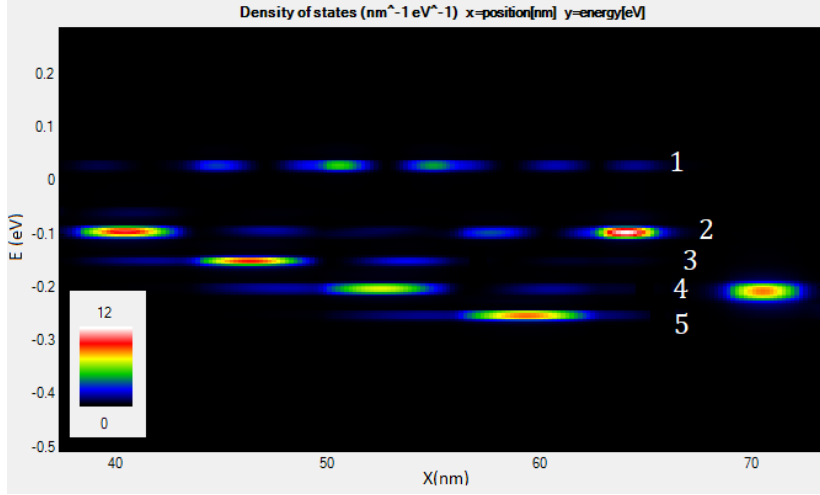


Figure 2.3: Density of states as a function of position and energy at 400mV and 100K.

scatterings, reverse process rate of thermal back-filling is much lower than the forward rate, therefore the electrons in state 1' cannot easily be excited back to the state 2 due to increased rate of phonon scattering at higher temperatures. This is also an important feature for room temperature operation of the 3-phonon resonant design. Oscillator strength for transitions between each state is given in Table 2.1. Red cell shows the lasing transition, while green ones are the phonon resonant transitions. Oscillator strengths indicate which transition is most probable. For all of the states, transition is most probable for the adjacent states; For state 1, the most probable transition is to state 2, or back to the lowest state of the previous period. Oscillator strength of the lasing transition is about 1/8 of the phonon resonant transition. Therefore, due to current conservation in steady state, the number of electrons in the upper level has to be more than the ones in the lower state, which facilitates population inversion.

Fig. 2.3 shows the density of states as a function of position and energy. The horizontal axis is the position with respect to the beginning of the period, and the vertical axis is the energy of the states. Density of states corresponding to each wavefunction is marked with rectangles. At 100K density of states of each state has an approximately 7meV of width.

2.2 Optical waveguide modeling

To calculate the optical modes propagating in the waveguide, we solve the eigenfunctions of the wave equation

$$\nabla^2 \frac{1}{\mu} (\nabla \times E) - k_0^2 (\epsilon_r - J \frac{j\sigma}{\omega\epsilon_0}) E \quad (2.7)$$

Here, we assume that there is no current flow or any charge density. We also assume the electric field in the propagation direction z , is periodic, i. e.;

$$E(x, y, z) = \tilde{E}(x, y) e^{-ik_z z} \quad (2.8)$$

This is called the paraxial wave approximation, or slowly varying envelope approximation. The resulting differential equation is called Helmholtz equation;

$$\frac{1}{\mu} \nabla^2 E(x, y) - k_0^2 \epsilon_r E(x, y) = 0; \quad (2.9)$$

Comsol use a finite element method to discretize the waveguide geometry and solve the eigenfunctions of the Helmholtz equation. Each eigenfunction corresponds to an optical boundary mode. Walls of the waveguide was defined semi-circular, as in wet-etched ridges. The layers were defined using the refractive indices given in the literature. Table 2.2 shows the semiconductor layers of the epitaxial structure along with its doping, thickness and the refractive index. References for the values indicated in the table for each layer. Refractive index of the layers depends on the doping strongly, especially in the long-wavelength. Hence, we included the effect of doping on the index using the data from the references shown in the table. Index for the active region is calculated using extrapolation on data from [27]. For the simulation boundaries, we defined a scattering boundary condition, which does not actually affect the modes, when the simulation boundaries are large enough (about $100 \times 100 \mu\text{m}$).

Since the intersubband radiation occurs in TM polarization (electric field perpendicular to the epitaxial planes), only TM modes are relevant to QCL operation. Fig. 2.4 shows the TM optical modes in a $30 \mu\text{m}$ wide waveguide. The mode at the top is the fundamental TM mode and higher order modes are shown

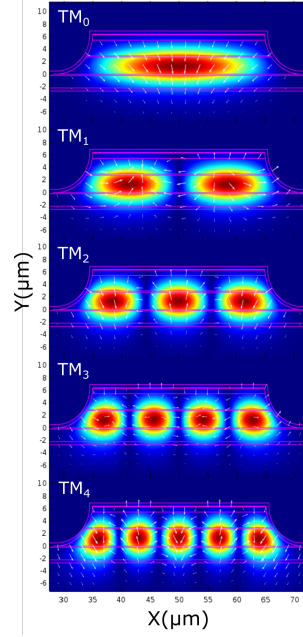


Figure 2.4: Color map of electric fields of TM modes of a $30\mu\text{m}$ wide cavity.

respectively. Fig. 2.5 shows the effective indices of both TE and TM modes as a function of ridge widths, from 6 to $30\mu\text{m}$. Effective indices of all modes increase with ridge width. Below effective index of 3.03, modes are not confined. As the ridge width increases, the waveguide supports more modes.

Description	Doping (cm^{-3})	Layer Thickness (nm)	Refractive index
InGaAs: Si	Si:5E18)	100	2.37 [28]
InP	Si:(5E18)	850	2.9641 [29]
InP	Si:(5E16)	2500	3.0531 [29]
InGaAs	Si:(5E16)	200	3.30 [28]
Active region (Al _{0.33} InGa _{0.67} As)		2764	3.23 [27]
InGaAs	Si:(5E16)	200	3.30 [28]
InP	Si:(5E16)	2000	3.0531 [29]
InGaAs	Si:(1E18)	50	2.90 [29]
Buffer: InP	Si:(5E18)		2.9641 [29]

Table 2.2: Doping, thickness and refractive indices of InP949 epicrystal layers.

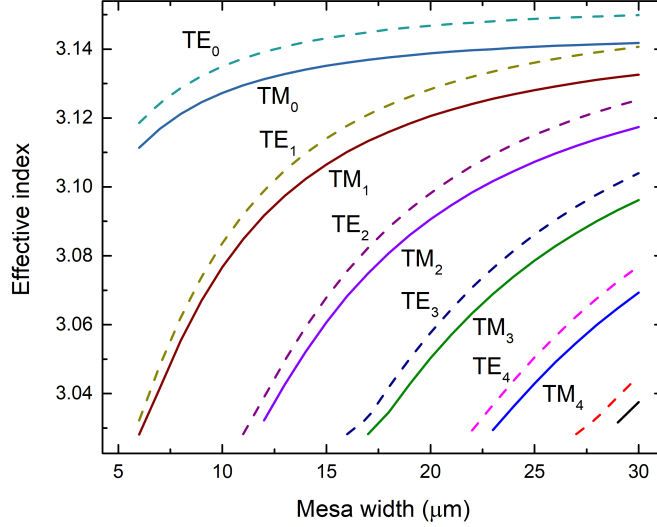


Figure 2.5: Effective indices of the eigenmodes of the QCL cavity.

2.3 Thermal modeling

Energy in the electronic system is dissipated by light and scattering by phonons. Dominant mechanism for heat transport in the QCL active region is phonon scattering. Phonons scatter from other phonons as well as electrons and impurities in the crystal. In a junction of two different semiconductors, due to different phonon dispersion relation of two materials, an acoustic mismatch occurs and cause scattering of the phonons at the interface. This result in a temperature discontinuity at the junction. The temperature discontinuity (ΔT) depends on the heat flux perpendicular to the interface (Q) and the thermal boundary resistance of the junction (R) with the formula;

$$\Delta T = RQ \quad (2.10)$$

This phenomenon is called Kapitza resistance and has been observed in interfaces of many metals, semiconductors, and fluids. A QCL active region has typically hundreds of semiconductor interfaces. Therefore, Kapitza resistance significant factor affecting thermal properties of QCLs. The thermal conductivity of the active region of a QCL is less than that of its constituent bulk materials and

strongly anisotropic. Vitiello et. al. [30] measured a 5-fold reduction of the out-of-plane thermal conductivity of a GaAs/Al_{0.15}Ga_{0.85}As QCL crystal. In-plane thermal conductivity was also found to be reduced by 30% due to interface roughness scattering. In another report [31], average thermal boundary resistance of various QCL material systems are listed. Average InGaAs/AlInAs boundary resistance of a QCL operating at 8 μ m wavelength is reported as 4.4 10⁹m²K/W, and the resulting out-of-plane thermal conductivity was 1.7 W/m.K. It was concluded that for thermal conductivity of QCLs, Kapitza resistance plays a much stronger role than the bulk thermal conductivities.

High thermal resistance of the active region of a QCL is a major factor in reducing their thermal performance. The active region is also thicker than most semiconductor lasers, further complicating their heat dissipation. First QCLs were operated at cryogenic temperatures, and for the first years of QCL research, studies were intensively conducted for operation at room temperature [32]. Although it was achieved for mid-wave and long-wave lasers, optical power reduces with temperature, especially for continuous wave (CW) operation [33, 34]. At THz frequencies, room temperature QCL is currently an active research topic [35, 36].

Although the optical power density at the facet is relatively small, catastrophic mirror damage could also be an issue for QCLs. However, unlike, for example, high power diode lasers, the damage is not due to optical power but due to the thermoelastic stress generated by the high electrical power dissipated at the active region [37, 38, 39].

Table 2.3: Thermal conductivity and specific heat parameters of QCL layers

Layer	κ_{300} (W/m.K)	α	C_0 (j/g.K)	k_t (10 ⁻³ /K)
InP	68 [40]	-1.4 [40]	0.373 [41]	6.42 [41]
InGaAs	4.8[40]	-1.17 [40]	0.318 [42]	8.00 [42]
Active region	$k_t=2.1$ W/m.K		0.344	7.54

Specific heat and thermal conductivity are the fundamental properties of the materials to be modeled in the simulations. Both these parameters are temperature dependent. We used experimental data from the literature [40, 42, 43]

and fitted the function $C_V(T) = C_0(1 - e^{-k_t T})$ for the specific heats, and $\kappa(T) = \kappa_{300}(T/300K)^\alpha$ for the thermal conductivities. For the specific heat of the active region, C_0 and k_t values were calculated from a weighted average of InGaAs and AlInAs. Values for C_0 , κ_t , κ_{300} and α are shown in Table 2.3.

For thermal modeling of the QCL cavity, we used Comsol Multiphysics Heat Transfer in Solid module. It uses a finite element method to solve the heat transfer equation in 2D;

$$d_z \rho C_p \frac{\partial T}{\partial t} + d_z \rho C_p u \cdot \nabla T = Q \quad (2.11)$$

The first term defines the time dependence and equals to zero for steady state calculations. The second term defines the heat flux due to temperature gradients and Q is the heat source. d_z is the thickness of the 2d structure and used to calculate the heat source power density. ρ is the density and C_p is the specific heat.

2.3.1 CW operation

To calculate the CW operation of QCLs, we conducted steady-state simulation of the waveguide at the 2D cross-section. A heat source with constant power density, $P_{in}=250\mu\text{W}/\mu\text{m}^3$ was defined on the active region. InP substrate thickness is 200 μm and electroplated gold thickness (on the top of the waveguide) is defined as 5 μm . Initial temperatures of all layers are -170°C. For epi-down configuration, a heatsink was defined on top of the waveguide using a fixed temperature boundary condition. This is a best-case scenario that assumes the submount material has a very high thermal conductivity. For the epi-up configuration, the heatsink is defined at the bottom of the substrate. Fig. 2.6 shows some of the results of the simulations for various ridge widths. (a) is the colormap plot of the temperature of a 6 μm laser. Dotted lines on the colormap plot show the sections along which the horizontal and vertical temperature profiles are plotted. (b) and (d) are horizontal; (c) and (e) are vertical cross-section temperatures for varied ridge widths. For both configurations, the maximum temperature in the active region

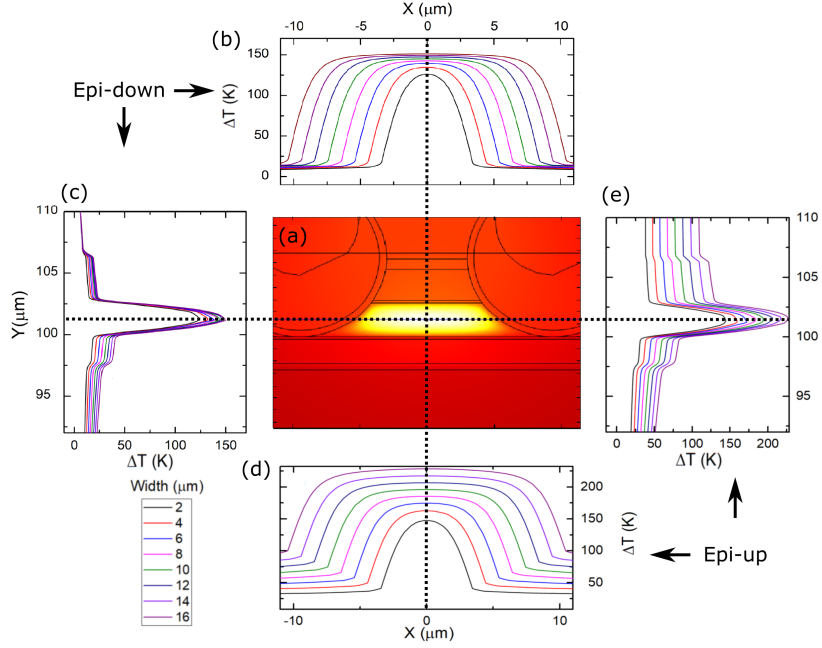


Figure 2.6: CW thermal calculation results of the QCLs with various ridge widths.

(a) 2D temperature color map of a distribution of a 6 μm wide laser. (b)

Temperature as a function of x coordinate along the central horizontal cross-section of the lasers with various widths, for epi-down configuration. (c)

Temperature as a function of y coordinate along the central vertical cross-section of the lasers with various widths, for epi-up configuration.

(d) Temperature as a function of x coordinate along the central horizontal cross-section of the lasers with various widths, for epi-down configuration. (e)

Temperature as a function of y coordinate along the central vertical cross-section of the lasers with various widths, for epi-down configuration.

increases with increasing waveguide width. For wide lasers, horizontal temperature cross-section reaches to the maximum temperature about $2\mu\text{m}$ within the ridge walls. Vertical temperature cross sections, on the other hand, is maximum at the center of the active region. Since the gradient of temperature indicates the heat flow rate, particularly for wide lasers, heat flow occurs mainly in the vertical direction. The effect of the heat resistance of the substrate is also obvious; in epi-up configuration, temperatures are significantly higher. Fig. 2.7 shows the maximum temperature in the cavity as a function of time, for the same power density as above and. Epi-up laser temperature rises almost linearly with the ridge width, but epi-down laser temperature rise is much less for all ridge widths and has a tendency to converge to a maximum value as the ridge with increases.

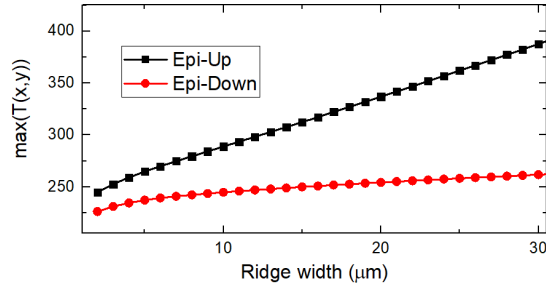


Figure 2.7: Maximum temperatures in steady state calculations as a function of ridge width, for epi-down and epi-up configurations.

These results show that especially for broad area QCLs and for CW operation, epi-down mounting is critical.

2.3.2 Pulsed operation

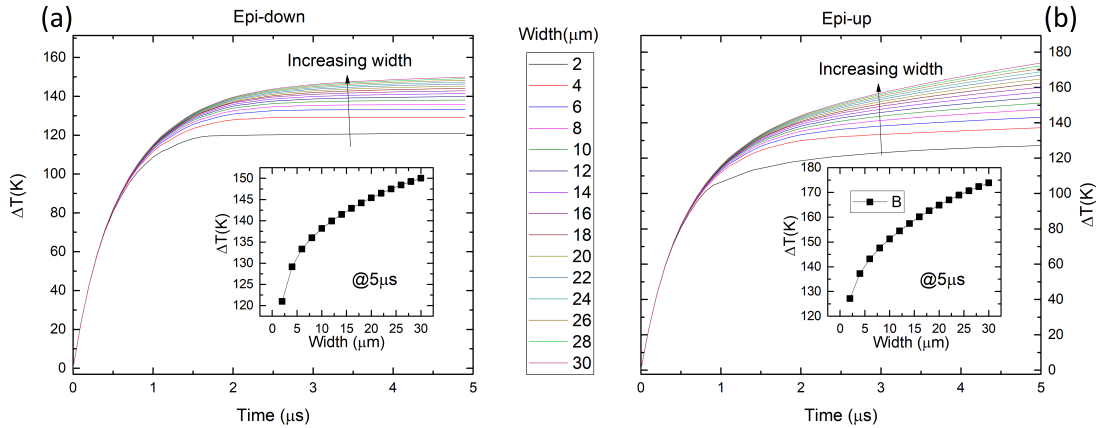


Figure 2.8: Calculated time-dependent temperatures at varied ridge widths for epi-up and epi-down configurations, for pulsed operation.

Fig. 2.8 shows the maximum temperature of the active region as a function of time at varied ridge widths, for epi-down (a) and epi-up(b) configurations. Power density on the active region is the same as CW case and $250 \mu\text{W}/\mu\text{m}^3$. Initial temperatures are $-170 \text{ }^\circ\text{C}$. For both epi-up and epi-down case, until about 500 ns, the temperature rise is independent of the ridge width. This shows that at this time interval, the temperature rise is dominated by the specific heat of the material. After 1 μs wider lasers reach higher temperatures, which was also

observed in steady state calculations. Temperature rise at $5 \mu s$ is shown in the insets. Epi down laser reach to the equilibrium temperature in a few microseconds, but, epi-up laser temperatures continue to rise after $5 \mu s$. These results show that for pulsed operation at low duty cycles and $t < 500$ ns, epi-up and epi-down mounting display similar thermal performance. For longer pulses, epi-down mounting reduces the maximum temperature by 10%. However, as we noted in the steady-state calculations, due to substrate heating, epi-up lasers continue to rise in temperature for longer pulses.

Chapter 3

Experimental

3.1 Epitaxial growth of quantum cascade lasers

Typical QCL epitaxial structure contains up to hundreds of epitaxial crystal layers each of which is very thin. In general, each layer consists of a ternary compound adjacent to a different ternary compound. Obtaining the correct composition and balancing the likely strain accumulation is a challenge. Considering that growth conditions for each layer are different, rapid switching from one growth condition to the other is required. Further, interdiffusion of ternary constituents needs to be avoided to obtain sharp interfaces, a difficult task at best.

Molecular beam epitaxy (MBE) is a widely used technique for growth of thin semiconductor epitaxial crystals. This is a growth method that enable deposition of crystalline layers with precise control of alloy composition, doping, thickness and strain. For the first decade of the QCL research, it was the method of choice for the precision requirements of the QCL designs.

Schematic layout of an MBE system is shown in Fig. 3.1. MBE system is an ultra-high vacuum chamber with base pressures of 10^{-8} to 10^{-12} Torr. Inside the chamber, there are sources of semiconductor precursors and a "seed

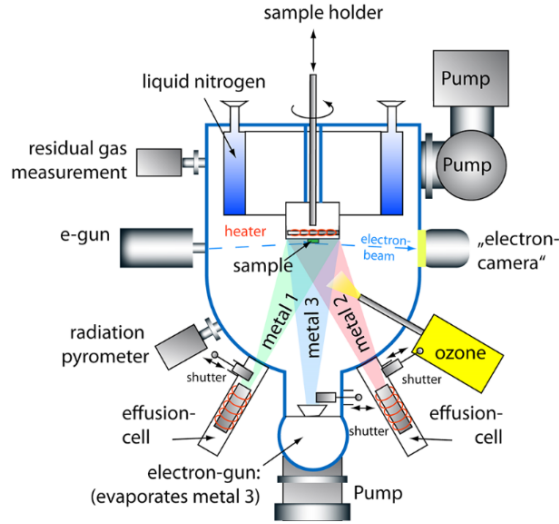


Figure 3.1: Schematic layout of a molecular beam epitaxy system.

[44]

crystal” to grow the epitaxial layers on. Semiconductor source is typically an ”effusion cell” which is a temperature controlled container that heats the precursors. Heated precursors sublime from the effusion cell and deposits on the seed crystal. The seed crystal is normally a polished wafer. The crystal is also heated to facilitate diffusion of the precursor atoms on the surface. MBE systems are generally equipped with a ”reflection high-energy electron diffraction” (RHEED) setup which monitors the crystal growth stages. A high energy electron source is directed on the epitaxial crystal surface and the reflected electrons form a diffraction pattern on a phosphorescent screen. The diffraction pattern oscillates at the period of deposition of a complete single crystal layer. Therefore, it enables precise monitoring of the number of monolayers deposited. Each source has a mechanical shutter that enables to control the composition of the layers.

For QCLs, elemental sources of Ga, In, Al, As, P are typically used. Silicon is a commonly used doping element. Partial pressure (beam equivalent pressure) of the precursor elements are very low, in the order of 10^{-7} Torr. For this reason, deposition rates are also low; between $0.5\text{-}1\mu\text{m}/\text{hour}$. Typical substrate temperatures are between $400\text{-}600^\circ\text{C}$. There is an optimal substrate temperature regime for each material. Optimal quality is achieved between $460\text{-}510^\circ\text{C}$ for InGaAs, while for AlInAs, $520\text{-}550^\circ\text{C}$ is preferred [45]. Each layer is grown at an optimum

temperature and temperature is ramped up and down as the layer compositions are changed.

Most of the QCL crystals used in this thesis were grown by MBE. Since we did not have an in-house MBE system, they were fabricated in the commercial facility of IQE company [46].

Alternatively, metalorganic chemical vapor deposition (MOCVD) has recently become a common technique for growth of epitaxial layers. MOCVD use metalorganic precursors in gas form which react with the crystal surface to grow layers. Metalorganic precursors used for this method are compounds of a metal (indium, gallium or aluminum) and organic radicals, such as methyl and ethyl, such as trimethylaluminum ($\text{Al}_2(\text{CH}_3)_6$) and triethylgallium ($\text{Ga}(\text{C}_2\text{H}_5)_3$). These precursors have a low vapor pressure and most of them are liquid at room temperature. Within the MOCVD chamber, seed wafer is heated to 500-600°C. Vapors of the precursors are sent into the chamber and decompose at the surface of the crystal. Metal atom is bonded to the surface while the organic part (methane or ethane) leaves in gas form. Arsenic and phosphor are introduced in the chamber using phosphine (PH_3) or arsine (AsH_3) gases.

MOCVD has a higher growth rate compared to MBE (1.5-2 $\mu\text{m}/\text{hour}$) and it does not require ultra-high vacuum. For this reason, MOCVD growth is a lower cost approach than MBE. However, the process control is more complex than MBE. Since the chamber is not in ultra-high vacuum, one cannot use RHEED to control the number of monolayers. Instead, optical reflectometry is used. In this approach, a laser beam is shone onto the sample surface through a window and reflected light is collected. As the thickness and refractive index of the layers change, reflected power oscillates, the period of which depends on thickness. This allows the monitoring of the growth in real time. To stop the growth of the crystal layer, precursor gases in the chamber needs to be purged, and purging is not as fast as an MBE source shutter, in general. For these reasons, MOCVD requires longer calibration routines to grow crystals at the required precision. The growth temperatures, generally, are higher in MOCVD systems when compared with MBE growth, as pyrolysis of the gases on the surface of the sample is temperature

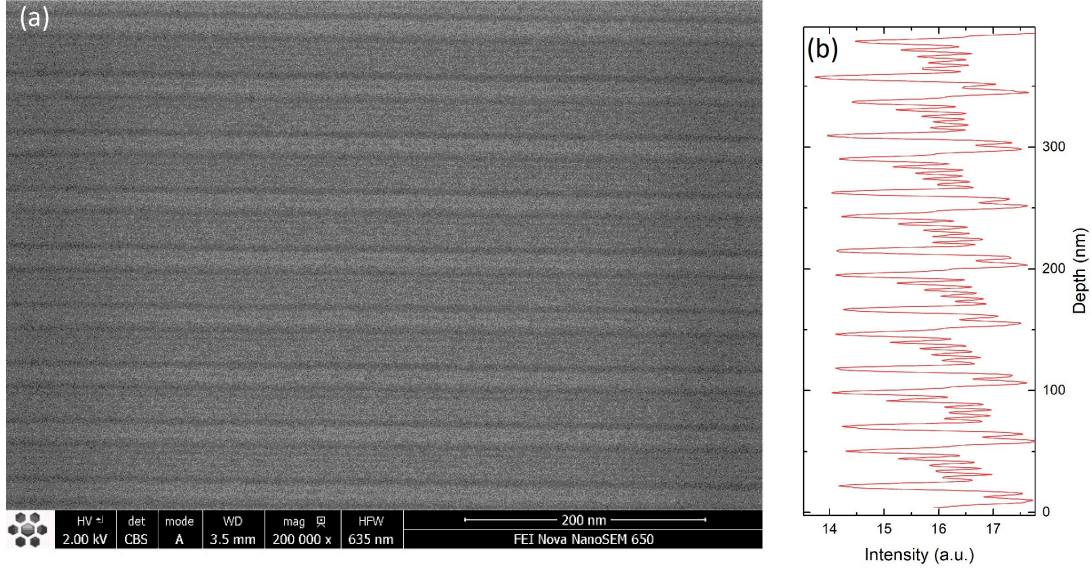


Figure 3.3: SEM image of GaAs/AlGaAs based QCL crystal.
 (a) SEM image (b) Intensity profile of the image.

high-resolution scanning electron microscope (SEM). Even without EDX functionality, it is possible to distinguish between the quantum well and barrier layers. (Fig. 3.2) shows the SEM image of the layers seen from a cleaved facet of the InGaAs/AlInAs based crystal and Fig. 3.3 shows the AlGaAs/GaAs based crystal¹. Plots on the right (b) are intensity profiles averaged along the lateral axis. Both images clearly show the QCL periods, as well as the individual layers. InGaAs layers appear brighter than the AlInAs layers, while GaAs layers appear brighter than AlGaAs layers. Also, doped regions, i.e. injection region, are darker than undoped ones. SEM can serve as a quick check tool for layer thicknesses. The thickness of a period was found to be 48 nm for the AlGaAs/GaAs sample (design thickness: 47.8 nm) and for the InGaAs/AlInAs (Fig. 3.2) it was found to be 69 nm (design thickness: 69.1 nm).

Fig. 3.4 is the photoluminescence spectrum of InP949 crystal used in our experiments. This spectrum was measured by FTIR. The sample is cooled to 35K in a cryostat. Excitation laser is a 633nm He-Ne laser and modulated at a few kHz with an optical chopper. The signal was measured using an InGaAs photodiode connected to a lock-in amplifier. Lock-in amplifier is synchronized with

¹We thank Ermaksan A. Ş. for high-resolution SEM images.

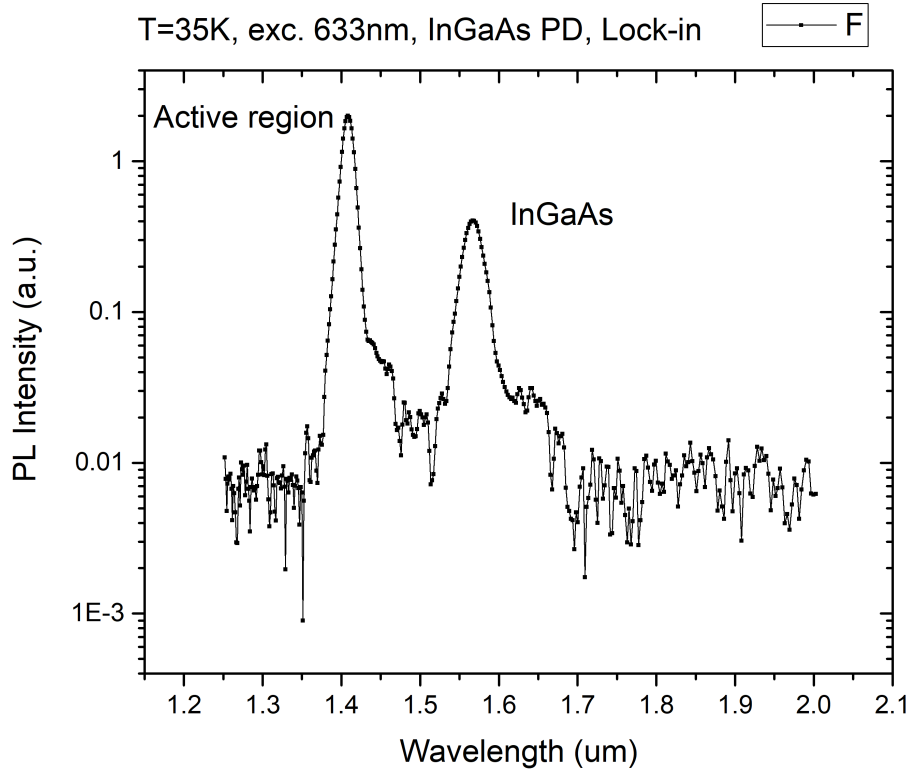


Figure 3.4: Photoluminescence spectrum of InGaAs/AlInAs based QCL crystal (InP949) in the range of 1.25-1.8 μ m.

the chopper and the amplitude output of the lock-in is connected to the external sensor input of the FTIR. We attribute the peak at 1.57 μ m to InGaAs cladding and the peak at 1.41 μ m to the InGaAs wells in the active region. The energy difference between the two peaks is about 90 meV and due to the energy offset between the conduction band edge of the InGaAs wells and the lowest energy level in the band structure of the active region. Shoulders towards the longer wavelength on both peaks could be due to the doping states. We should note that those PL signals are due to interband transitions. Although we attempted to measure intraband transitions at longer wavelengths, we could not observe any signal even after 3-4 hours of detector integration times (using a DTGS photodetector). This could be due to the spontaneous intersubband transitions being dominated by non-radiative processes [67].

3.2 Fabrication of QCLs

QCL fabrication is a complex process with many steps. In this section, we describe the methods we used to fabricate a QCL device in two parts; the first part is on process development of micro-fabrication, and the second part is on mounting (or packaging) of the processed epitaxial crystal pieces.

3.2.1 Process development

Like many other semiconductor lasers, to fabricate a QCL laser, a waveguide is formed in the shape of thin, long strip. This strip is made by removing material from both sides of the cavity and in a process called etching. There are two types of conventional etching methods for QCLs; "wet" etching and "dry" etching. Wet etching is the removal of material by using a chemical solution. Typical chemicals used for wet etching III-V materials are; HCl, HBr, HPO_3 , H_2SO_4 , HNO_3 and H_2O_2 . A typical etchant recipe consists of an aqueous solution of an oxidizer (HNO_3 or H_2O_2) and a non-oxidizing acid. Oxidizers form a layer of oxide on the surface of the material, but in general, they alone can not remove material. III-V oxides are not water soluble, therefore, they form a protective layer on the crystal, which stops the reaction. However, non-oxidizing acids react with the oxide to form a soluble compound. Since the epitaxial crystal of a QCL consists of many different materials with different doping levels, a non-selective etchant with equal etch rates for different layers, is needed. For InGaAs/AlInAs/InP material system, a HBr based recipe is commonly used: HBr: HNO_3 : H_2O 1:1:10. This solution etches InP, AlInAs and InGaAs with an etch rate of approximately $1\mu\text{m}/\text{min}$ at room temperature. When using this solution, one should consider a few things; etching should be done under a fume hood since the solution releases HBr vapor, which is a strong irritant. After preparing the solution, it should be "aged" for at least a week, since right after preparation, etch rates are very variable and gas bubbles may form on the sample. This etchant is also light sensitive, so it is recommended to protect it from light during etching. We observed asymmetrical etched cavities, due to the light coming from one side of the room.

Once the solution is used it should be kept in a glass bottle under dark.

Dry etching is another common technique for semiconductor laser fabrication. In this case, instead of liquid solutions, chemicals and ions in gas form are used. For III-V materials, plasma-based etching techniques are widely used. These techniques generate a plasma in a gas chamber in which the epitaxial crystal is placed. This technique is generally preferred when it is necessary to control the etched wall profiles. Two kinds of etching mechanisms exist for plasma etching: physical and chemical etching. Physical etching is the removal of material on the surface due to impact between the energetic ions and neutral gas and the atoms of the epitaxial surface. This process is non-selective and able to etch many different materials. Chemical etching depends on reaction kinetics between the plasma activated radicals and the crystal. The aim is to find etchant and material combinations where the final etched product is in the gas phase with high vapor pressure, which can be pumped out from the vacuum system. Chlorine-based dry etching recipes are commonly used for GaAs/AlGaAs material systems, but compounds with indium are difficult to etch since the vapor pressure of the indium-chlorine compounds is much lower. For In containing crystals, either chlorine or bromine based recipes at elevated temperatures (200°C or more) [68] or CH₄ based recipes at room temperature is used [69, 70]. CH₄ recipes have downsides as well, the etch rates are low and they deposit carbon on the surface that inhibits etching. Although there are many recipes in the literature, one should still expect a long optimization process since many parameters are sample dependent and not readily adaptable to different ICP-RIE systems.

QCL epitaxial crystals have a relatively thick active region and cladding. The in-plane electrical conductivity of the active region is much less than the out-of-plane conductivity. To confine the current in the waveguide, it is necessary to etch all the way down to the active region. Typical etch depths are 5-7 microns. For this reason, QCL mesas have higher aspect ratios than diode lasers. Passivation of the mesa walls become critical since it affects both thermal performance and optical loss. Most common QCL laser structures are double channel (DC) and buried heterostructure devices. DC-QCLs are made by etching two parallel channels on

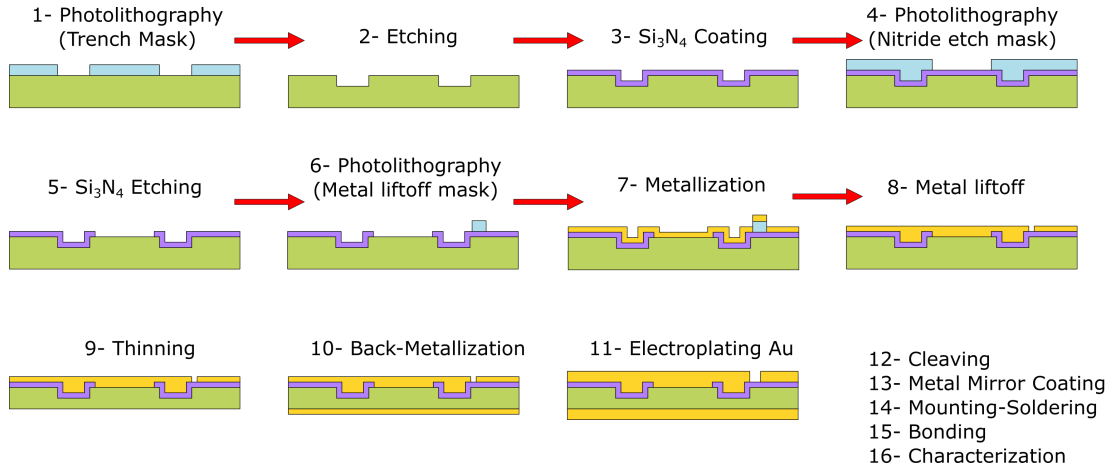


Figure 3.5: Fabrication process of QCLs from section view.

the QCL crystal and the long and thin mesa between the channels form the laser waveguide. After etching, walls of the trenches are passivated using a dielectric such as Si_3N_4 or SiO_2 . For buried heterostructure, the etched trenches are refilled by growing an insulating epitaxial crystal using typically, MOCVD; this process step is called regrowth. For InGaAs/AlInAs based QCLs, Fe-doped InP is used as regrown passivation. Fe doping ensures that InP is an insulator. Regrown epitaxial layers repair the vertical continuity of the crystal and with high thermal conductivity, ensure lateral cooling of the cavity while confining the current under the mesa. However, regrowth is both a complex and expensive approach and is not readily available. In our work, we did not use regrowth, instead, we used Si_3N_4 or HfO_2 for sidewall passivation. We also tried to use SrF_2 , as an insulator, but the results were not good; SrF_2 caused problems in the electroplating steps, and SrF_2 passivated lasers electrically shorted at very low voltages (5V). This could be due to ionic conduction of SrF_2 [71].

Fig 3.5 delineates the fabrication steps schematically. First, a photoresist mask is patterned on the epitaxial wafer. Then the sample is etched using HBr HNO_3 etchant. Etch depth is determined according to the thickness of the top cladding and active region. Then the sample is coated with silicon nitride (or other passivation materials such as HfO_2). Followed by another photoresist pattern that leaves the top of the waveguides uncovered. Si_3N_4 on top of the waveguide is

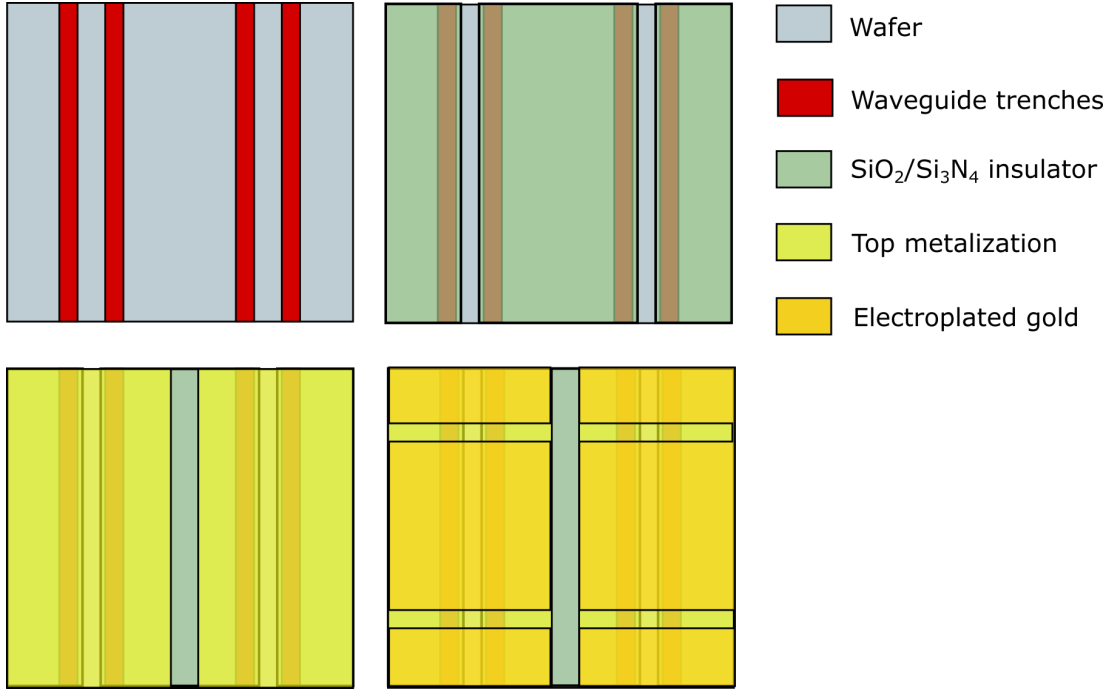


Figure 3.6: Fabrication steps of QCLs. Top view.

etched using buffered oxide etchant. This etched window is for electrical contacts. For the next step, which is called lift-off, another photoresist pattern is made. The sample is then coated with Ti/Au (20/100nm) metal using e-beam evaporation. For lift-off, the sample is soaked in acetone to remove the photoresist pattern along with the metallization on top of the photoresist. Then, if needed, the sample is thinned on the back side with mechanical grinding or chemical etching. After cleaning the sample, back side is also metalized. Finally, the gold at the top of the chip is thickened to about $5 \mu\text{m}$ by electroplating more gold. Appendix B lists the detailed fabrication steps, we used for our lasers.

Fig. 3.6 schematically shows the fabrication process from the top view of the sample. In the figure, two waveguides are shown on the same chip, but we actually fabricated close to 40 emitters per $1 \times 1 \text{cm}$ chips with $450\text{-}500 \mu\text{m}$ periods. After opening the trenches waveguides are formed. When designing the photomasks for anisotropic wet etch, one should consider the possible undercuts due to non-selectivity of the etch. Since the etch depth is $\approx 7 \mu\text{m}$, waveguide trench patterns should be $7 \mu\text{m}$ narrower than the required trench width. The

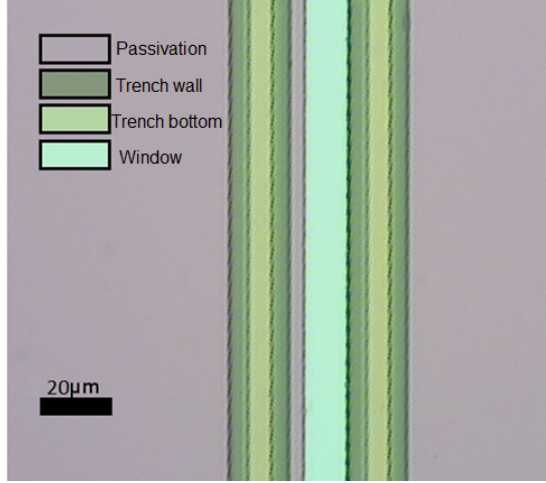


Figure 3.7: Optical microscope image of a QCL after opening the contact windows.

most alignment sensitive part of the fabrication process is the opening of the passivation windows. To increase alignment tolerances, passivation windows are designed to be approximately $4 \mu\text{m}$ narrower from the waveguide mesa. Metallic contacts of each laser are designed to be separate in the lift-off process. The width of the stripe that separates the contacts is $30 \mu\text{m}$. Finally, for electroplating, it is necessary to protect the line at which facets will be cleaved. This line should not be electroplated since after cleaving electroplated gold may overhang on the facet and cause electrical short-circuiting. To prevent this, a $100 \mu\text{m}$ stripe is patterned with photoresist along the lines at which the chips will be cleaved.

Fig 3.7 shows the optical microscope image of a mesa taken after the opening of contact windows. In this sample, alignment is not optimal, but since the large contact window alignment tolerances, these lasers worked as expected.

Fig 3.8 shows an image of the QCL facet from an optical microscope. Wall profiles are semi-circular due to anisotropic etch. The active region is also visible due to its slightly higher optical reflectivity. To calculate the radius of the wall, we inspected the images of the facets and found that lateral and vertical etch radii (w_1 and w_2 in Fig. 3.8) are not equal. The ratio of the horizontal radius to vertical is approximately 1.5. Also, undercut to etch-depth ratio is 0.8.

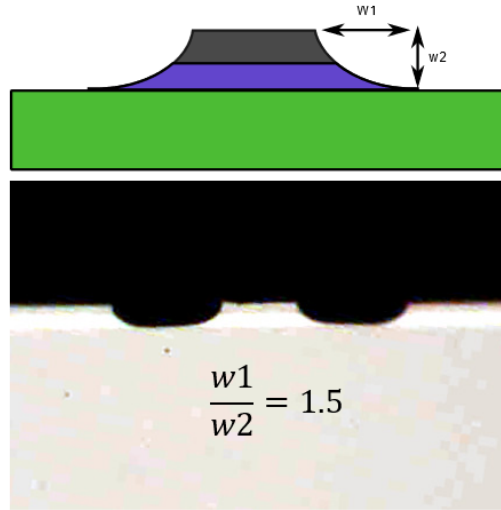


Figure 3.8: Optical microscope image of a QCL facet.

To increase the power collected from one facet, it is recommended to coat one of the facets with a high reflective material. For long-wave QCL, gold is an ideal reflector material with about 95% reflectivity [72]. To form the mirror, we coated the back-facet with 100 nm Al_2O_3 / 10 nm Ti/100 nm Au / 100 nm Al_2O_3 by e-beam evaporation. Al_2O_3 is required to prevent electrical short-circuiting and titanium is needed to promote adhesion of the gold film. We designed an apparatus to hold the cleaved chips during evaporation. The apparatus has slits of 100 and 200 μm which expose the area on the facet needed to be coated. Al_2O_3 is coated with 200 μm slit and Ti/Au is coated with 100 μm slit so that mirror metal is kept away from the top contact.

3.2.2 Mounting QCL chips

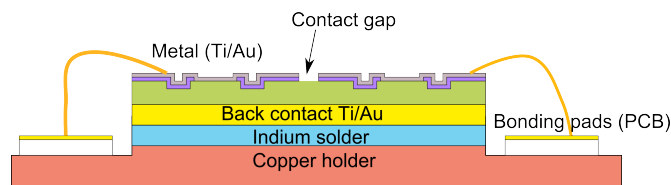


Figure 3.9: Schematics of soldering and bonding of a QCL.

For testing of fabricated chips, it is necessary to package the lasers properly. Sensitive facets and brittle nature of InP complicates the process, but, once the process is optimized, it can be achieved routinely. Although we tried epitaxial side down (epi-down) mounting of the lasers, the main approach we used in our lab was epitaxial side up (epi-up) mounting and wire bonding. The laser chips are soldered to copper holders using indium and lasers are bonded on pads on custom-made printed circuit boards (PCBs). Fig. 3.9 demonstrates the packaging schematically.

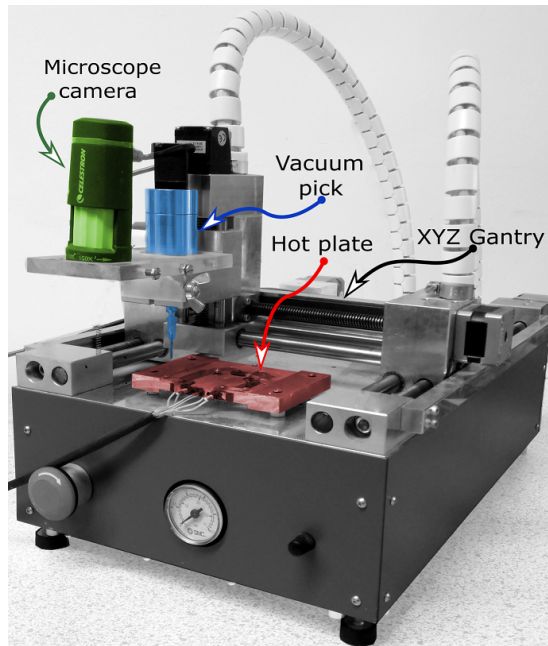


Figure 3.10: Pick-and-place machine for placing and soldering lasers.

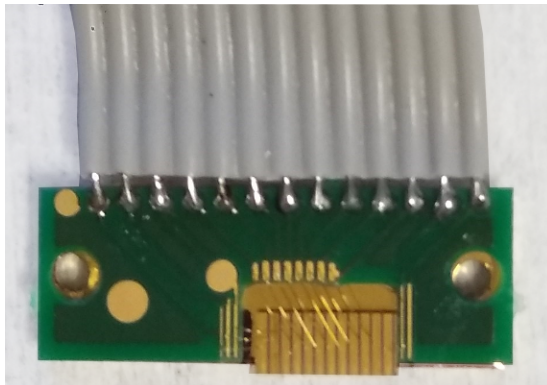


Figure 3.11: A finished laser, soldered and wire bonded.

Packaging during the initial attempts of our work was extremely wasteful and more than half of the lasers were being damaged. We first used indium ribbons cut in the shape of the chips. However, without solder flux, indium ribbons did not adhere properly on the chip and flux tended to contaminate the facets. We, then, tried indium solder paste, which already contains flux, but without proper patterning of the paste, it still caused contamination. Therefore, we used custom made metal stencils commonly used for PCB fabrication to pattern the indium paste. After application of the solder, to place the chip on the holder precisely, we used a modified pick-and-place machine (Cirroid machine [73], Fig. 3.10). We mounted a USB microscope and a temperature controlled heating stage. By using a program written in LabVIEW, we could mount the laser on copper pads with $\approx 10 \mu\text{m}$ precision and control the heating profiles. The heating profile we used was; ramp up to 120°C in 2 minutes, stay at 120°C for 1 minute, ramp up to 190°C in 1 minute, stop heater and wait until the stage cools down to $\approx 50^\circ\text{C}$.

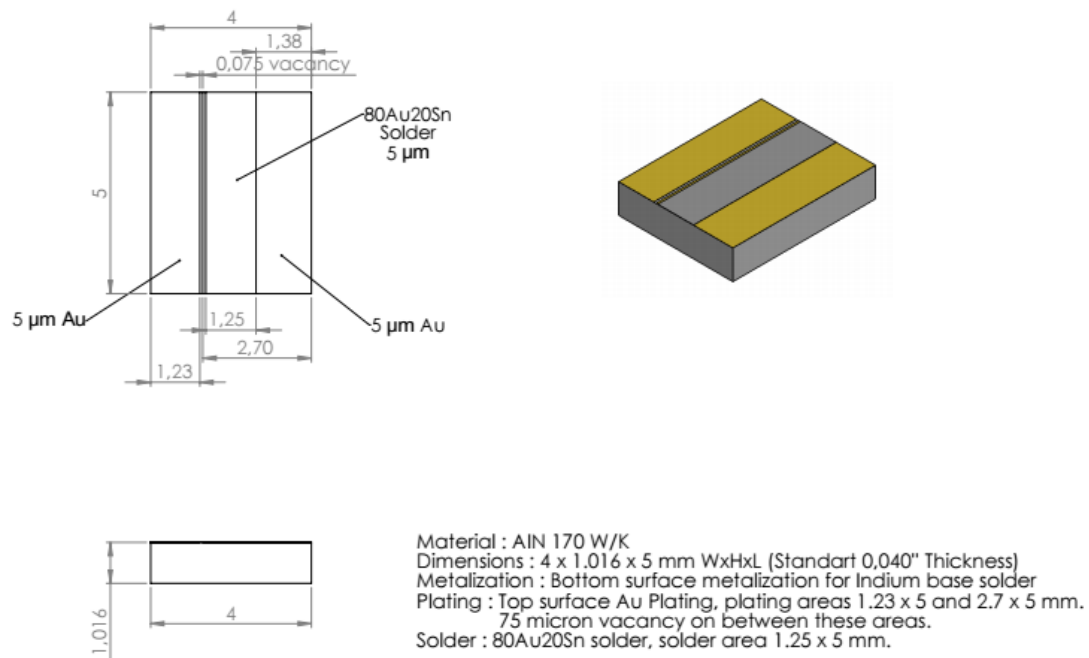


Figure 3.12: Drawing of submount for epi-down mounting

Fig. 3.11 shows a mounted laser chip on a gold plated copper holder. Each laser is bonded with $50 \mu\text{m}$ diameter gold wire on gold plated PCB pads. The copper



Figure 3.13: Epi-down mounted QCL

holder is the common cathode of the lasers and each laser's anode is connected to a separate cable. Using PCB as a bonding pad, we could measure many lasers at once, and with a low cost. We used conventional two-component epoxy glue to adhere the PCB pad to copper, but since it is brittle at low temperatures, it is recommended to use a low-temperature epoxy.

Epi-down mounting is another common method for packaging QCLs. For this type of mounting AlN or Al₂O₃ submounts coated with patterned solder is used. Epi-down mounting is preferred for high duty cycle or continuous-wave operation. For InGaAs/AlInAs/InP material system AlN is preferred due to its high thermal conductivity and matching thermal expansion coefficient [74]. As solder, Au-Sn eutectic alloy is advantageous, since it does not require flux [75]. We used custom-made AlN submounts with Au-Sn thin film solder as shown in Fig. 3.12. We placed laser bars on solder and heated it to 320 °C with ≈10 g weight on top of the chip. However, the solder leaked out from the edges and short-circuited the laser and contaminated the back facet. Fig. 3.13 shows a epi-down soldered laser. To prevent short-circuiting, the back facet and the sides could be passivated with aluminum dioxide or silicon nitride, or submount patterned with insulating solder mask to protect the laser edges.

3.3 QCL characterization techniques

3.3.1 Spectral characterization

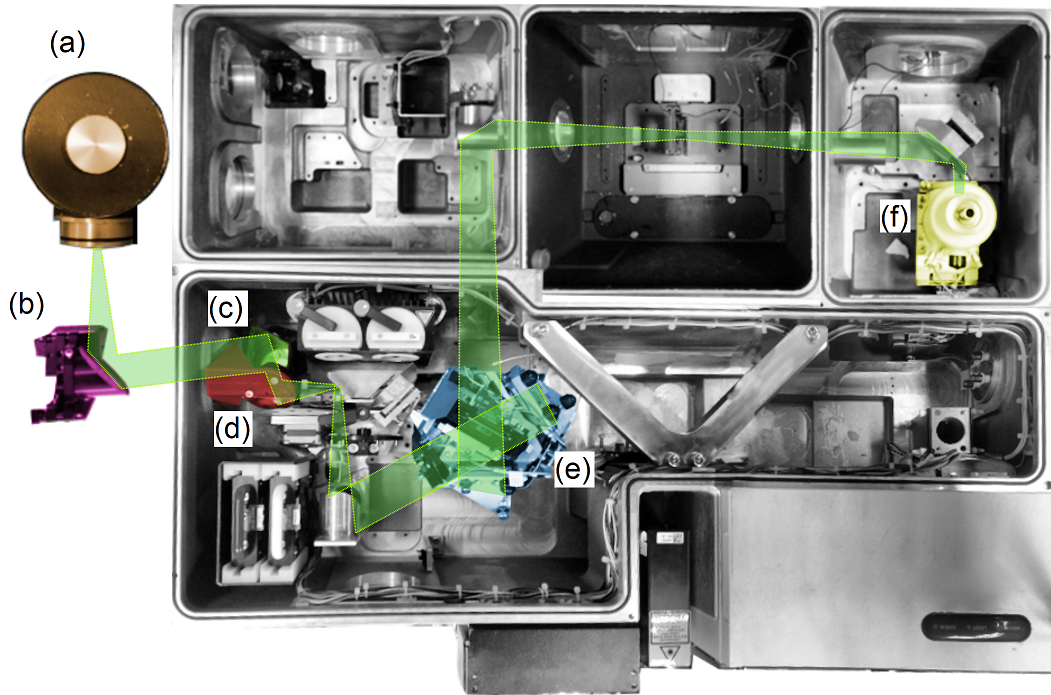


Figure 3.14: FTIR spectrometer (Bruker Vertex 70V) and the optical path in external source measurement mode.

The spectrum of a QCL yields critical information for both verification purposes, and analysis of optical modes and dynamics. For spectral measurements, a grating spectrometer with an infrared sensor could be used, but a Fourier-transform infrared spectrometer (FTIR) spectrometer is the ideal tool for this purpose. FTIR spectrometer uses a scanning Michelson interferometer to analyze infrared light. Michelson interferometer splits a beam of light into two parts with a beamsplitter and two beams go into two different "arms" of the interferometer. Both arms have a mirror at the end that reflects light back to the interferometer. If the photons reflected from the mirrors are "in phase" i. e. optical path length difference of two arms are integer multiple of the wavelength,

constructive interference occurs, if they are "out of phase", i. e. the path difference is half-integer multiple of the wavelength, destructive interference occurs. Fig. 3.14 shows the Bruker Vertex 70V spectrometer and the optical path of a QCL measurement. QCL in a liquid nitrogen dewar (a) and the light output is collimated using a gold parabolic mirror (b) and sent into the interferometer (e) via mirrors (c) and (d). The light exits from the interferometer and arrives at the mercury-cadmium-telluride (MCT) photodetector (f). Depending on the relative positions of the two arms of the interferometer, the light that exits the interferometer is modulated at a certain frequency, in wavenumber space. When two arms have equal length, all wavelengths of light coming into the interferometer transmission through the interferometer is maximum, because for all wavelength phase of light from two arms are equal. The light signal at this interferometer position corresponds to the light modulated at frequency $f=0$. As the path length of one arm gets longer, modulation frequency increases. Signal amplitude as a function of the path length difference of two arms is called an interferogram. An interferogram is essentially the Fourier transform of the related spectrum. One can obtain the spectrum by calculating the inverse Fourier transform of the interferogram.

FTIR spectrometers have some advantages compared to grating spectrometers. Grating spectrometers have a narrow slit aperture which determines the frequency resolution of the spectrum. The light to be analyzed has to be focused at this aperture for maximum signal intensity, and F-number of the focused light has to match the F-number of the spectrometer. FTIR accepts collimated light, therefore light could be sent through a much larger aperture without compromising resolution. Another advantage is that most infrared photodetectors have a relatively large and constant dark noise. Since light at many frequencies reaches the photodetector at the same time, average optical power on the detector is higher. This reduces the contribution of the dark noise on the measured signal.

Common infrared photodetector types are; thermopiles, pyroelectrics, and photodiodes. Photodiodes are photon detectors. Detector element is a p-n junction of a semiconductor. Photodiodes are often used in reverse bias. A photon excites

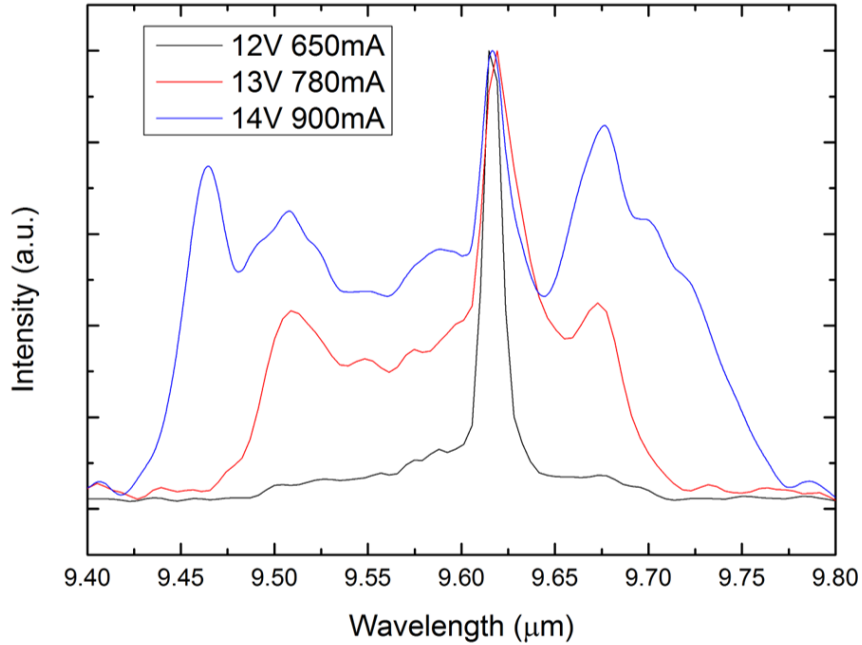


Figure 3.15: FTIR spectrum of a QCL in pulsed operation at various voltages. Waveguide width is $12 \mu\text{m}$, cavity length is approximately 3 mm .

an electron in the junction to the conduction band. Electric potential bias causes the free electron to generate current. Thermopile and pyroelectric detectors detect photons indirectly; they actually measure temperature rise at the sensor due to the absorbed light. Thermopile detectors generate a voltage proportional to optical power, while a pyroelectric detector generates a voltage proportional to change in optical power. Mercury-cadmium-telluride (MCT) is a small band-gap semiconductor and commonly used for measurement of infrared light. Its band gap depends on the mercury-cadmium ratio. At room temperature, thermally excited electrons generate significant dark current, so, MCT detectors are frequently cooled to reduce the signal to noise ratio.

The FTIR spectrometer uses a 633 nm helium-neon laser to monitor the motion of the interferometer arms. The laser goes through the interferometer, and a dedicated photodetector measures the signal intensity of the laser that exits the interferometer. The signal intensity is modulated as the arms move. The spectrometer adjusts the velocity of the interferometer mirror to keep the modulation frequency of the laser constant. Frequency is set to a constant value between

2.5-40 kHz. This is the "rapid scan mode" of the FTIR spectrometer. Fig. 3.15 shows the spectrum of a laser at various voltages in rapid scan mode. These are actually the time average of the spectra, so the rapid-scan mode is not the ideal technique for pulsed lasers. For these measurements, we used the "step-scan mode". In step scan mode, interferometer mirror stops at prefixed positions and for each position, photodetector measure the signal as a function of time. After repeating the measurement for many interferometer positions, time-resolved interferograms are obtained. At each interferometer position, acquisition of the time-dependent photodiode signal is initiated with an external trigger pulse. We used the synchronization output of the voltage pulser as the trigger pulse, therefore acquisition is synchronized with the laser pulses. To increase the signal to noise ratio, acquisition is repeated for many pulses (50-1000), and average time-resolved signals are calculated.

For pulsed laser spectral measurements, we have measured the spectra of the standard QCLs using the time-resolved step scan mode of the Bruker Vertex 70V FTIR, with a KBr beamsplitter and a fast MCT photodetector. Time-resolved MCT photodetector signal was recorded with M3I.4142 acquisition board. To keep the background temperature change to a minimum, we used 0.5% duty cycle. The highest spectral resolution was 0.5 cm^{-1} and temporal resolution was lower than 5ns. We have varied the voltage of the pulses with $2 \mu\text{s}$ width. For the $12 \mu\text{m}$ wide laser, a single mode emission at $9.21 \mu\text{m}$ was observed right above the lasing threshold. As the voltage increases, a second mode at about $9.12 \mu\text{m}$ becomes active and dominates as the voltage (or current) increases. We think these are the lateral modes of the laser cavity. Fabry-Perot modes are also visible with a period of about 1 cm^{-1} . We have observed both of these lateral and Fabry-Perot modes in the $24 \mu\text{m}$ wide laser as well, although emission wavelengths seem blue-shifted. For this laser, it looks like there are 4 lateral modes and they compete as the voltage or current varies. For both lasers, Fabry-Perot modes shifts to red with time. This is most probably due to heating of the cavity, changing the refractive indices.

3.3.2 Thermal measurements

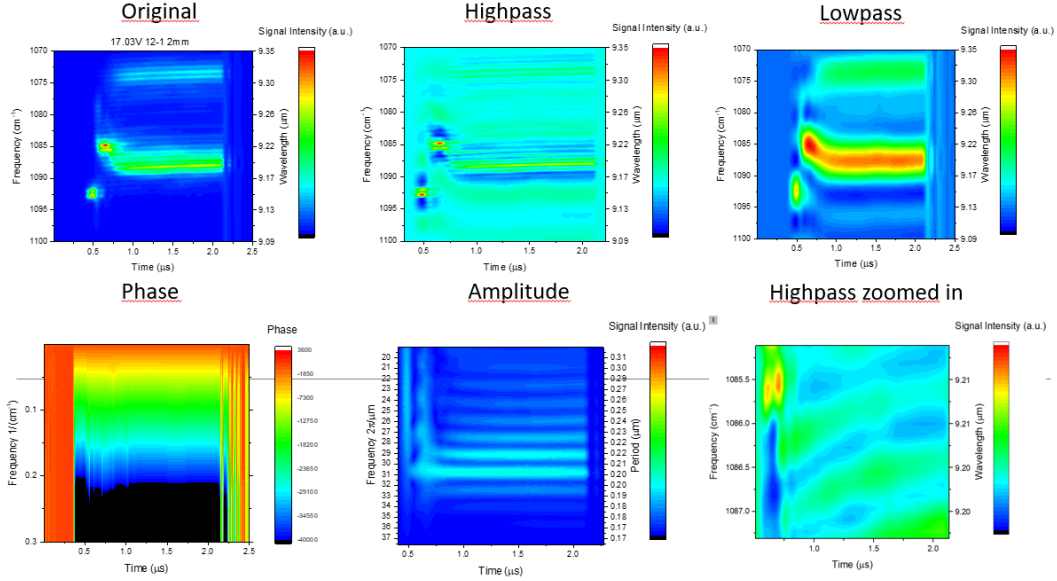


Figure 3.16: Fourier filtering to separate longitudinal FP modes.

Although the spectrum of a QCL may exhibit complex behavior with temperature and electric field, we observed that longitudinal Fabry-Perot modes in the spectrum evolve fairly regularly over time. The shift in the Fabry-Perot (FP) mode peaks seems relevant to heating of the laser. However, FP and lateral modes are overlapped in the spectrum. To separate them, we used high and low pass Fast Fourier Transform (FFT) filters. As shown in Fig. 3.16, highpass filter isolates the FP modes while a lowpass filter isolates the lateral modes. We also calculated the phase and amplitude of the spectrum. In the amplitude plot, we can calculate the frequency of the FP modes, which yield the effective index. The Fourier transform of the FP spectrum also is not purely sinusoidal. This detail may need further investigation and may be due to the FP spectrum being multiplied with the spectral gain curve of the laser, or, resolution of the FTIR is not adequate and cause these artifacts, or due to some non-linear term in the gain. In any case, the shift seems correlated with the temperature increase. From the time-dependent phase of the FFT of the spectra, we obtain the shift the FP-modes. We have also used Comsol Multiphysics to calculate the active region temperatures with respect to the input power (voltage x current) assuming all

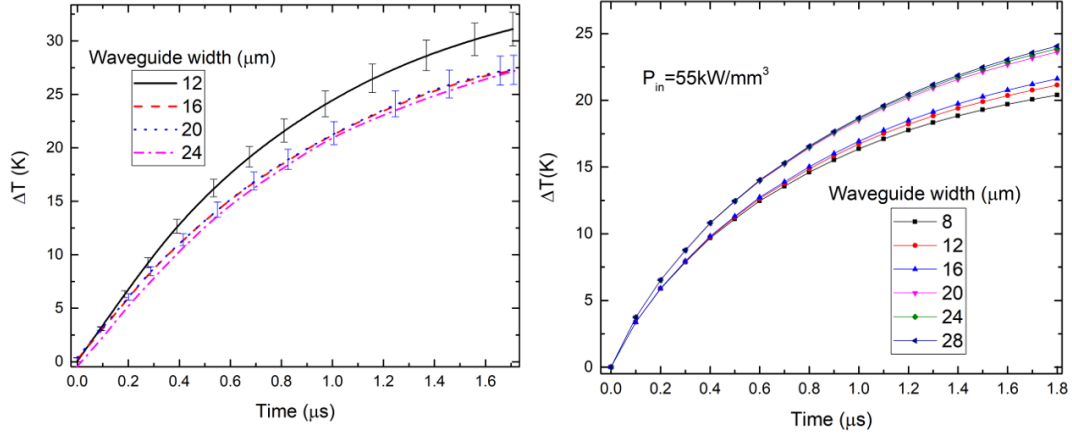


Figure 3.17: Measured and calculated cavity temperatures as a function of time for various waveguide widths.

input power is converted into heat in the active region (Fig. 3.17). The correlation of simulation with experiment is very good, however, the temperature dependency of the refractive index of the cavity needs to be calibrated to characterize the cavity temperature and thermal properties, precisely. For this reason, we added a temperature sensor and a heater to the copper holder of the laser within the dewar and controlled the temperatures using a PID temperature controller. Measuring the temperature dependence of the FP shift, it is possible to measure the cavity temperature with time and calculate the thermal resistance of the cavity. This measurement is also useful for our work on alternative materials for lossless passivation. The passivation layer may also act as a heat spreader, therefore characterization of thermal resistance may give us valuable information about the performance of the passivation.

3.3.3 Near field measurements

Characterizing near and far field of QCLs is essential for most applications since in general it is required to collimate the laser using a lens or mirror, or couple the light into a fiber or waveguide. Near field of a QCL basically refers to the optical power distribution on the plane of the laser output facet. Far field is the

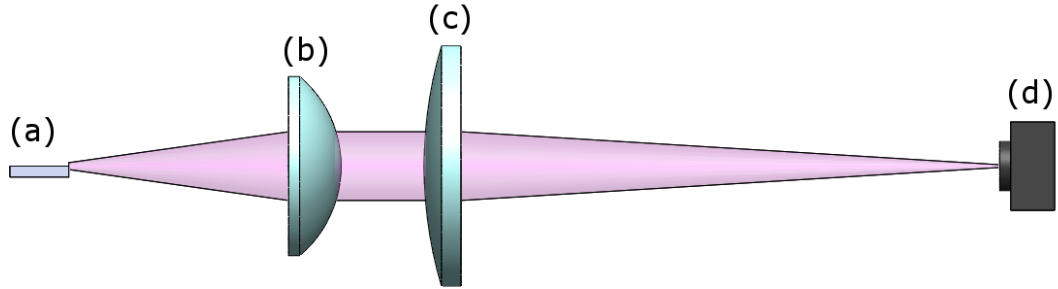


Figure 3.18: Experimental setup for near-field measurements.

angular dependence of the optical power as the distance the from facet goes to infinity but distances much larger than $\pi D^2/\lambda$, where D is the aperture, i.e. the waveguide width, and λ is the wavelength of the laser, is considered as far field. This number is in the order of 10-100 μm for QCLs, therefore a few centimeters away from the facet can be safely regarded as far field.

Fig. 3.18 shows the experimental setup for near field measurement we used. The laser (a) is collimated with a germanium lens (b) and refocused with another germanium lens (c) on the infrared sensor (d). We used a FLIR Lepton LWIR camera module as a sensor. Since this is a 2D array of sensors, it eliminates the need for scanning and images the optical field at once. Then we moved the camera along the propagation axis to obtain sections of the field along the axis. It is also possible to use a single element infrared sensor, such as an MCT photodetector with a pinhole and scan the detector in the horizontal and vertical axis to obtain a 2D profile of the optical power.

3.3.4 Voltage-current-power measurements

Electro-optical characterization of QCLs is essential for both optimization and understanding the underlying physics. Although these measurements and techniques appear relatively simple, one should take into account many factors to do

it accurately.

Long-wave QCL radiation is detectable by thermal cameras. There are low-cost thermal cameras in the market that could be used for a quick and easy tool for detection of lasing. We used a FLIR Lepton module connected to a Raspberry Pi computer as well as a FLIR TG165 hand-held thermal camera. These cameras detect lasing even at very low duty cycles. Lasing with a few μW of average power is easily detectable if the camera is positioned 5-10 cm away from the facet. Fig. 3.19 shows an example image taken with the FLIR Lepton. Thermal cameras help with alignment, observation of lasing angle and quick determination of voltage and temperature range at which the QCL lases.

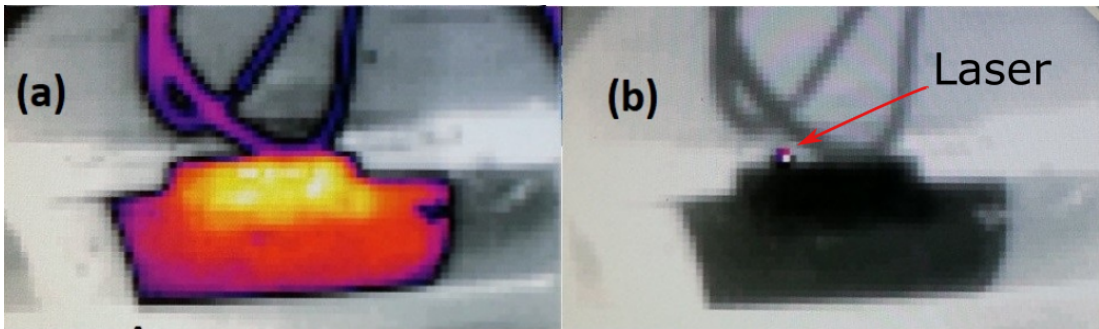


Figure 3.19: Thermal camera of a QCL mounted on a LN-cooled dewar below threshold (a) and above threshold (b).

Fig. 3.20 shows the experimental setup we used for current-voltage-power measurements for pulsed operation of lasers. We used an Avtech AVOZ-A3-B pulsed voltage source (a) for most of the pulsed measurements. QCLs are placed in a liquid nitrogen dewar (b) with a zinc selenide window (c). Output light is collected with a gold integrating sphere (d) connected to a liquid nitrogen cooled MCT photodetector (a). We used a two-channel oscilloscope with 500 MHz bandwidth to record current through a 1Ω resistor connected in series with the laser. The output of the photodetector is also recorded simultaneously through the second channel. Synchronization between the pulse source and the oscilloscope is established through a BNC connector between the sync output of the source and the trigger input of the oscilloscope.

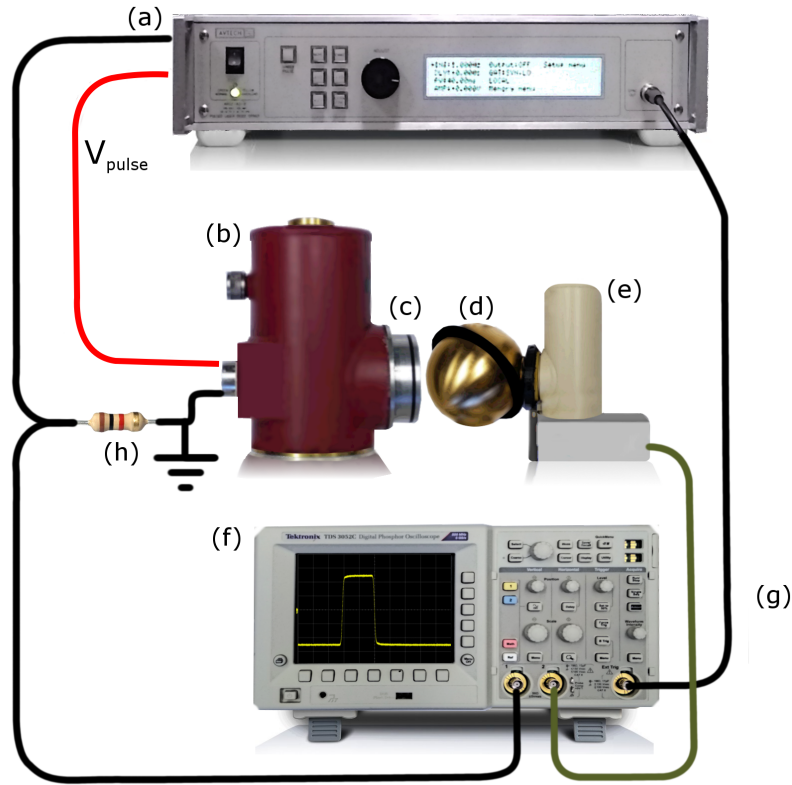


Figure 3.20: Experimental setup for pulsed Voltage current and power measurement.

Voltage and current waveforms observed on the oscilloscope are shown in 3.21. Due to impedance mismatch between the QCL and the pulse, as well as the impedance of the long (50 cm added length) connection cables, we observed a substantial amount of oscillations (ringing) in the voltage signal. Due to the added inductance, the current waveform has about 200 ns of rise-time. To reduce the impact of these, we only take in to account the values measured at the end of the pulse, where the voltage and current stabilize. We designed a Labview program to do this. This program basically sets the voltage, temperature etc. and reads the waveform and extracts the average values at the wanted time interval. Typically, we used 500 ns pulse width and recorded the averages at the last 50 ns of the pulse.

We also used Newport LDP-3839 current pulser occasionally. Since current

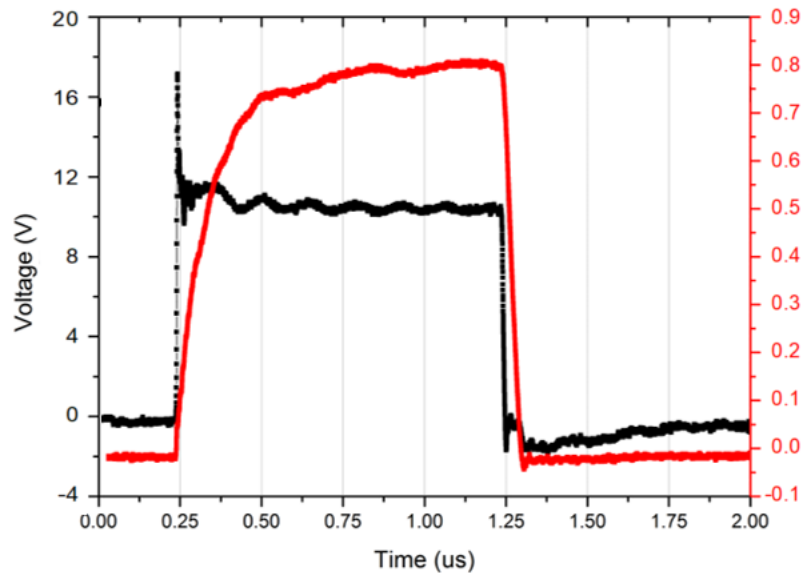


Figure 3.21: Voltage and current waveforms of 1 μ s pulse recorded by an oscilloscope.

pulsers apply constant current, instead of measuring the current through a resistor, we measured the voltage output. It should be noted that while measuring the output voltage, the ground connector of the oscilloscope probe should not be connected to either the anode or cathode of the pulser. This may cause failure of the pulser. Instead, two different probes on different channels should be used, one for the anode and one for the cathode. The voltage difference can be calculated using the math functions of the oscilloscope. Apparently many current pulsers gets damaged if one of the outputs is grounded. We guess the reason could be a current monitor resistor like the one in Fig. 3.20. When both sides of the resistor are grounded, the pulse cannot monitor the current and overloads the output. This is not the case for voltage pulsers, but they are prone to failure if the output is shorted.

As an alternative to the commercial voltage/current pulsers, it is possible to use a simple MOSFET switch circuit. We built a circuit using OIR2117 MOSFET driver and IRF530N MOSFET to switch DC lab power supplies. MOSFET driver was driven by a square pulse signal generator with 5V amplitude. With this circuit, we could achieve higher duty cycles and longer pulse width that is not

supported by AVOZ-A3-B or LDP-3830. Since the circuitry is smaller, connector cables were also shorter, which decreased the cable impedance. We measured around 140 ns current rise times with our circuit.

Chapter 4

Characterization of QCLs

In this chapter we present the electro-optical characterization of quantum cascade lasers designed and micro-fabricated in the Advanced Research Labs. of the Physics Department. We first discuss the current- voltage and power data followed by spectral characterization. We then, discuss temporal dynamics of the spectrum. We present the spectra as a function of voltage at various temperatures and discuss the possible instabilities and multi-mode regimes.

4.1 Elecro-optical characterization

The most basic features of a semiconductor laser are the relationship between current and voltage and optical power. In the case of quantum cascade lasers studied in this thesis, we pulse voltage bias the QCLs and measure current and optical power.

Fig. 4.1 shows the current and optical power as a function of voltage for 2 mm long Si_3N_4 passivated lasers for various ridge widths. The measurements were done at pulse-width of 500 ns and duty cycle of 0.5%. A typical current-voltage relationship of the lasers presented here consist of three regions; 1: Below turn-on voltage, 2: Linear region above turn-on, 3: Above breakdown voltage.

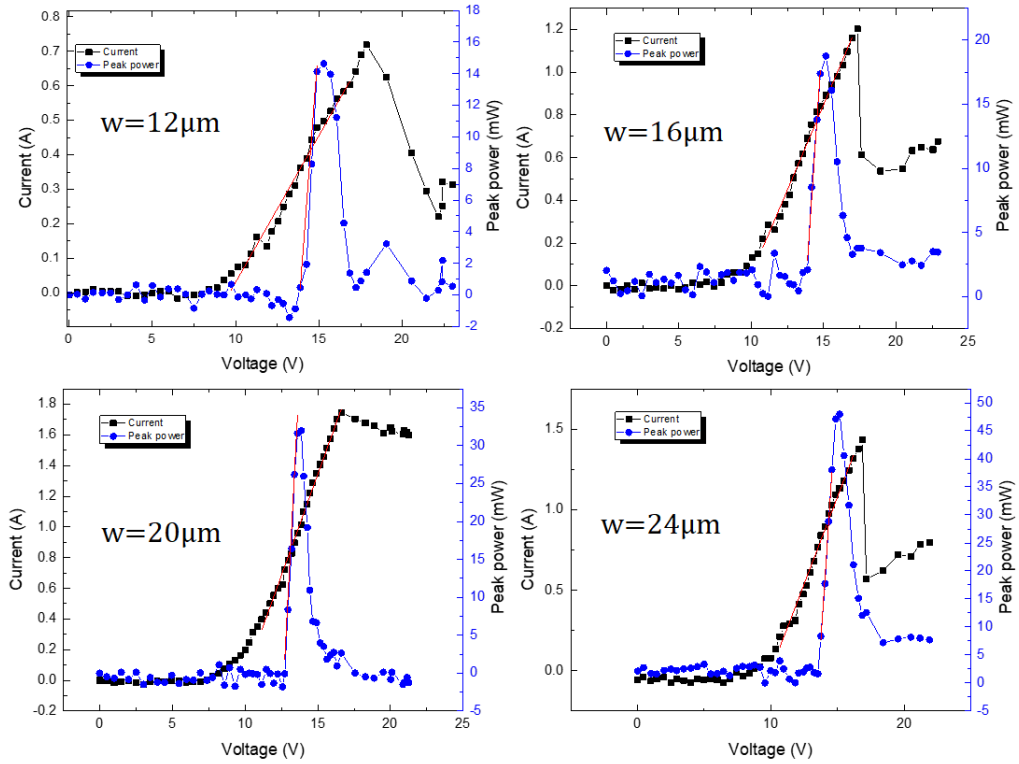


Figure 4.1: Voltage-current-power characteristics of QCLs with 2mm cavity length and various widths.

Below the turn-on voltage, resistance is high, of the order of a tens of $k\Omega$ s per mm^2 , between -170 to -100 $^{\circ}\text{C}$. Unlike a typical laser diode, a QCL is a unipolar device and has no built-in potential to overcome. However, at zero bias, the electronic states allocated for electrical conduction is not in alignment and hence no current can pass until the electric field is large enough to align the electronic states. As the voltage is increased, bending of the conduction band edges takes place until the relevant electronic states are in alignment to allow conduction. The voltage at which current starts to flow can be considered as a turn-on voltage. As the voltage is further increased, current increases with voltage due to the manifold of states taking part in the conduction. In this linear region, we observe that the slope resistance is about $500 \Omega/\text{cm}^2$. The transition from zero bias to onset of conduction requires a voltage of 10 V. The voltage limit at which lasing ceases is labeled as the breakdown voltage (BV), where further bending of electronic energy states causes misalignment of successive states involving the

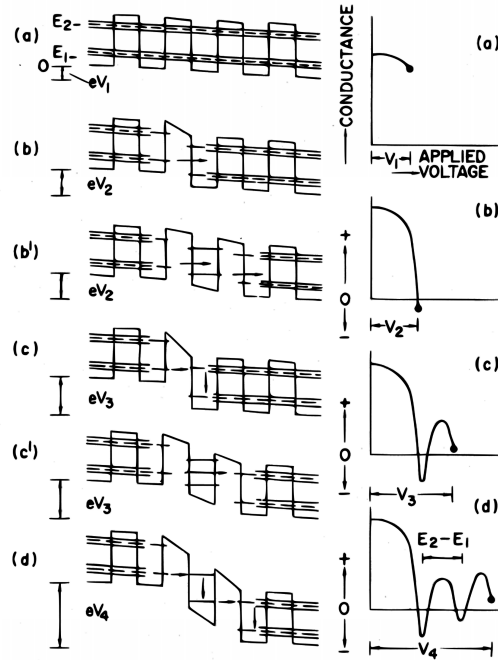


Figure 4.2: Diagram of alignment of band energy levels under increasing electric field resulting negative differential resistance.

Reprinted figure with permission from [L. Esaki, L. L. Chang, Physical Review Letters, 33, 8,1974.] Copyright 1974 by the American Physical Society.

lasing transition and current decreases as the voltage is increased further. BV is the onset of the negative resistance regime. The exact value of BV varies slightly from sample to sample and is typically between 16-18 V.

In the negative resistance region, active region periods may separate into different electric field domains due to space charge formation [76]. Space charge accumulates near the boundaries of the adjacent periods disrupting the potential of the quantum wells. Space charge cause discontinuities in the potential. To prevent early onset of negative differential resistance, the injection zone of the active region is n-doped [77]. Doping increases the conduction in the injection region and spreads the space charge [78]. In the breakdown regime, current-voltage characteristics are quite variable for different devices. For instance, 16 and 24 μm wide lasers without gold mirrors have a sharp fall in current above the breakdown voltage, while the 12 μm wide laser has smaller negative resistance (slope), and the 20 μm wide laser has even smaller values. We also observe a variability

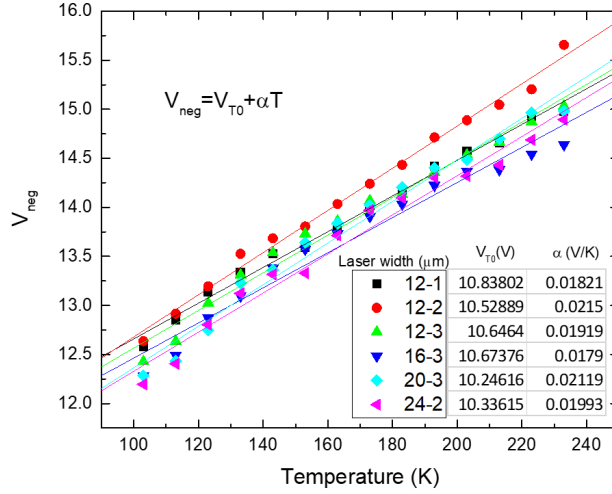


Figure 4.3: Turn-down voltage of the lasers with cavity length of 1.5mm as a function of temperature.

between two lasers with apparently the same geometry. Further data is needed to clarify the relationship between ridge width and negative resistance. For most lasers, we observe a second linear current-voltage region after the sudden end of negative resistance (clearly seen in Fig. 4.1 for a 24 μm wide laser). Such behavior is also explained for superlattices by Esaki and Chang.[79]. Fig. 4.2 shows the alignment of the bands of a superlattice under electric field caused by a potential bias. From 4.2a to 4.2d potential increases. Plots on the right are the voltage versus conductance graphs, where x-axis is the voltage and y-axis is the conductance. In Fig. 4.2(a) shows the energy levels under bias before the domain formation. In this region, electron transport occurs between the bands, while conductance decreases with the increased electric field. In (b) a domain boundary is spontaneously formed while conductance drops rapidly. At (c) conduction first increase, when the bottom energy level on the left matches with the top energy level on the right and decreases again as voltage rises. In (c') and (d) the domain expands to another period, creating another dip in the conductance.

To analyze the negative resistance region above the breakdown threshold, we measured the breakdown voltage of 1.5 mm HfO_2 passivated lasers with various widths as a function of temperature, Fig 4.3. There is a linear relationship between the breakdown voltage and temperature. Breakdown voltage rises as the

temperature increases. This supports the idea that the breakdown is related to active region doping. At lower temperatures, some fraction of dopants are not ionized, reducing the free electron density at the active region. This may decrease the threshold for the breakdown. From the linear fits, we calculated the V_{T0} , the breakdown voltage at 0 K, and the slope, α . Both parameters do not depend on the waveguide width. V_{T0} is approx. 10.5 V and α is approx. 0.02V/K.

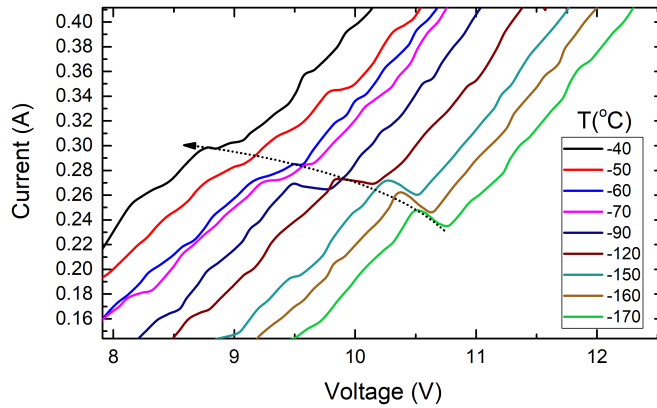


Figure 4.4: Turn-down voltage of the lasers with cavity length of 1.5mm as a function of temperature.

Further analysis of Fig 5.1 shows that there is also a smaller kink in current-voltage graph around 11V, Fig.4.1. The mechanism of this negative resistance is different from the one at higher voltages. This is due to resonant tunneling, which is explained by the alignment or misalignment of the energy levels of consecutive periods of active regions[78]. This is similar to the operation mechanism of a tunnel diode. An electron in the lower energy state in a period tunnel into the injection region, then into the upper state of the next period. Injection region is doped and in many designs has manifolds of energy states or minibands. When the energy of the electron in the injection region and the upper state of the next period is the same, resonant tunneling occurs. Tunneling rate increase as the energy difference between the initial and lower state gets smaller. Therefore resonant tunneling increases the injection rate. Electron tunneled into the injection region thermalize in the manifold of states which facilitates resonant tunneling. Fig. 4.4 shows the current-voltage graph at various temperatures displaying the

resonant tunneling peak. This data is from a 24 μm wide, 1.5 mm long, HfO_2 passivated laser. Resonant tunneling peak becomes broader with increasing temperature and moves towards lower voltages. Since the density of states in the injection region is narrower at lower temperatures, we observe quenching of the resonant tunneling at these temperatures. This observation is in good agreement with the literature [78].

Further, in Fig. 4.1, voltage-optical power or current-optical power relationship in lasers without dielectric mirrors exhibit a steep rise above the threshold current and after the peak power, drops rapidly. 12 μm wide laser shows a second rise after the power drops, and this rise is at the negative resistance regime. This is probably the activation of a second mode. The offset in the power below the threshold current is due to the dark current of the detector and the background radiation. The red lines on optical powers shown in Fig. 4.1 are the linear fits to the rising edge of the current-power relationship. From these linear fits, we calculated the slope efficiencies, which are proportional to quantum efficiencies. Slope efficiencies of various lasers with different passivation materials and waveguide widths are further analyzed to calculate cavity losses in the next chapter. However, we should note that the optical powers measured here are average powers over many voltage pulses. As we show in the time-resolved spectral measurements, optical power and modes vary during the pulse. Since the optical powers are average, power as a function of voltage seem to drop slowly after reaching the maximum of the peak power. However, as we observe on the time-dependent spectra shown in the section 4.2, at a certain voltage emission cease abruptly. Current-voltage-power data here was measured using a calibrated slow MCT detector, therefore the power is averaged over the pulse width. During the rise and fall of the pulse, the laser emits light briefly, even if the peak voltage of the pulse is above the emission range. This cause a small signal in the averaged detector output.

Table 4.1 lists the various parameters extracted from Fig. 4.1 to show typical values, ranges and trends with respect to ridge width. Note that the width is the ridge width at the top of the waveguide, and due to the wet-etched wall profiles, actual active region widths are approximately 4 μm wider than the indicated

Table 4.1: Parameters derived from current-voltage-power measurement of QCL

Width	$12\mu m$	$16\mu m$	$20\mu m$	$24\mu m$
Threshold voltage (V)	13.84	13.72	12.67	13.54
Threshold current (I)	0.35	0.64	0.73	0.74
Slope (mW/V)	14.1	16.9	36.7	36.1
Slope efficiency (mW/A)	166	105	139	171
Turn-on voltage (V)	9.64	9.68	9.89	10
Slope resistance (Ω)	11.8	6.28	3.8	4.76
Reverse breakdown voltage (V)	17.85	17.33	16.62	16.85
Max. power (mW)	15	19	32	48
Max. power @ (V)	15.28	15.15	13.68	15.16
Max. power @ (I)	0.48	0.87	0.99	1.08
Wallplug efficiency (%)	0.20	0.14	0.23	0.29

values. The threshold current is between 0.35 and 0.74 A. which corresponds to $1.09\text{kA}/\text{cm}^2$ and $1.32\text{kA}/\text{cm}^2$.

Slope efficiencies were calculated for the maximum optical power. It tends to increase with the waveguide width but is also high for $12\mu m$ wide laser. As explained in detail in the next chapter, for a given waveguide mode, loss due to passivation dielectric decrease with increasing ridge-width. However, $12\mu m$ wide laser is close to single mode operation, therefore, it has less mode overlap with the dielectric leading to a reduced loss.

Turn-on voltages in Table 4.1 are calculated from the intersection of the voltage axis with the linear fit to the current-voltage in the linear region. It is around 10V and small variations are probably due to experimental errors. Wall-plug efficiencies are around 0.2%. This value is much smaller than the theoretical limit of 40% [80], therefore, there is much room for improvement for this QCL design.

To examine the effect of heating and to find the maximum average power achievable, we scanned pulse widths and duty cycles of the voltage pulses for lasers with different widths and measured the average optical powers. From the average powers with known duty cycle, we calculated the average peak powers. Fig.4.5 shows the resulting colormap plots. Color indicates the optical power

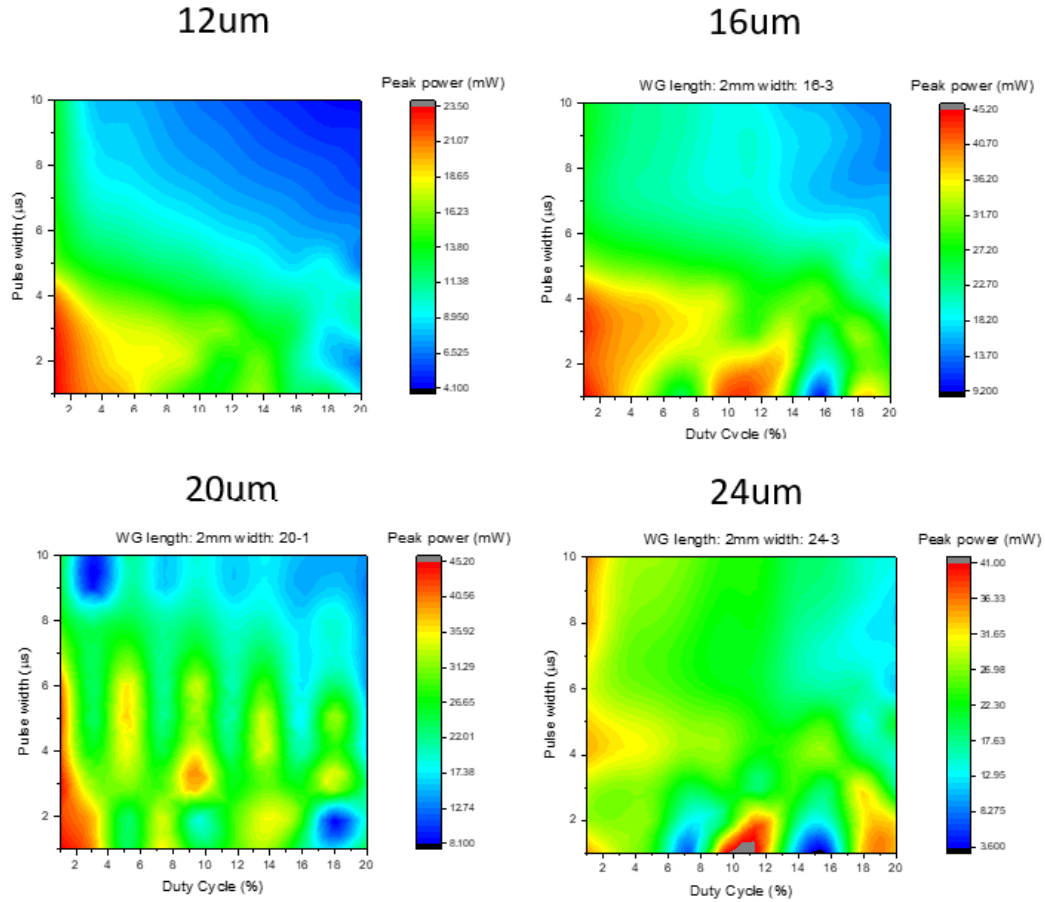


Figure 4.5: Optical power of Si_3N_4 passivated QCLs as a function of pulse width and duty cycle.

intensity while the horizontal axis is the duty cycle and the vertical axis is the pulse width. These are measured using constant voltage pulses of 15V. Heat sink temperature is about -170°C . Since the voltage is constant, we expect the change in optical power to be mostly temperature dependent. For low duty cycles, it is assumed that the substrate temperature is equal to heatsink temperature. In this regime, after the initiation of the voltage pulse, the temperature rise is confined to the active region. This is because of the low thermal conductivity of the active region compared to the substrate. At the lowest duty cycle of 1%, for most of the lasers, peak powers stay constant up to $4\mu\text{s}$ pulse widths. For higher duty cycles, we expect the substrate temperature to rise significantly. In this regime, active region temperature at the beginning of the pulse is dominated by the thermal conductivity of the substrate (InP) and the thermal barrier between the substrate

and the heatsink (indium solder). Peak power values along the line of $1\mu\text{s}$ pulse width as a function of duty cycle shows the temperature dependence of the peak power, approximately. For $12\mu\text{m}$ wide laser, optical power decreases steadily with increasing duty cycle, but, for the other lasers, optical power decreases and increases as the duty cycle changes. This may be the result of activation of different optical modes at different temperatures. To clearly observe the effect of these modes, it is useful to explore the spectrum-temperature relationships.

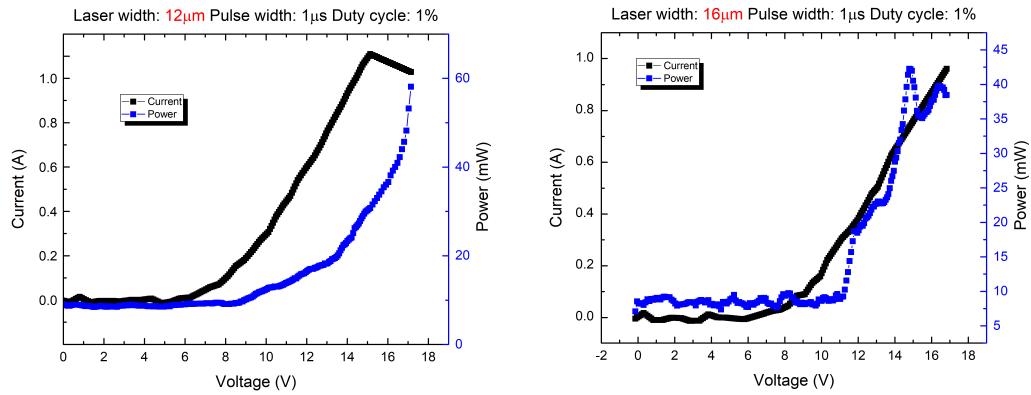


Figure 4.6: Voltage-current-power characteristics of QCLs with 2 mm long cavity length with mirror at the back facet.

We also fabricated lasers with high-reflective gold mirrors on the back facets. Voltage-current power characteristics of two of those lasers are shown in Fig 4.6. Mirrors significantly reduce the threshold for lasing. $12\mu\text{m}$ mirrored laser starts to lase around 9 V-200 mA and $16\mu\text{m}$ laser starts at around 11 V-320 mA, while the non-mirrored ones start to lase at around 13.8 V. Threshold current is reduced to almost two times, and slope efficiency almost doubled. As a result, mirrored lasers operate at a wider voltage range.

4.2 Spectro-temporal measurements

Emission spectra of lasers provide much sought-after information on the laser dynamics. QCL spectra exhibit a wide range of physical phenomena, such as

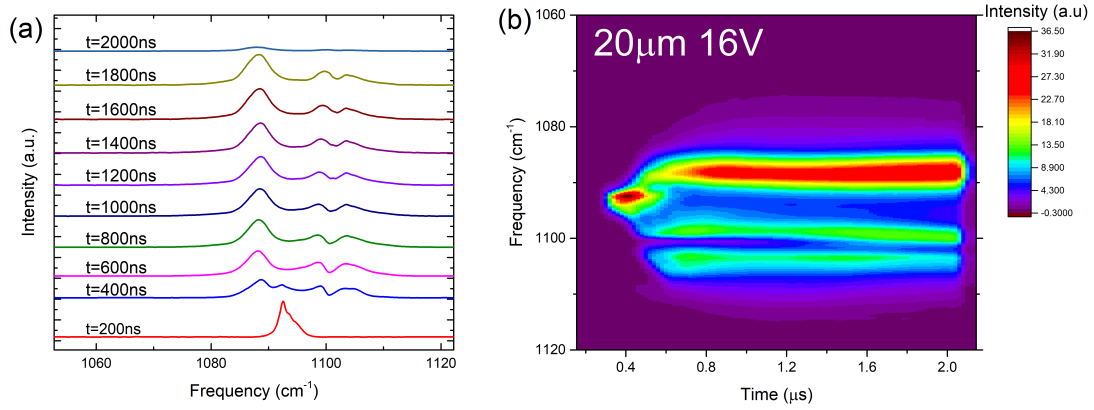


Figure 4.7: Time resolved spectrum of a QCL with 20 μm waveguide width and 3.8mm cavity length at 2 μs long 16V voltage pulse.

the occurrence of longitudinal and lateral waveguide modes, as well as gain saturation, saturable absorption, mode hopping, temperature dependent gain and the like. Many parameters such as voltage, temperature, cavity geometry, loss due to passivating insulators and contact metals affect the QCL spectra. In this section, we are going to examine the spectra of various lasers with different cavity geometry as a function of temperature and voltage. Further, the step-scan technique provides temporal information with high resolution. Using the step-scan approach, we measured many spectra, sweeping voltage, and temperature. Fig. 4.7 shows the spectrum of a QCL at various time slices. This data was recorded with 20 ns time resolution and 0.5cm^{-1} spectral resolution. The laser is a 3mm long $20\mu\text{m}$ wide HfO_2 passivated structure, and operating at approximately -160°C . Fig. 4.7(a) shows the stacked spectra in with 200 ns time steps while 4.7(b) shows the same data in colormap format with 20 ns steps. Color indicates the light intensity and scale is shown on the right. Since the color map representation is more compact, it is possible to present more detail with it, so we preferred this format in most of the following spectral data.

Fig. 4.8 shows the heat map of time-resolved spectra at different pulse voltages for 1.8mm long $24\mu\text{m}$ wide QCLs. The applied pulse width is $2\mu\text{s}$. Time scale starts when the voltage pulser triggers the FTIR spectrometer. Voltages shown on the figures indicates voltages set on the voltage pulser and voltages are expected to be less on the lasers due to series resistance. Lasing starts at around $0.5\mu\text{s}$ and

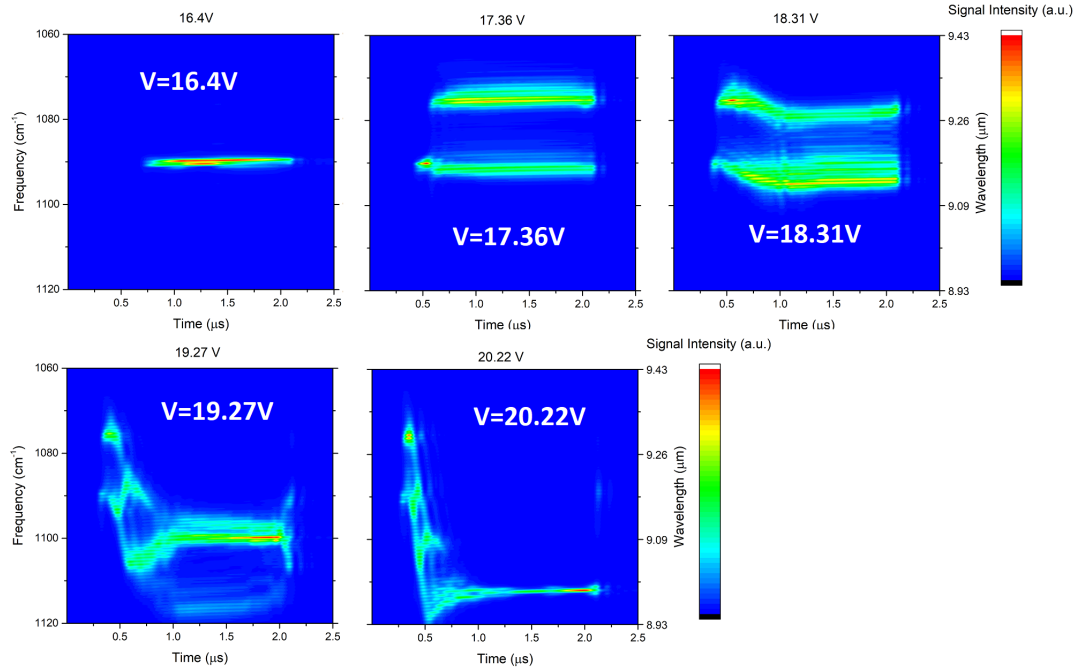


Figure 4.8: Time resolved spectrum of a QCL with 24 μm waveguide width and 1.8mm cavity length at various 2 μs long pulse voltages.

continues until about 2 μs . There is a rise time of $\approx 250\text{ns}$ and stabilization time of $\approx 100\text{-}200\text{ns}$ of the voltage pulses, and from the spectra, we can assume that the voltage is stable after 750ns, because 16.4V is the lasing threshold for this laser, and lasing starts at about 750ns at this voltage. After 750ns, we assume the changes in spectra are temperature related. As we will show in the next section temperature rise in the active region is significant, even in pulsed operation.

Lasing just above the threshold exhibits a single mode, with a single narrow peak at about 1090 cm^{-1} ($9.17\ \mu\text{m}$), but closer examination reveals three smaller peaks. The small peaks are due to longitudinal Fabry-Perot (FP) modes between two laser facets. These modes are observable in almost all spectra, as long as the spectral resolution of the FTIR is adequately high. At 17.36 V another mode appears around 1075 cm^{-1} ($9.30\ \mu\text{m}$). At 18.31 V another mode around 1100 cm^{-1} and at 20.22 V another mode at 1115 cm^{-1} appears. For the 24 μm laser, in total, 4 modes are observed, but the mode at 1075 cm^{-1} is activated only when the main mode at 1090 cm^{-1} is active. For the case of 12 μm wide laser, Fig.4.9;

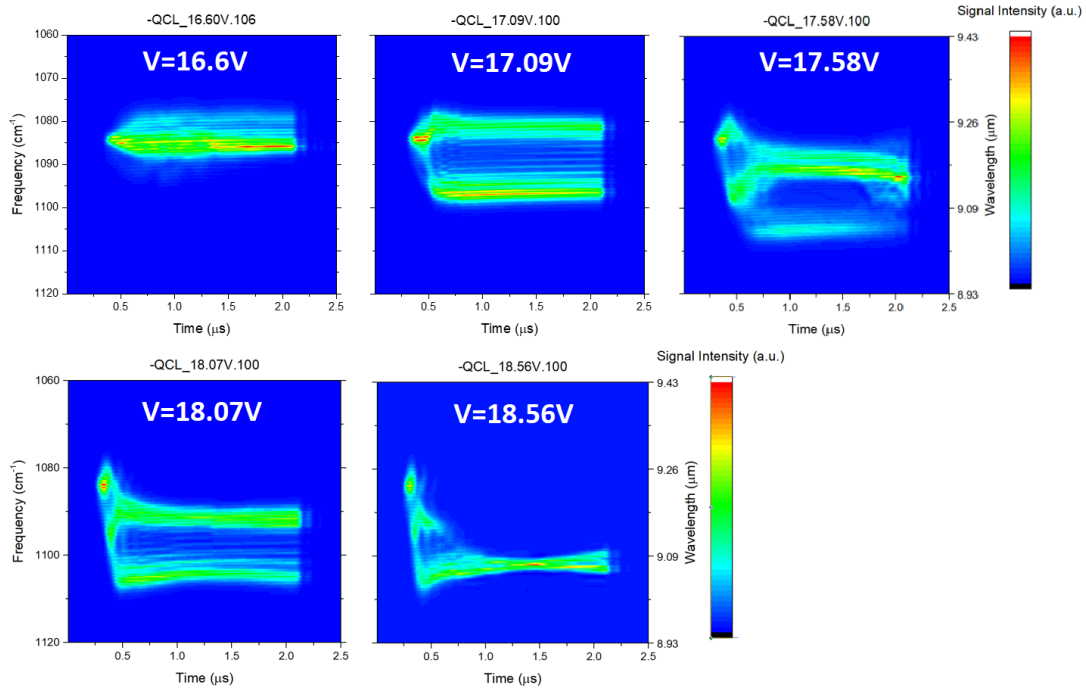


Figure 4.9: Time resolved spectrum of a QCL with 12 μm waveguide width and 1.8mm cavity length at varied 2 μs long pulse voltages.

there are only 3 modes, and the mode at 1075 cm^{-1} is not observed.

The fundamental mode of a waveguide is the one with the largest effective index amongst other modes. We also expect that the fundamental mode to have the lowest loss and lowest threshold for lasing. For this reason, we assume the peak at 1090 cm^{-1} is due to fundamental lateral cavity modes. Starting with a single longitudinal mode, this mode gets broader as the voltage gets larger. This phenomena is due to spatial hole burning and caused by gain saturation at the nodes of the standing wave of the longitudinal modes [81].

At 17.09V the spectrum splits into two peaks. This is suggestive of Risken-Nummedal-Graham-Haken (RNGH) instability. RNGH instability is a coherent phenomenon that results from short gain recovery times (a few picoseconds) combined with saturable absorption in the active region[81, 82]. The oscillation seen at resonance in superlattices between the minibands of a semiconductor superlattice are Rabi oscillations[83]. The source of RNGH instability is similar in nature

where population inversion oscillates with Rabi frequency and modulates gain. RNGH is related to self-pulsing where under certain laser parameters stationary solutions to the laser equations do not exist and build up of a pulse is observed.

In the RNGH instability regime, the emission spectrum splits into two peaks separated by the Rabi frequency;

$$\Omega_{rabi} = \mu E / \hbar = \mu \sqrt{2nI_{avg}/(c\epsilon)} / \hbar \quad (4.1)$$

where n is the background refractive index, μ is the transition dipole element, I_{avg} is the average optical intensity in the cavity. Frequency splitting between the peaks is around $18 \text{ cm}^{-1} \approx 0.5 \text{ THz}$. Photons of these two frequencies are coherent, which leads to the laser output being modulated at half of this frequency. Note that RNGH instability is different from mode-locking. In the mode locking case, the modulation frequency is determined by cavity round trip time. Cavity round trip time for these lasers are;

$$\tau_{rt} = 2 * n * L/c \approx 2 \times 3.1 \times 1.8 \times 10^{-3} / 3 \times 10^8 \approx 3.72 \times 10^{-11} s = 37.2 ps$$

which corresponds to a value of $\approx 27 \text{ GHz}$ which is an order of magnitude less than the frequency splitting. Spectra shown in fig 4.8 at 18.31 V and Fig. 4.9 at 17.58 V evolve with time, even after $1 \mu s$. Since it is expected that the voltage is stable at this time, this time evolution of the spectra could be temperature dependent. For this reason, we extended our voltage-dependent spectral analysis and included the substrate temperature as a parameter. We stabilized the temperature of the QCL heat sink inside the dewar using a heater, a thermistor, and a PID controller. We set the voltage of the pulses using a Labview code and scanned through the lasing voltage range and measured time-resolved spectrum at each voltage step. Spectral resolution for these measurements were 2 cm^{-1} and time resolution was 50 ns . Voltage steps were around 0.1 V . We first identified the voltage range in which laser lases, then divided this range into 20 steps for each laser. Pulse length was $1 \mu s$ and duty cycle was 0.5% . Then, we extracted the spectrum at 500 ns after the pulse started. 500 ns seems to be an optimal trade-off time between the temperature rise in the active region and stabilization of the voltage pulse. We merged these spectra into 2D color map plots, as shown in Fig. 4.10, 4.11 and 4.12.

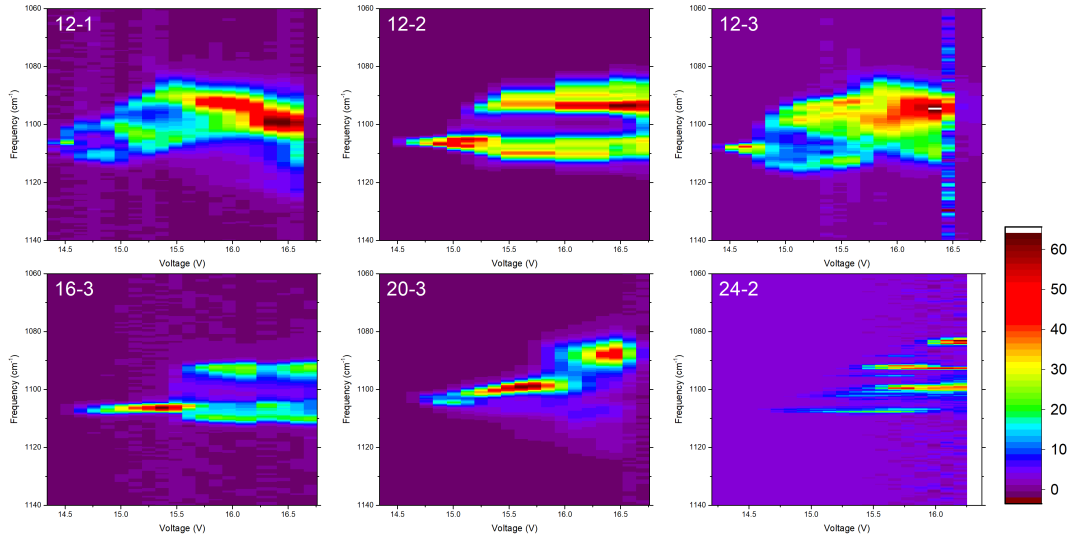


Figure 4.10: Spectrum of 1.5mm long QCLs as a function of applied voltage at -170°C .

Fig 4.10 shows the spectra measured for lasers with various ridge width and 1.5mm cavity length at -170°C . These lasers were passivated with HfO_2 and as will be shown in the next chapter, these have approximately half the cavity loss of the Si_3N_4 passivated ones. The vertical axis on each plot shows the frequency, in wavenumbers. The horizontal axis shows the pulse voltages. Color indicates the intensity of the light signal. The color scale is linear and shown in Fig. 4.10 with arbitrary units. Each figure is normalized to fit this color scale. Ridge widths are 12, 16, 20 and 24 μm and shown on the top left of each plot. All lasers are on the same laser bar and measured one at a time. There are three different, but geometrically same lasers with 12 μm to show variability between the lasers. Lasers were measured up to the voltages where lasing stops. End of the lasing is generally is at an abrupt voltage, as clearly seen in 12-1 and 20-3 lasers.

Note that periodic features of Fabry-Perot modes are not apparent in these figures, because the spectral resolution used in these experiments is larger than the period of Fabry-Perot modes. Spectral resolution is lower than the spectra in 4.9 to reduce the time required to finish many measurements. We limit the discussion here, to the lateral modes and instabilities, which have broader spectral features.

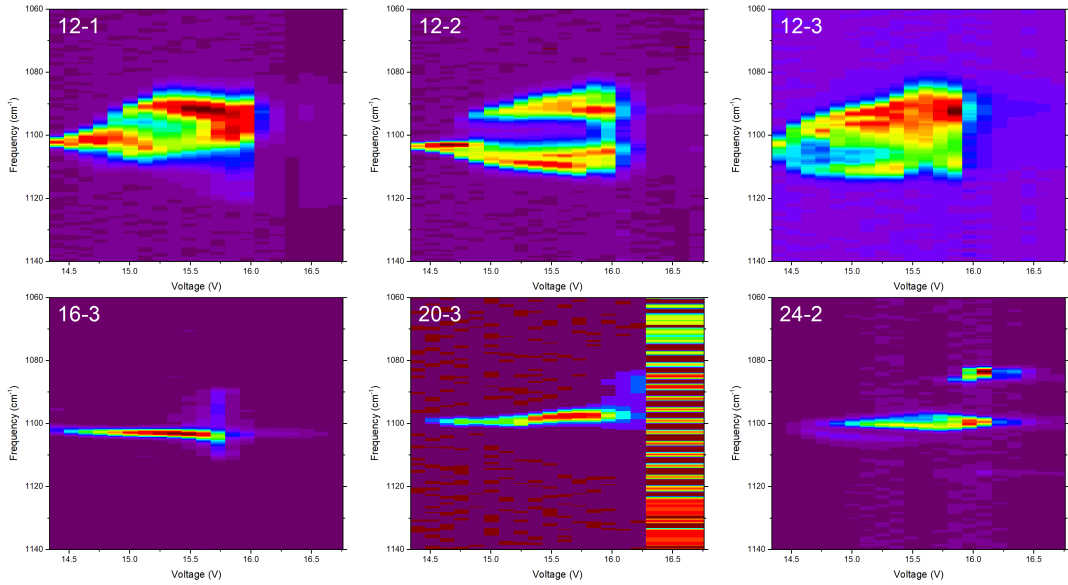


Figure 4.11: Spectrum of 1.5mm QCLs various voltages as a function of applied voltage at -155°C .

In all of the lasers, lasing right above the threshold has a single longitudinal Fabry-Perot mode. This mode is at about $1106 \pm 1 \text{ cm}^{-1}$. The spectrum of the 12-1 laser is split into two peaks at about 14.7V. Difference between the two peaks is about 10 cm^{-1} . Then the peak at 1100 cm^{-1} broadens and splits again into two new peaks at around 15.25V with a spectral difference of 14 cm^{-1} . These peaks gradually merge at around 15.7V to form a broader peak. 12-3 exhibits similar features; First, the initial mode broadens, then splits at around 14.7V and merges into a broader peak. However, 12-2 has a significantly different spectrum, it broadens first, and splits at about 15.25V. But, unlike the splittings shown in 12-1 and 12-3, the second peak appears abruptly, while the initial peak continues to broaden. For $12 \mu\text{m}$ wide lasers, splittings become more apparent with increasing temperature. For all of these $12 \mu\text{m}$ wide lasers, two phenomena are clearly observed; as the voltage increases, spectrum generally broadens, due to spatial hole burning, and again spectrum splits abruptly with increasing voltage due to RNGH-like instability. These two phenomena seem to occur simultaneously in the same laser and sometimes at the same voltage.

The spectrum of the $16 \mu\text{m}$ wide laser starts with a single mode and broadens

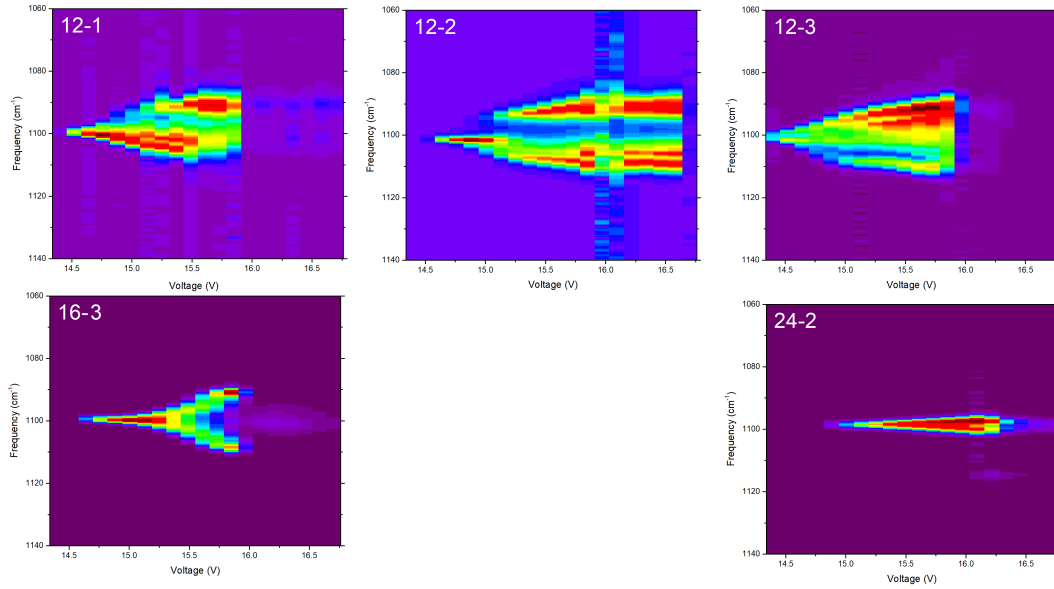


Figure 4.12: Spectrum of 1.5mm QCLs various voltages as a function of applied voltage at -140°C .

slightly, up to 15.5V. After that, another mode appears. For the $20\ \mu\text{m}$ wide laser, a mode hopping behavior is seen with a small overlap between these modes. The spectrum of the $24\ \mu\text{m}$ wide laser is displaying four modes with very little gain saturation. As the voltage gets higher, modes with lower frequencies get activated. It was also reported by Gordon et. al. [81] that lasers with broader area tend to show less spatial hole burning and RNGH instability.

Voltage bias in these measurements actually affect the spectra by changing the gain in the active region. However, gain also depends on temperature. Temperature can, for example, alter the gain by thermal back-filling of the electrons in the lower energy states of the laser or reducing the injection efficiency. We expect the gain to decrease with temperature in general; this is also indicated by pulse width-duty cycle-power measurements shown in Fig 4.5. To analyze the temperature effects, we increased the substrate temperature to $-155\ ^{\circ}\text{C}$ (Fig. 4.11) and $-140\ ^{\circ}\text{C}$ (Fig. 4.12). For all lasers, the voltage at which the lasing stops decreases with the temperature.

Rabi frequency increases proportionally to the square root of the light intensity

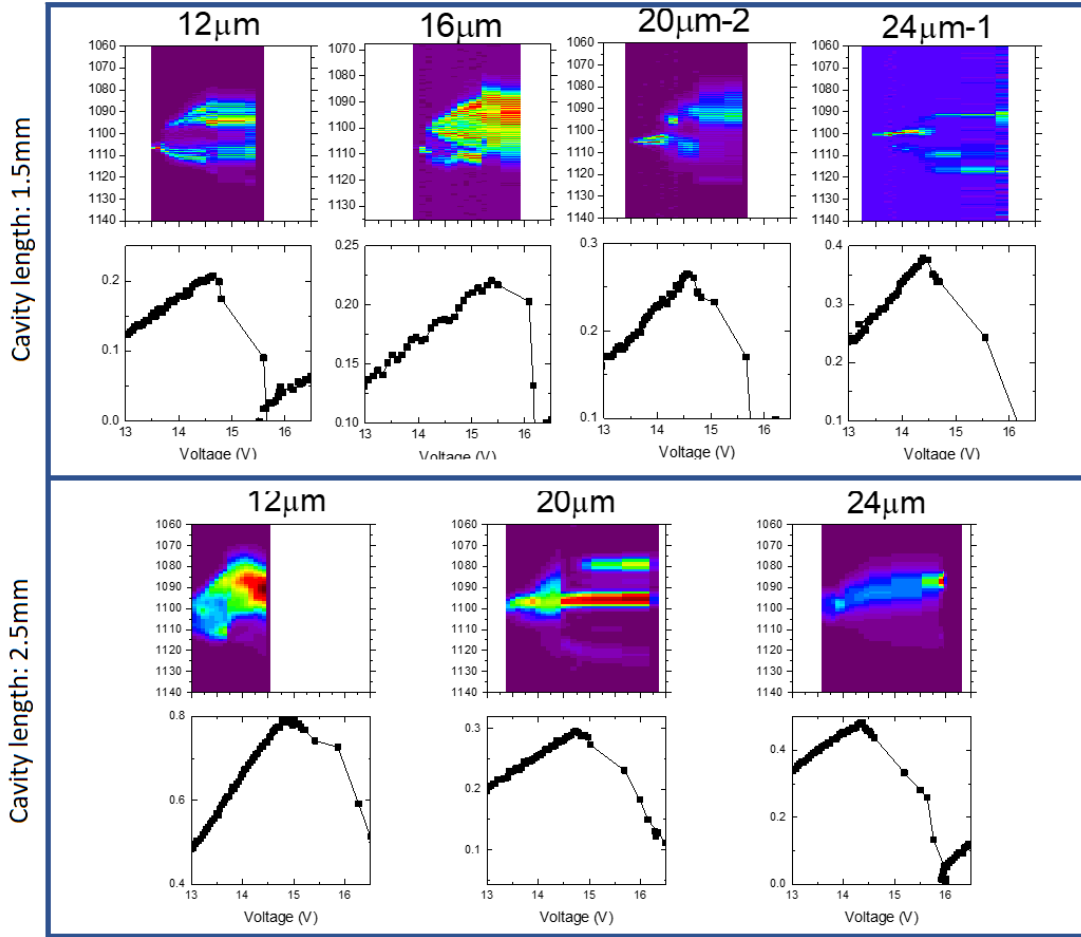


Figure 4.13: Spectra of 1.5mm QCLs as a function of applied voltage

in the cavity (Equation 4.1). This is clearly seen in Fig. 4.12 for 12 μm wide (12-2) and 16 μm wide lasers. Fig. 4.14 shows the frequency splitting measured from the data shown in 4.12 for 12-2 as a function of optical power. Central frequencies of two peaks were found by fitting a Gaussian function to each peak. Optical power is calculated from the integral of the spectra and has arbitrary units. Black squares are the measured data and the red line is the fitted function $\Delta f = a\sqrt{I}$, where a is the fitting parameter. Rabi frequency-power relationship is consistent with the predicted behavior. If the absolute power is calibrated, it is also possible to calculate the transition dipole element from the fitting parameter. Further data and analysis are needed to clarify this phenomenon.

In addition to the gain, the onset of the negative differential resistance (NDR)

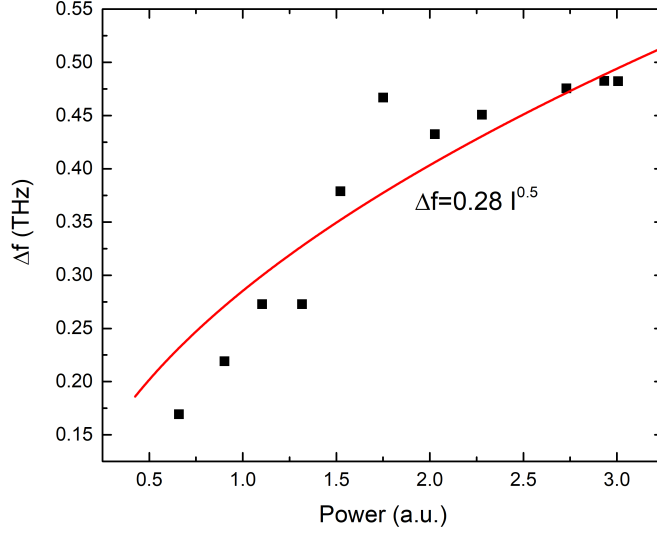


Figure 4.14: Frequency splitting of 1.5 mm 12 μm laser at $-140\text{ }^\circ\text{C}$ as a function of laser power.

may affect the modes and cause instabilities. This phenomenon has been studied for THz QCLs by Allen et. al.[84] and optical bi-stability was observed which was attributed to photon-assisted current transport. Fig.4.13 shows the voltage-dependent spectra of 1.5 and 2.5 mm long cavity lasers with varied widths. Voltage-current measurements were shown under each voltage-spectrum plot. Voltage axis is common for current and spectrum graph, and it indicated the voltage measured near the laser with an oscilloscope. Spectrum, voltage, and current were measured at 500ns after the beginning of the pulse. Negative resistance seems to affect the spectrum. 2.5 mm - 12 μm laser stops lasing just before the onset of NDR. 2.5 mm - 20 μm laser exhibits an abrupt change in the spectrum and 1.5 mm - 20 μm and 1.5 mm - 24 μm lasers switch from single mode to multi mode at the onset of NDR. However, it requires more data and further analysis to conclude which of these are relevant to NDR.

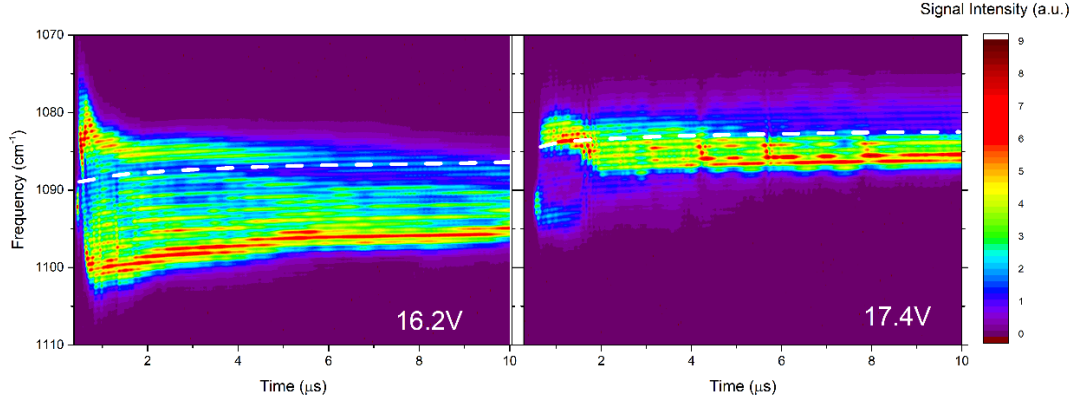


Figure 4.15: Time resolved spectrum of a QCL displaying shift of longitudinal FP modes at two different biases.

4.3 Thermal characterization

Both electrical and spectral characteristics illustrate that temperature is a very significant parameter for physics of QCLs. In this section, we present the results of the technique we used for characterization of QCL active region temperature.

QCLs have very complex spectral features as shown in the previous chapter. Spectrum depends on many factors such as voltage, current, temperature, cavity loss, cavity length, and waveguide geometry. However, the position of Fabry-Perot modes is mainly determined by the temperature of the cavity. Fig. 4.15 shows the time-resolved spectra of a QCL at two different voltage pulses. Pulse length is $10 \mu\text{s}$. Spectral resolution is 0.5 cm^{-1} . Although these belong to the same laser, they are different from each other. However, the shift of the Fabry-Perot modes is similar. White dashed lines on the graphs show the shift of the modes with time.

To characterize the frequency shift of the modes as a function of temperature we varied the heatsink temperature and measured the frequency shift at the beginning of the pulse. Duty cycle is 0.5% to keep the temperature rise of the substrate low. We assume the heatsink temperature is close to the actual temperature of the active region at the beginning of the pulse. The laser used has a 2 mm long $12 \mu\text{m}$ wide Si_3N_4 passivated cavity. Fig. 4.16 is the plot of

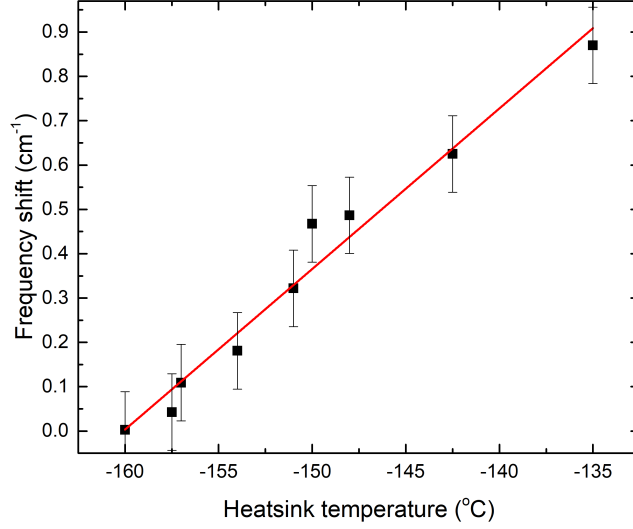


Figure 4.16: Shift of the Fabry-Perot modes as a function of heatsink temperature.

the measured frequency shift as a function of the heatsink temperature. The red line is the linear fit to the data. From the linear fit, we calculate the calibration constant between the frequency shift as

$$\alpha = 0.036 \pm 3 \times 10^{-3} \text{ cm}^{-1} / ^\circ\text{C}. \quad (4.2)$$

This calibration constant enables us to calculate the temperature rise with respect to the heatsink temperature as a function of time. Fig. 4.17 shows the time-resolved temperatures measured from the shift using the calibration constant at varied heatsink temperatures. This data is taken using the same laser used for calibration, under the same conditions. Each curve starts at the initial temperature equal to the heatsink temperature and rises steadily. At -77°C laser stops, so it can not be measured. Temperatures as a function of time are in the form of

$$T(t) = T_0 - \Delta T_{max} * e^{-t/t_0}$$

Fitted functions shown on the graph with dotted lines. Fitted values of t_0 is about $1 \pm 0.5 \mu\text{s}$. t_0 is the rise time of the temperature. At that time, the laser reaches to $1/e \approx 37\%$ of the maximum temperature rise, ΔT_{max} . Fitted value for ΔT_{max} is $50 \pm 5^\circ\text{C}$. $T_0 - \Delta T_{max}$ is the offset temperature, i. e. the heatsink temperature.

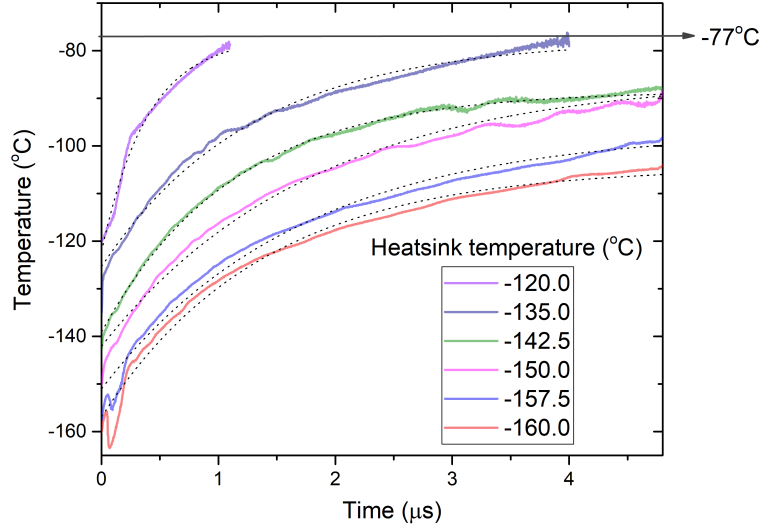


Figure 4.17: Time resolved average cavity temperatures at different heatsink temperatures.

At all heatsink temperatures, cavity temperature initially rises rapidly, followed by saturation. For higher temperatures, we can only follow the temperature until lasing stops.

Fig. 4.18 (a) shows the temperature of the cavity of the same laser in Fig. 4.17 at varied duty cycles with approximately $5 \mu\text{s}$ of pulse width. However, the heatsink temperature was fixed at $\approx -145 \text{ }^\circ\text{C}$. Similar to Fig, 4.17, time dependence of temperature is exponential. Although the heatsink temperature is fixed, initial temperatures increase with the duty cycle. This is due to increased heat flow causing the substrate to heat above the heatsink temperature. Cavity temperatures at the beginning of the pulse as a function of the duty cycle is shown in Fig 4.18(b). Black dots are the experimental data, and the red curve is a Boltzmann sigmoid function fitted to the data to guide the eye. We expect the cavity temperature to be close to the heatsink temperature at low temperature, and converge to a maximum value (i. e. the cavity temperature at continuous wave operation) at high duty cycles. The sigmoid function converges to approximately $-120 \text{ }^\circ\text{C}$. However, more data may be needed at higher duty cycles to estimate the temperature rise for continuous wave operation, more accurately.

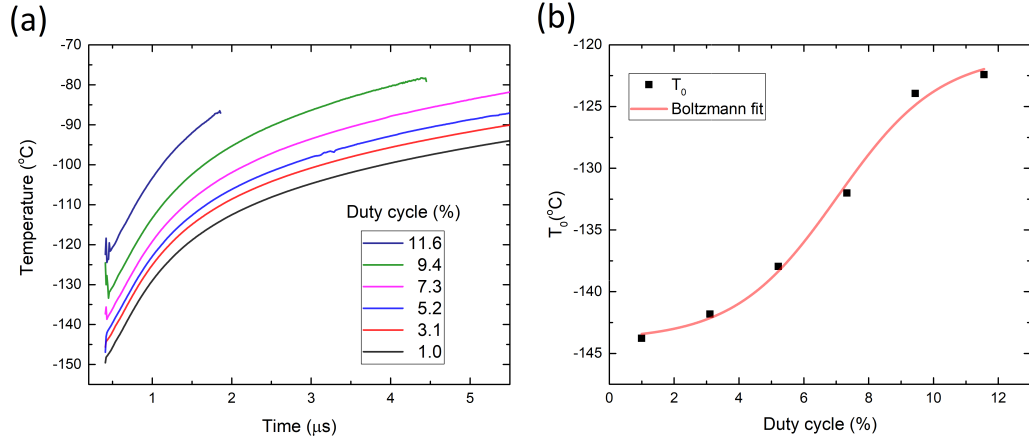


Figure 4.18: Time resolved temperatures at different duty cycles (a). Initial temperatures as a function of duty cycle (b).

Using the calibration constant we measure, we can calculate the temperature rise of the cavity. However, since the temperature is not spatially uniform, the measured temperatures are actually an average of the temperature distribution in the cavity. We assumed the temperature distribution is independent of the z position (in the direction along the cavity). Then we define the temperature as a function of x (in the out of plane direction) and y (in plane and perpendicular to x and y) positions; $T(x, y)$. FP modes in the cavity shifts due to change of the effective index of the mode depending on the temperature. We assume the effective index change in the cavity is temperature dependent indices of the materials with

$$\Delta n_{eff}(T_{avg}) = \int P_{norm}(x, y) \Delta n(x, y, T(x, y)) dx dy \quad (4.3)$$

where Δn_{eff} is the change in the effective index at the average temperature, T_{avg} . $\Delta n(x, y, T(x, y))$ is the index change of the material at position x, y and temperature $T(x, y)$. $P_{norm}(x, y)$ is the normalized optical power and serves as a weighting function. The relationship between the effective index and the temperature is;

$$\Delta n_{eff}(T_{avg}) = \alpha \Delta T_{avg} \quad (4.4)$$

therefore,

$$\Delta T_{avg} = \frac{1}{\alpha} \int P_{norm}(x, y) \Delta n(x, y, T(x, y)) dx dy.$$

we now assume that the temperature dependent shift constant α for the effective index is also valid for temperature dependence of the material indices;

$$\Delta n(T(x, y)) = \alpha \Delta T(x, y) \quad (4.5)$$

This approximation does not affect the results much, because most of the optical power is confined in the active region, and the changes in the index is so small that it does not change the mode energy distribution significantly. Therefore;

$$\Delta T_{avg} = \int P_{norm}(x, y) \Delta T(x, y) dx dy.$$

This formula describes the relationship between the measured average temperature from the spectrum and the temperature distribution at the cross-section of the cavity.

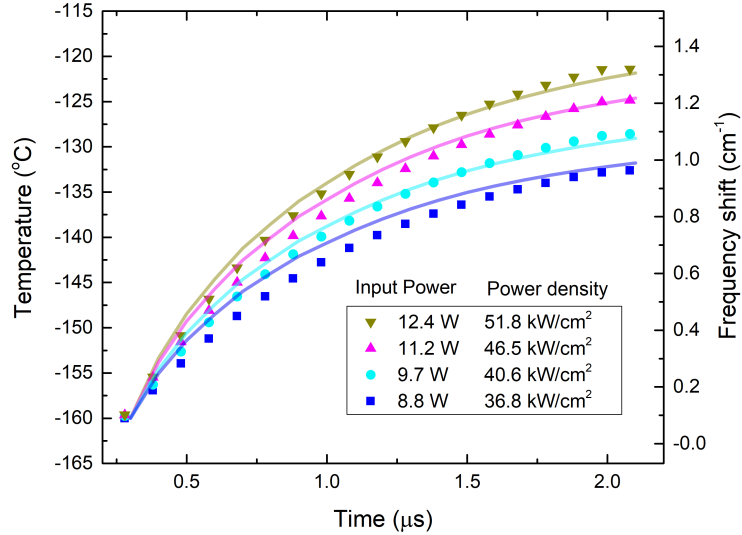


Figure 4.19: Simulated and measured time resolved cavity temperatures at various electrical input powers.

To calculate the power distribution, we used the optical mode intensity of the cavity calculated with Comsol Multiphysics. Calculation of the optical modes is explained in section 2.2. From the calculated mode electric field we calculate the normalized power using the formula;

$$P(x, y) = \frac{E^2(x, y)}{\int E^2(x, y) dx dy}. \quad (4.6)$$

By defining the thermal conductivity of the active region as a fitting parameter, we conducted a combined optical and thermal simulation of the laser cavity. We calculated the optical mode power profile $P(x, y)$ of the fundamental TM mode of the cavity. We defined the heat source with powers shown in the inset of Fig. 4.19 on the active region, and calculated the time-dependent temperature rises. An objective function was defined as the difference between the experimental data (shown with dots in Fig. 4.19) and the calculated temperatures (shown with solid lines);

$$f = \sum_{P_{in}, t} T_{exp}(t, P_{in}) - T_{sim}(t, P_{in}). \quad (4.7)$$

Thermal conductivity of the active region was optimized to minimize the objective function. Best fit was obtained for thermal conductivity, $k_{active} = 2.1 \pm 0.1$. Curves in fig. 4.19 are the Temperature using for this value.

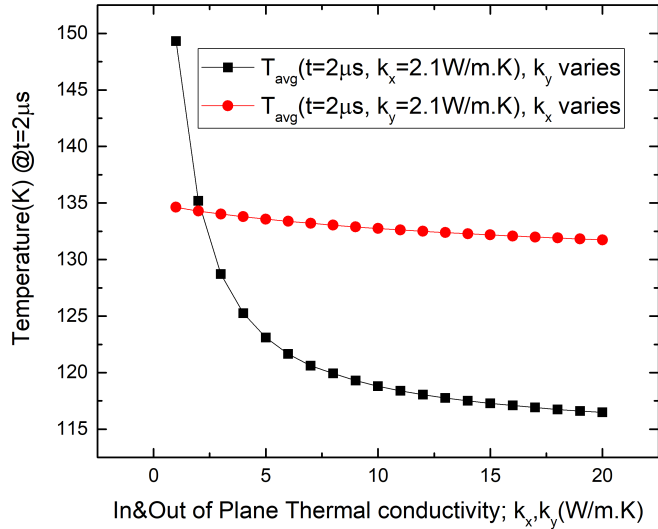


Figure 4.20: Average temperature as a function of in plane (k_x) and out of plane (k_y) thermal conductivities .

However, active region thermal conductivity of QCLs are known to be highly anisotropic [35, 31, 30]. To investigate the effect of anisotropy on the measured temperatures, we defined in plane (k_x) and out of plane (k_y) thermal conductivities of the active region independently and calculated T_{avg} at $2 \mu s$. Fig 4.20 shows the T_{avg} as a function of k_y when $k_x = 2.1$ (black curve) and as a function of k_x

when $k_y = 2.1$ (red curve). Temperatures show much stronger dependence on k_y around 2.1 W/m.K. This indicated that calculated "effective" thermal conductivity k_{active} value is closer to out of plane thermal conductivity. Indeed, when we fixed k_x to a value between 1-10 W/m.K, and fitted k_y , it converged to about 2.1 W/m.K, independent of the value of k_x . We have been able to distinguish in-plane and out-of-plane thermal conductivities and have shown that out-of plane thermal conductivity dominates the temperature rise. This is to be expected due to Kapitza resistance due to many layers limiting the heat flow.

Chapter 5

Optical Loss Management in Long-Wave QCLs

Optical power is one of the most demanded quantities for a QCL. Cavity loss and gain are the ultimate factors that determine the output power. The material gain of a QCL is generally much less than other semiconductor lasers, such as quantum well laser diodes. The typical range of modal optical gain for a QCL is 10-30 cm^{-1} , while the gain of a quantum well of a laser diode is in the range of 100-1000 cm^{-1} [85], although modal gains are within the same range. Overlap of the optical modes within the active region of a QCL is larger than quantum well lasers. In addition, due to the longer wavelengths, free carrier absorption loss is higher and material loss of commonly used passivation materials such as Si_3N_4 and SiO_2 could be higher in the long wavelength regime. For these reasons, loss reduction is critical for increasing the output powers.

Main sources of loss in a QCL cavity are;

1. Dielectric loss due to passivation material,
2. Plasmonic loss due to the contact metals,
3. Free carrier absorption due to doping in the cladding and active region,

4. Scattering losses due to the roughness of the cavity walls.

In this chapter, we will discuss the contribution of these in the net loss of the modes in the cavity.

5.1 Measurement of loss

There are many techniques in the literature for loss characterization of semiconductor lasers. Hakki-Paoli method [86] makes use of the subthreshold electroluminescence spectrum to characterize gain in the cavity. It involves analysis of local minima and maxima of the Fabry-Perot fringes in the electroluminescence data. This method works well for moderately high Q-factor cavities, but as the finesse of the cavity increases, minima of the fringes approaches to zero, and fringe contrast does not increase.

For high Q-factor cavities, a generalized version of the technique based on Fourier analysis of the electroluminescence spectrum could be used to characterize cavity loss-gain [87, 88]. However, due to fast non-radiative transitions below the threshold, intersubband electroluminescence of QCLs are generally weak. The intensity of the electroluminescence is voltage-dependent, which means below the threshold, the gain spectrum may differ substantially from the gain-loss during lasing[89]. Other approaches rely on current - optical power dependence. It is possible to calculate the cavity loss using the relationship between the threshold current and cavity length [90], or slope efficiency and cavity length [91]. At the threshold current density, gain and loss are equal, and;

$$gJ_{th} = \frac{\alpha_m + \alpha_w}{\Gamma} = \frac{\alpha_{tot}}{\Gamma} \quad (5.1)$$

and;

$$J_{th} = \frac{\alpha_w + \alpha_m}{g\Gamma} = \frac{\alpha_w}{g\Gamma} - \frac{\ln(\sqrt{R_1 R_2})}{g\Gamma} \frac{1}{L} \quad (5.2)$$

where $\alpha_m = \ln(\sqrt{R_1 R_2})/L$ is the mirror loss, α_w is the cavity loss, g is the gain

coefficient, Γ is the modal gain coefficient, R_1 and R_2 are the mirror reflectivities and L is the cavity length. Relationship between the cavity length and the differential quantum efficiency η_d is;

$$\frac{1}{\eta_d} = \frac{\alpha_w}{\eta_i \ln(1/\sqrt{R_1 R_2})} L + \frac{1}{\eta_i} \quad (5.3)$$

where η_i is the differential quantum efficiency and η_i is the injection efficiency.

$$\eta_d = \frac{dP}{dI} \frac{\lambda}{1.24 \mu\text{m}/\text{eV}} \quad (5.4)$$

dP/dI is the slope efficiency with units of Watt/Ampere. λ is the wavelength in free space in microns. To characterize the loss in our lasers, we used the cavity length-differential quantum efficiency relationship shown above. R_1 and R_2 are equal and $\approx 26\%$.

5.2 Sources of loss in QCLs

5.2.1 Dielectric loss

Almost all disrupted semiconductor layers need to be protected from outside elements such as humidity and contamination. Further, electrical isolation is needed. The passivation layer on a QCL cavity acts as an electrical insulator and affects both optical and thermal properties of the cavity since the passivation reaches down to the active layer. However, dielectric passivation materials can also absorb light and cause optical loss. Fig. 5.1 and 5.2 shows the extinction coefficients of Si_3N_4 , AlN and HfO_2 as a function of wavelength. It is clearly seen that nonzero extinction coefficient at $9.17 \mu\text{m}$ will result in optical loss due to passivation. Although Si_3N_4 is a common material for QCL passivation, its absorption coefficient at $9.5 \mu\text{m}$ is still too high and alternative low-loss materials may be needed. SrF_2 and AlN are good candidates for this application. SrF_2 has a low thermal conductivity but very low loss, AlN has a high thermal conductivity but moderate loss. Si_3N_4 has a moderate thermal conductivity but high loss, but it is easily available and easy to deposit and etch.

These are the reasons of why investigation of alternative passivation materials is helpful in characterization of loss mechanisms of the laser.

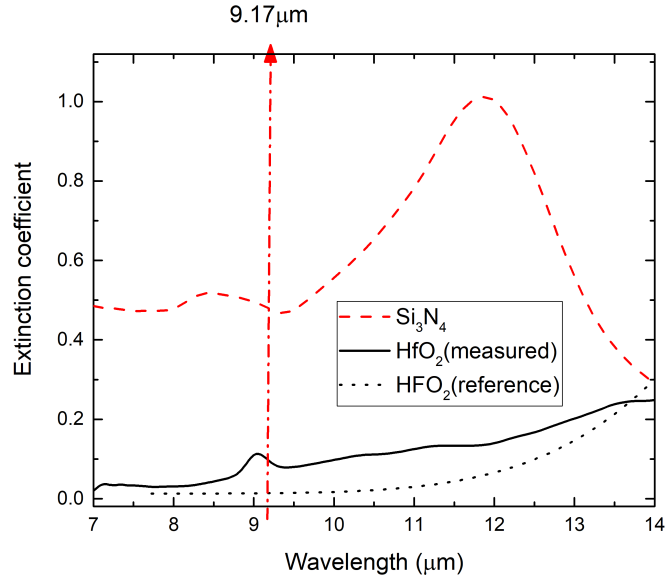


Figure 5.1: Extinction coefficient of Si₃N₄ and HfO₂

We have started to investigate SrF₂ and AlN as passivation to see their effect on the optical power. We purchased an AlN sputtering target to use in passivation of our lasers and started to fabricate lasers with SrF₂ using thermal evaporation. In all our trials so far, SrF₂ has been problematic and caused electrical short-circuiting both during electrical measurements and gold electroplating. It may be very porous for proper electrical isolation or leaks current due to its ionic structure or it may crack due to the high mismatch between its thermal expansion coefficient and that of the laser. Fig 5.2 shows the absorbance of AlN films at various RF sputtering powers and target temperatures. At 9-12 μm regime, the absorbance is strongly dependent on growth parameters, for this reason, extensive optimization studies may be needed to effectively use as a passivation material.

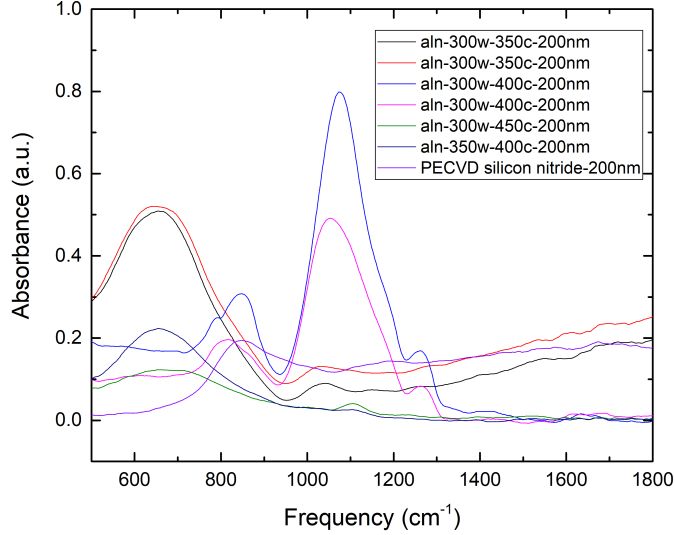


Figure 5.2: Absorbance of AlN thin films compared to and Si_3N_4

5.2.2 Plasmonic loss

Plasmonic loss is due to the coupling of the optical field to the free electrons of the metal contacts. Typically, the extension of the electric field of a mode into the surrounding metal leads to the formation of plasmon polaritons in the metal which later dissipates as heat by scattering from phonons. Metallization related loss is mainly determined by the tail of the optical mode (evanescent wave) reaching to the metal. Metallization at the top of the waveguide does not cause significant loss, since the optical mode is strongly confined by the active region and the surrounding waveguide decaying into the thick cladding, evanescently. In contrast with vertical confinement, lateral confinement has no index contrast until the mode decays into the surrounding sidewall passivation. Therefore, the primary parameter determining the plasmonic loss is the thickness of the intervening dielectric layer. Using the Comsol Wave Optics Module, we modeled the composite semiconductor, dielectric and metal interface and calculated the optical loss as a function of dielectric thickness. As shown in Fig. 5.3, plasmonic loss increases exponentially as the dielectric thickness decrease. For thick dielectrics, loss converges to a constant which is determined by the properties of

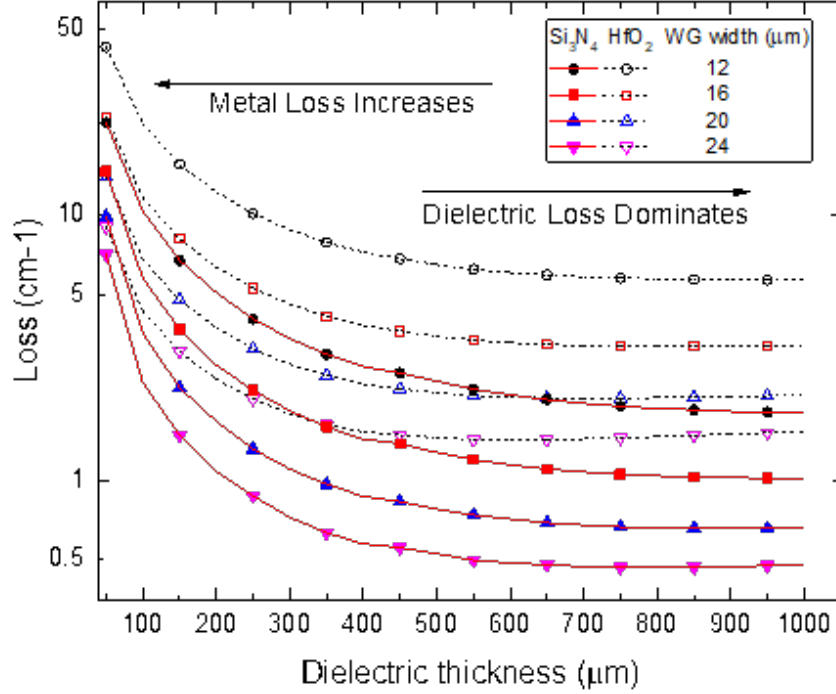


Figure 5.3: Loss of the fundamental TM mode of waveguides with varied width, as a function of dielectric thickness. © 2018 IEEE.

the dielectric.

Above 500 nm, change in loss is less than 5%. Considering that the thicker dielectric would deteriorate the thermal performance of the laser and is prone to cracking, we determine 500 nm as the optimal dielectric thickness to minimize the plasmonic loss.

5.2.3 Free carrier absorption

Free electron absorption occurs due to the presence of free electrons in the active region or cladding. In a QCL cavity three different types of modes may occur: Volume modes; are due to confinement of the light by total reflection from the

claddings, surface modes are due to coupling of the light with the surface plasmon polaritons on the interfaces, and Langmuir modes are due to plasma waves confined by total reflection from claddings [92].

Surface modes are relevant to laser operation if the waveguide designed with the metal contact or a highly doped layer close to the active region [93].

Langmuir modes are due to volume plasma waves of free electrons in the cavity. QCL injection region plasma resonance frequency of the mid-wave and long-wave QCLs are about a few THz [92]. Since the operating frequency is much higher than the resonance frequency, free carrier absorption is due to active region doping is low, and the resulting loss is in the order of 10^{-2}cm^{-1} [92].

5.3 Low loss waveguides

Dielectric loss of the conventional materials (Si_3N_4 or SiO_2) is a significant factor in reducing the efficiency of long-wavelength QCLs. For this reason, we compared the optical loss of the Si_3N_4 passivated and HfO_2 passivated lasers. To measure the optical loss using the relationship between the cavity length and differential quantum efficiency shown in equation 5.3, we measured the optical power of lasers with various length as a function of current.

Fig. 5.4 shows the optical power measured from a single facet of QCLs with 1.8, 2.5 and 3.8 mm cavity length and 12, 16, 20 and 24 μm ridge widths. Optical power was measured with an MCT photodetector and an integrating sphere placed in front of the dewar as shown in Fig. 3.20. Integrating sphere optical power was calibrated using a thermopile detector. Note that the specified ridge widths are at the top of the waveguide, and due to wet etched wall profiles, the active region is approximately $4\mu\text{m}$ wider than these. For all three cavity lengths, we observe increased current threshold with increasing ridge width and a linear increase after the threshold current. From the slope of the linear fits on the linear region of the current-power data, we calculated the slope efficiency for each laser.

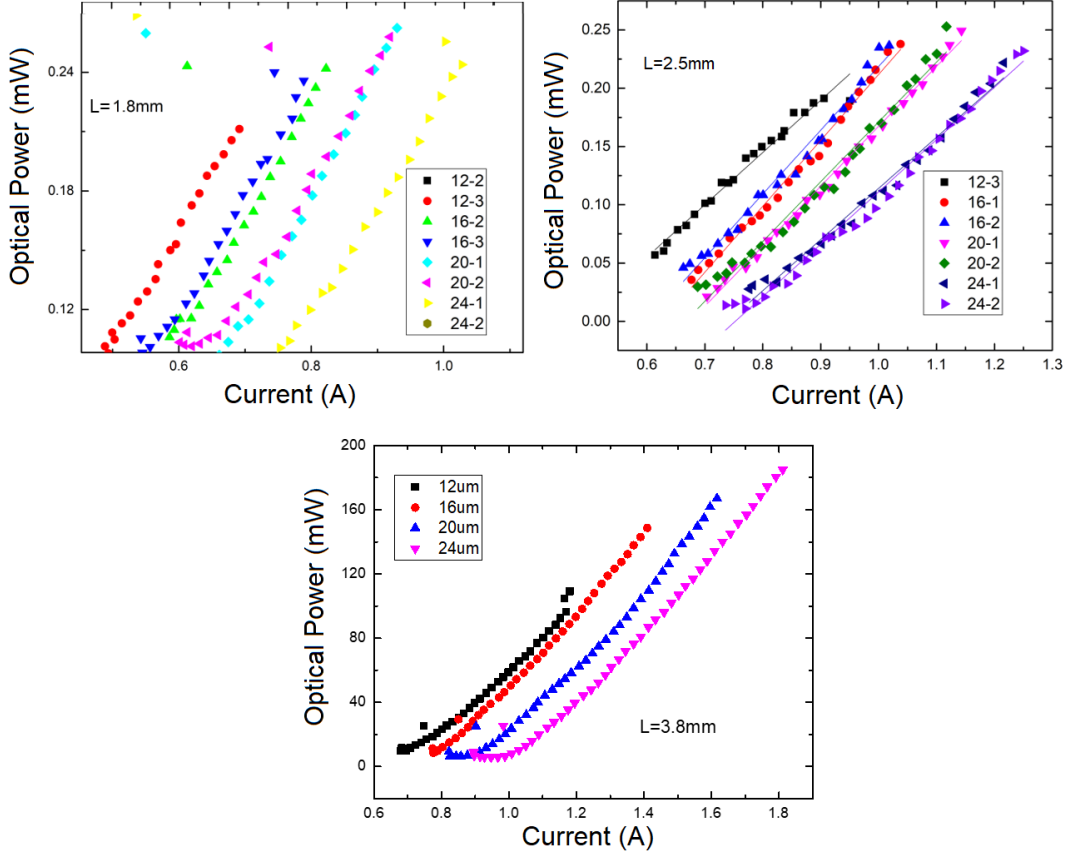


Figure 5.4: Current-power characteristics of HfO_2 passivated QCLs with 1.8, 2.5 and 3.8mm cavity length and various thicknesses.

Fig. 5.5 shows the inverse of slope efficiencies as a function of cavity length for both HfO_2 and Si_3N_4 passivated lasers. The difference between the slope efficiency of two passivations is clearly observed. Slope efficiencies have increased about two-fold. Green diamond symbols indicate the average data of all ridge widths for each cavity length. Two green lines show the linear fits to the average data of HfO_2 and Si_3N_4 passivated lasers. From these linear fits we calculated the loss of HfO_2 passivation as $6 \pm 0.5 \text{ cm}^{-1}$ and Si_3N_4 passivation as $11.5 \pm 1 \text{ cm}^{-1}$. This difference clearly shows the reduction of loss in HfO_2 passivation.

As a side note, the reason for using the average slope efficiencies for loss calculation is the error sensitivity of equation 5.3. To calculate α_w , we define a fit function $f(L) = a \cdot L + b$, therefore $\alpha_w \propto a/b$. Therefore the standard deviation

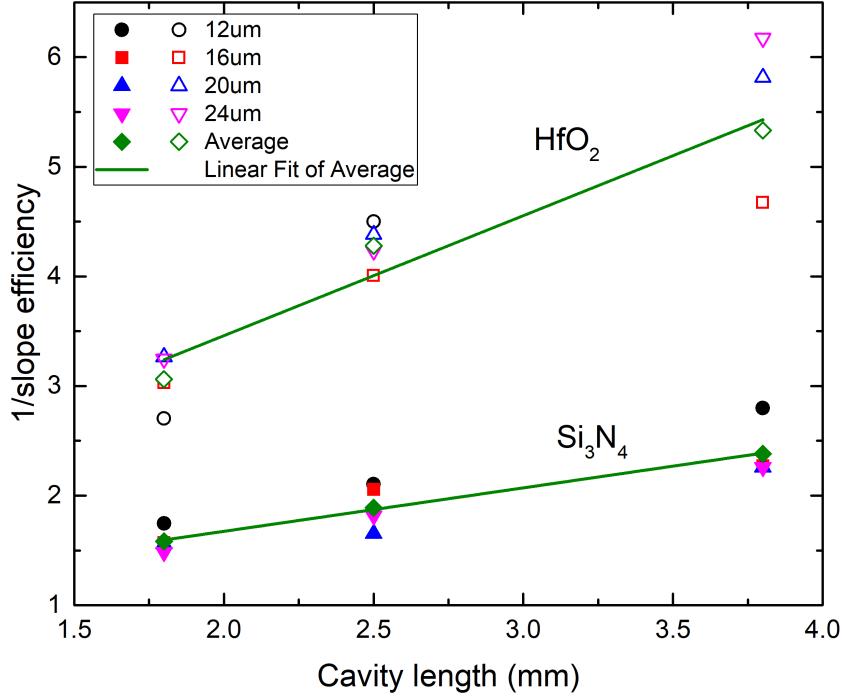


Figure 5.5: Inverse of slope efficiency as a function of cavity length. © 2018 IEEE.

of loss is;

$$\sigma_{\alpha_w} = |\alpha_w| \sqrt{\frac{\sigma_a}{a} + \frac{\sigma_b}{b} - 2\frac{\sigma_{ab}}{a \cdot b}} \quad (5.5)$$

where σ_a and σ_b are the standard deviation of slope and the intercept, respectively and σ_{ab} is their covariance. Therefore, error in loss increases with both error in slope and intercept. Error in intercept is particularly high.

Fig. 5.6 shows the lasing threshold current density of the same lasers in Fig. 5.5 as a function of cavity width. As a consequence of higher loss, the threshold current of Si₃N₄ passivated lasers have up to two times higher threshold current compared to HfO₂ passivated ones. In general, lasers with narrower ridge widths have higher current density. This is probably the result of the higher overlap of the optical mode with the dielectric. Width dependency of the threshold current density is also more prominent for the Si₃N₄ lasers, which also supports that this

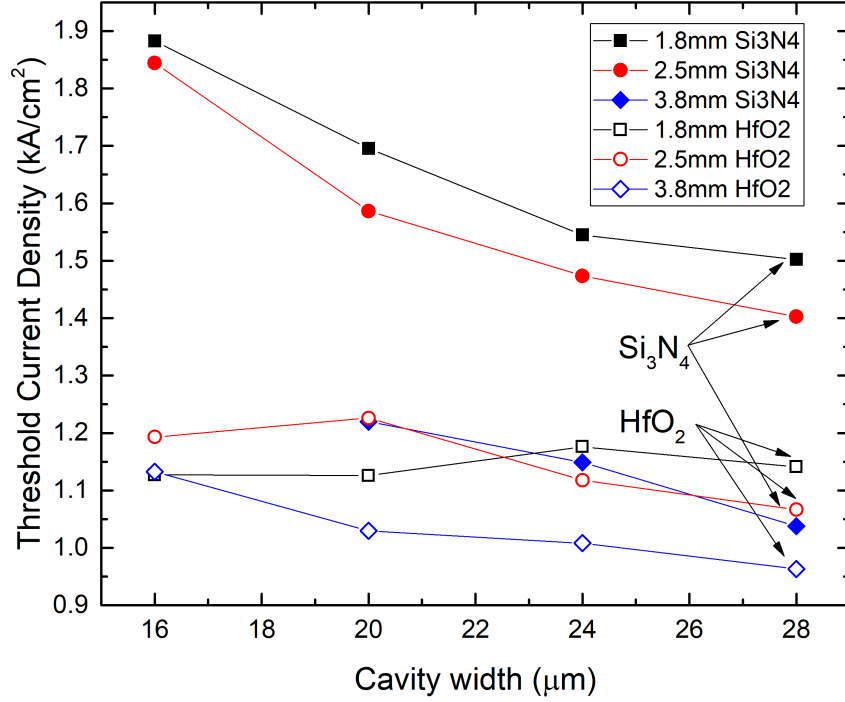


Figure 5.6: Lasing threshold current density as a function of cavity width for Si_3N_4 and HfO_2 passivated QCLs. © 2018 IEEE.

dependence is due to dielectric loss. As expected, this loss difference also affects the maximum output powers. For HfO_2 passivated lasers, we measured optical power up to ≈ 250 mW per facet. For Si_3N_4 passivated ones the maximum power obtained was 50 mW for one facet.

Bibliography

- [1] Nextnano website: nextnano.de.
- [2] L. Esaki and R. Tsu, "Superlattice and negative differential conductivity in semiconductors," *IBM Journal of Research and Development*, vol. 14, pp. 61–65, Jan 1970.
- [3] R. Kazarinov and R. Suris, "Possible amplification of electromagnetic waves in a semiconductor with a superlattice," vol. 5, pp. 707–709, 10 1971.
- [4] J. Faist, F. Capasso, D. L. Sivco, C. Sirtori, A. L. Hutchinson, and A. Y. Cho, "Quantum cascade laser," *Science*, vol. 264, no. 5158, pp. 553–556, 1994.
- [5] J. G. Ruch and W. Fawcett, "Temperature dependence of the transport properties of gallium arsenide determined by a Monte Carlo method," *Journal of Applied Physics*, vol. 41, pp. 3843–3849, aug 1970.
- [6] A. Andronov, V. Flyagin, A. Gaponov, A. Gol'denberg, M. Petelin, V. Usov, and V. Yulpatov, "The gyrotron: High-power source of millimetre and sub-millimetre waves," *Infrared Physics*, vol. 18, pp. 385–393, dec 1978.
- [7] J. Faist, "Intersubband optoelectronics," September 2009.
- [8] Q. J. Wang, C. Pflügl, L. Diehl, F. Capasso, T. Edamura, S. Furuta, M. Yamanishi, and H. Kan, "High performance quantum cascade lasers based on three-phonon-resonance design," *Applied Physics Letters*, vol. 94, p. 011103, jan 2009.

- [9] A. Wittmann, A. Hugi, E. Gini, N. Hoyler, and J. Faist, “Heterogeneous high-performance quantum-cascade laser sources for broad-band tuning,” *IEEE Journal of Quantum Electronics*, vol. 44, pp. 1083–1088, nov 2008.
- [10] J. R. Freeman, A. Brewer, J. Madeo, P. Cavalie, S. S. Dhillon, J. Tignon, H. E. Beere, and D. A. Ritchie, “Heterogeneous THz quantum cascade lasers: Broadband operation,” in *2011 International Conference on Infrared, Millimeter, and Terahertz Waves*, IEEE, oct 2011.
- [11] M. Ravaro, P. Gellie, G. Santarelli, C. Manquest, P. Filloux, C. Sirtori, J. Lampin, G. Ferrari, S. P. Khanna, E. H. Linfield, H. E. Beere, D. A. Ritchie, and S. Barbieri, “Stabilization and mode locking of terahertz quantum cascade lasers,” *IEEE Journal of Selected Topics in Quantum Electronics*, vol. 19, pp. 8501011–8501011, jan 2013.
- [12] C. Sirtori, S. Barbieri, and R. Colombelli, “Wave engineering with THz quantum cascade lasers,” *Nature Photonics*, vol. 7, pp. 691–701, sep 2013.
- [13] T. S. Mansuripur, S. Menzel, R. Blanchard, L. Diehl, C. Pflügl, Y. Huang, J.-H. Ryou, R. D. Dupuis, M. Loncar, and F. Capasso, “Widely tunable mid-infrared quantum cascade lasers using sampled grating reflectors,” *Optics Express*, vol. 20, p. 23339, sep 2012.
- [14] Q. Qin, J. L. Reno, and Q. Hu, “MEMS-based tunable terahertz wire-laser over 330 GHz,” *Optics Letters*, vol. 36, p. 692, feb 2011.
- [15] H. Page, P. Collot, A. de Rossi, V. Ortiz, and C. Sirtori, “High reflectivity metallic mirror coatings for mid-infrared ($\lambda \approx 9 \mu\text{m}$) unipolar semiconductor lasers,” *Semiconductor Science and Technology*, vol. 17, no. 12, p. 1312, 2002.
- [16] C. Bayo, *Theory of elasticity and electric polarization effects in the group-III nitrides*. PhD thesis, University College Cork, 2013.
- [17] J. Devenson, O. Cathabard, R. Teissier, and A. N. Baranov, “InAs/AlSb quantum cascade lasers emitting at 2.75-2.97 μm ,” *Applied Physics Letters*, vol. 91, p. 251102, dec 2007.

- [18] O. Cathabard, R. Teissier, J. Devenson, J. C. Moreno, and A. N. Baranov, “Quantum cascade lasers emitting near 2.6 μm ,” *Applied Physics Letters*, vol. 96, p. 141110, apr 2010.
- [19] S. Y. Zhang, D. G. Revin, J. W. Cockburn, K. Kennedy, A. B. Krysa, and M. Hopkinson, “ $\lambda \approx 1 \mu\text{m}$ room temperature ingaas/alassb/inp quantum cascade lasers,” *Applied Physics Letters*, vol. 94, p. 031106, jan 2009.
- [20] D. G. Revin, J. W. Cockburn, M. J. Steer, R. J. Airey, M. Hopkinson, A. B. Krysa, L. R. Wilson, and S. Menzel, “Improved performance of in_{0.6}ga_{0.4}as/alas_{0.67}sb_{0.33}/inp quantum cascade lasers by introduction of AlAs barriers in the active regions,” *Applied Physics Letters*, vol. 91, p. 051123, jul 2007.
- [21] Y. Bai, N. Bandyopadhyay, S. Tsao, E. Selcuk, S. Slivken, and M. Razeghi, “Highly temperature insensitive quantum cascade lasers,” *Applied Physics Letters*, vol. 97, p. 251104, dec 2010.
- [22] J. S. Yu, S. Slivken, S. R. Darvish, A. Evans, B. Gokden, and M. Razeghi, “High-power, room-temperature, and continuous-wave operation of distributed-feedback quantum-cascade lasers at $\lambda \sim 4.8 \mu\text{m}$,” *Applied Physics Letters*, vol. 87, p. 041104, jul 2005.
- [23] J. Faist, D. Hofstetter, M. Beck, T. Aellen, M. Rochat, and S. Blaser, “Bound-to-continuum and two-phonon resonance, quantum-cascade lasers for high duty cycle, high-temperature operation,” *IEEE Journal of Quantum Electronics*, vol. 38, pp. 533–546, jun 2002.
- [24] J. Mandon, M. Hogman, P. J. F. M. Merkus, J. van Amsterdam, F. J. M. Harren, and S. M. Cristescu, “Exhaled nitric oxide monitoring by quantum cascade laser: comparison with chemiluminescent and electrochemical sensors,” *Journal of Biomedical Optics*, vol. 17, no. 1, p. 017003, 2012.
- [25] C. Jirauschek and T. Kubis, “Modeling techniques for quantum cascade lasers,” *Applied Physics Reviews*, vol. 1, p. 011307, mar 2014.

- [26] D.-S. Jiang, Z.-P. Wang, C. Abraham, K. Syassen, Y. Zhang, and K. Ploog, “A resonant raman study on phonons in GaInAs/AlInAs multiple quantum wells,” *Journal of Physics and Chemistry of Solids*, vol. 56, pp. 397–401, mar 1995.
- [27] S. Nojima and H. Asahi, “Refractive index of InGaAs/InAlAs multi-quantum-well layers grown by molecular-beam epitaxy,” *Journal of Applied Physics*, vol. 63, pp. 479–483, jan 1988.
- [28] A. Li, J. Chen, Q. Yang, Y. Zhang, and C. Lin, “The effect of dispersion of the refractive index on the performance of mid-infrared quantum cascade lasers,” *Journal of Crystal Growth*, vol. 227-228, pp. 313–318, jul 2001.
- [29] R. C. Jayasinghe, Y. F. Lao, A. G. U. Perera, M. Hammar, C. F. Cao, and H. Z. Wu, “Plasma frequency and dielectric function dependence on doping and temperature for p-type indium phosphide epitaxial films,” *Journal of Physics: Condensed Matter*, vol. 24, p. 435803, oct 2012.
- [30] M. S. Vitiello and G. Scamarcio, “Anisotropic heat propagation velocity in quantum cascade lasers,” *Applied Physics Letters*, vol. 96, p. 101101, mar 2010.
- [31] V. Spagnolo, M. Vitiello, C. D. Franco, and G. Scamarcio, “Thermal modelling of quantum cascade lasers,” *Acta Physica Polonica A*, vol. 116, pp. 451–454, oct 2009.
- [32] J. Faist, F. Capasso, C. Sirtori, D. Sivco, A. Hutchinson, and A. Cho, “Room temperature mid-infrared quantum cascade lasers,” *Electronics Letters*, vol. 32, no. 6, p. 560, 1996.
- [33] Y. Bai, N. Bandyopadhyay, S. Tsao, S. Slivken, and M. Razeghi, “Room temperature quantum cascade lasers with 27% wall plug efficiency,” *Applied Physics Letters*, vol. 98, p. 181102, may 2011.
- [34] M. Razeghi, S. Slivken, Y. Bai, B. Gokden, and S. R. Darvish, “High power quantum cascade lasers,” *New Journal of Physics*, vol. 11, p. 125017, dec 2009.

- [35] M. S. Vitiello, G. Scamarcio, and V. Spagnolo, “Temperature dependence of thermal conductivity and boundary resistance in THz quantum cascade lasers,” *IEEE Journal of Selected Topics in Quantum Electronics*, vol. 14, no. 2, pp. 431–435, 2008.
- [36] M. A. Belkin and F. Capasso, “New frontiers in quantum cascade lasers: high performance room temperature terahertz sources,” *Physica Scripta*, vol. 90, p. 118002, oct 2015.
- [37] V. Spagnolo, G. Scamarcio, D. Marano, H. Page, and C. Sirtori, “Thermoelastic stress in GaAs/AlGaAs quantum cascade lasers,” *Applied Physics Letters*, vol. 82, pp. 4639–4641, jun 2003.
- [38] Y. Sin, N. Presser, M. Brodie, Z. Lingley, S. Moss, J. Kirch, C. Chang, C. Boyle, L. Mawst, D. Botez, D. Lindberg, and T. Earles, “Catastrophic degradation in quantum cascade lasers emitting at 8.4 μm ,” in *2014 IEEE Photonics Society Summer Topical Meeting Series*, IEEE, jul 2014.
- [39] Q. Zhang, F.-Q. Liu, W. Zhang, Q. Lu, L. Wang, L. Li, and Z. Wang, “Thermal induced facet destructive feature of quantum cascade lasers,” *Applied Physics Letters*, vol. 96, p. 141117, apr 2010.
- [40] V. Palanovski, *Simulation of Heterojunction Bipolar Transistors*. Ph.D. thesis, Technische Universität Wien, 2000.
- [41] U. Piesbergen *Z. Naturforschung*, vol. 18a, no. 2, pp. 141–147, 1963.
- [42] A. N.N.Sirota, V.V.Novikov *Doklady Akademii Nauk SSSR*, vol. 263, no. 1, pp. 96–100, 1982.
- [43] S. Adachi, *Properties of Aluminium Gallium Arsenide*, *The Institution of Electrical Engineers*. The Institution of Engineering and Technology, 1993.
- [44] F. Baiutti, G. Christiani, and G. Logvenov, “Towards precise defect control in layered oxide structures by using oxide molecular beam epitaxy,” *Beilstein Journal of Nanotechnology*, vol. 5, pp. 596–602, may 2014.

- [45] F.-Q. Liu, L. Li, L. Wang, J. Liu, W. Zhang, Q. Zhang, W. Liu, Q. Lu, and Z. Wang, “Solid source MBE growth of quantum cascade lasers,” *Applied Physics A*, vol. 97, pp. 527–532, sep 2009.
- [46] IQE website: <http://www.iqep.com>.
- [47] J. S. Roberts, R. P. Green, L. R. Wilson, E. A. Zibik, D. G. Revin, J. W. Cockburn, and R. J. Airey, “Quantum cascade lasers grown by metalorganic vapor phase epitaxy,” *Applied Physics Letters*, vol. 82, pp. 4221–4223, jun 2003.
- [48] A. A. Marmalyuk, A. A. Padalitsa, M. A. Ladugin, P. V. Gorlachuk, I. V. Yarotskaya, A. Y. Andreev, T. A. Bagaev, A. V. Lobintsov, Y. V. Kurnyavko, S. M. Sapozhnikov, A. I. Danilov, K. Y. Telegin, V. A. Simakov, I. I. Zaslavitskii, and S. S. Zarubin, “Metalorganic vapour phase epitaxy of GaAs/AlGaAs nanoheterostructures for a quantum cascade laser,” *Inorganic Materials*, vol. 53, pp. 891–895, aug 2017.
- [49] C. Wang, B. Schwarz, D. Siriani, M. Connors, L. Missaggia, D. Calawa, D. McNulty, A. Akey, M. Zheng, J. Donnelly, T. Mansuripur, and F. Capasso, “Sensitivity of heterointerfaces on emission wavelength of quantum cascade lasers,” *Journal of Crystal Growth*, vol. 464, pp. 215–220, apr 2017.
- [50] Y. Huang, J.-H. Ryou, R. D. Dupuis, C. Pflügl, F. Capasso, K. Sun, A. M. Fischer, and F. A. Ponce, “Optimization of growth conditions for InGaAs/InAlAs/InP quantum cascade lasers by metalorganic chemical vapor deposition,” *Journal of Crystal Growth*, vol. 316, pp. 75–80, feb 2011.
- [51] A. B. Krysa, D. G. Revin, J. P. Commin, C. N. Atkins, K. Kennedy, Y. Qiu, T. Walther, and J. W. Cockburn, “Room-temperature GaAs/AlGaAs quantum cascade lasers grown by metal–organic vapor phase epitaxy,” *IEEE Photonics Technology Letters*, vol. 23, pp. 774–776, jun 2011.
- [52] K. Vijayraghavan, M. Jang, A. Jiang, X. Wang, M. Troccoli, and M. A. Belkin, “THz difference-frequency generation in MOVPE-grown quantum cascade lasers,” *IEEE Photonics Technology Letters*, vol. 26, pp. 391–394, feb 2014.

- [53] L. Sirigu, A. Rudra, E. Kapon, M. I. Amanti, G. Scalari, and J. Faist, “A terahertz quantum cascade laser grown by low-pressure metalorganic vapor phase epitaxy,” *Applied Physics Letters*, vol. 92, p. 181111, may 2008.
- [54] J. Fan, M. Belkin, M. Troccoli, S. Corzine, D. Bour, G. Höfler, and F. Capasso, “Double-metal waveguide $\simeq 19$ [micro sign]m quantum cascade lasers grown by metal organic vapour phase epitaxy,” *Electronics Letters*, vol. 43, no. 23, p. 1284, 2007.
- [55] Z. Liu, D. Wasserman, S. Howard, A. Höffman, C. Gmachl, X. Wang, T. Tanbun-Ek, L. Cheng, and F.-S. Choa, “Room-temperature continuous-wave quantum cascade lasers grown by MOCVD without lateral regrowth,” *IEEE Photonics Technology Letters*, vol. 18, pp. 1347–1349, jun 2006.
- [56] C. Pflügl, M. Austerer, W. Schrenk, S. Golka, G. Strasser, R. P. Green, L. R. Wilson, J. W. Cockburn, A. B. Krysa, and J. S. Roberts, “Single-mode surface-emitting quantum-cascade lasers,” *Applied Physics Letters*, vol. 86, p. 211102, may 2005.
- [57] M. Troccoli, S. Corzine, D. Bour, J. Zhu, O. Assayag, L. Diehl, B. Lee, G. Höfler, and F. Capasso, “Room temperature continuous-wave operation of quantum-cascade lasers grown by metal organic vapour phase epitaxy,” *Electronics Letters*, vol. 41, no. 19, p. 1059, 2005.
- [58] M. Troccoli, D. Bour, S. Corzine, G. Höfler, A. Tandon, D. Mars, D. J. Smith, L. Diehl, and F. Capasso, “Low-threshold continuous-wave operation of quantum-cascade lasers grown by metalorganic vapor phase epitaxy,” *Applied Physics Letters*, vol. 85, pp. 5842–5844, dec 2004.
- [59] R. P. Green, L. R. Wilson, E. A. Zibik, D. G. Revin, J. W. Cockburn, C. Pflügl, W. Schrenk, G. Strasser, A. B. Krysa, J. S. Roberts, C. M. Tey, and A. G. Cullis, “High-performance distributed feedback quantum cascade lasers grown by metalorganic vapor phase epitaxy,” *Applied Physics Letters*, vol. 85, pp. 5529–5531, dec 2004.

- [60] A. Krysa, J. Roberts, R. Green, L. Wilson, H. Page, M. Garcia, and J. Cockburn, “MOVPE-grown quantum cascade lasers operating at $\sim 9\mu\text{m}$ wavelength,” *Journal of Crystal Growth*, vol. 272, pp. 682–685, dec 2004.
- [61] D. Bour, M. Troccoli, F. Capasso, S. Corzine, A. Tandon, D. Mars, and G. Höfler, “Metalorganic vapor-phase epitaxy of room-temperature, low-threshold InGaAs/AlInAs quantum cascade lasers,” *Journal of Crystal Growth*, vol. 272, pp. 526–530, dec 2004.
- [62] Y. Inoue, H. Nagasawa, N. Sone, K. Ishino, A. Ishida, H. Fujiyasu, J. Kim, H. Makino, T. Yao, S. Sakakibara, and M. Kuwabara, “Fabrication and characterization of short period AlN-GaN quantum cascade laser structures,” *Journal of Crystal Growth*, vol. 265, pp. 65–70, apr 2004.
- [63] J. Kubacka-Traczyk, I. Sankows, K. Kosiel, and M. Bugajski, “High-resolution x-ray characterization of mid-IR QCL structures,” in *2009 International Workshop Terahertz and Mid Infrared Radiation: Basic Research and Practical Applications*, IEEE, nov 2009.
- [64] A. S. Kurochkin, I. I. Novikov, L. Y. Karachinsky, D. V. Denisov, A. G. Gladyshev, G. A. Gusev, A. N. Sofronov, A. A. Usikova, Y. M. Zadiranov, G. S. Sokolovsky, V. M. Ustinov, and A. Y. Egorov, “MBE growth and characterization of InAlAs/InGaAs $9\mu\text{m}$ range quantum cascade laser,” *Journal of Physics: Conference Series*, vol. 917, p. 052016, nov 2017.
- [65] V. V. Mamutin, V. M. Ustinov, N. D. Ilyinskaya, M. V. Baydakova, B. Y. Ber, and D. Y. Kasantsev, “Molecular-beam epitaxy growth and characterization of $5\text{-}\mu\text{m}$ quantum cascade laser,” *Journal of Physics: Conference Series*, vol. 291, p. 012008, apr 2011.
- [66] P. P. Michałowski, P. Gutowski, D. Pierścińska, K. Pierściński, M. Bugajski, and W. Strupiński, “Characterization of the superlattice region of a quantum cascade laser by secondary ion mass spectrometry,” *Nanoscale*, vol. 9, no. 44, pp. 17571–17575, 2017.
- [67] J. Faist, “Quantum cascade lasers,” p. 3, Oxford University Press, 2013.

- [68] S. Bouchoule, L. Vallier, G. Patriarche, T. Chevolleau, and C. Cardinaud, “Effect of Cl_2 - and HBr -based inductively coupled plasma etching on InP surface composition analyzed using in situ x-ray photoelectron spectroscopy,” *Journal of Vacuum Science & Technology A: Vacuum, Surfaces, and Films*, vol. 30, p. 031301, may 2012.
- [69] J. W. McNabb, “Anisotropic reactive ion etching of InP in methane/hydrogen based plasmas,” *Journal of Vacuum Science & Technology B: Microelectronics and Nanometer Structures*, vol. 9, p. 3535, nov 1991.
- [70] S. Chang-Zheng, Z. Jin-Bo, X. Bing, W. Jian, and L. Yi, “Vertical and smooth, etching of inp by $\text{Cl}_2/\text{CH}_4/\text{Ar}$ inductively coupled plasma at room temperature,” *Chinese Physics Letters*, vol. 20, no. 8, p. 1312, 2003.
- [71] N. I. Sorokin and B. P. Sobolev, “Nonstoichiometric fluorides—solid electrolytes for electrochemical devices: A review,” *Crystallography Reports*, vol. 52, pp. 842–863, sep 2007.
- [72] H. Page, P. Collot, A. de Rossi, V. Ortiz, and C. Sirtori, “High reflectivity metallic mirror coatings for mid-infrared ($\approx 9 \mu\text{m}$) unipolar semiconductor lasers,” *Semiconductor Science and Technology*, vol. 17, pp. 1312–1316, nov 2002.
- [73] Cirroid website: cirroid.com.
- [74] A.-C. Pliska, J. Mottin, N. Matuschek, and C. Bosshard, “Bonding Semiconductor Laser Chips : Substrate Material Figure of Merit and Die Attach Layer Influence,” in *THERMINIC 2005*, (Belgirate, Lago Maggiore, Italy), pp. 76–83, TIMA Editions, Sept. 2005. Submitted on behalf of EDA Publishing Association (<http://irevues.inist.fr/handle/2042/5920>).
- [75] G. Greitmann, H. Burkard, and J. Link, “- 25 june 2003-1-AuSn thin film solder layers for assembly of optoelectronic devices,” 2003.
- [76] L. Esaki and R. Tsu, “Superlattice and negative differential conductivity in semiconductors,” *IBM Journal of Research and Development*, vol. 14, pp. 61–65, jan 1970.

- [77] H. Liu and F. Capasso, *Intersubband Transitions in Quantum Wells: Physics and Device Applications, Volume 62 1st Edition*. Academic Press, 2000.
- [78] C. Sirtori, F. Capasso, J. Faist, A. Hutchinson, D. Sivco, and A. Cho, “Resonant tunneling in quantum cascade lasers,” *IEEE Journal of Quantum Electronics*, vol. 34, no. 9, pp. 1722–1729, 1998.
- [79] L. Esaki and L. L. Chang, “New transport phenomenon in a semiconductor “superlattice”,” *Physical Review Letters*, vol. 33, pp. 495–498, aug 1974.
- [80] D. Botez, J. D. Kirch, C. Boyle, K. M. Oresick, C. Sigler, H. Kim, B. B. Knipfer, J. H. Ryu, D. Lindberg, T. Earles, L. J. Mawst, and Y. V. Flores, “High-efficiency, high-power mid-infrared quantum cascade lasers [invited],” *Optical Materials Express*, vol. 8, p. 1378, apr 2018.
- [81] A. Gordon, C. Y. Wang, L. Diehl, F. X. Kärtner, A. Belyanin, D. Bour, S. Corzine, G. Höfler, H. C. Liu, H. Schneider, T. Maier, M. Troccoli, J. Faist, and F. Capasso, “Multimode regimes in quantum cascade lasers: From coherent instabilities to spatial hole burning,” *Physical Review A*, vol. 77, may 2008.
- [82] C. Y. Wang, L. Diehl, A. Gordon, C. Jirauschek, F. X. Kärtner, A. Belyanin, D. Bour, S. Corzine, G. Höfler, M. Troccoli, J. Faist, and F. Capasso, “Coherent instabilities in a semiconductor laser with fast gain recovery,” *Physical Review A*, vol. 75, mar 2007.
- [83] E. Diez, R. Gómez-Alcalá, F. Domínguez-Adame, A. Sánchez, and G. P. Berman, “Rabi oscillations in semiconductor superlattices,” *Physical Review B*, vol. 58, pp. 1146–1149, jul 1998.
- [84] D. G. Allen, T. W. Hargett, J. L. Reno, and M. C. Wanke, “Optical bistability from domain formation in terahertz quantum cascade lasers,” *IEEE Journal of Selected Topics in Quantum Electronics*, vol. 17, pp. 222–228, jan 2011.
- [85] “High power diode lasers, technology and applications,” p. 10, Springer-Verlag New York, 2007.

- [86] B. W. Hakki and T. L. Paoli, “Gain spectra in GaAs double-heterostructure injection lasers,” *Journal of Applied Physics*, vol. 46, pp. 1299–1306, mar 1975.
- [87] D. Hofstetter and R. Thornton, “Measurement of optical cavity properties in semiconductor lasers by fourier analysis of the emission spectrum,” *IEEE Journal of Quantum Electronics*, vol. 34, no. 10, pp. 1914–1923, 1998.
- [88] D. Hofstetter and J. Faist, “Measurement of semiconductor laser gain and dispersion curves utilizing fourier transforms of the emission spectra,” *IEEE Photonics Technology Letters*, vol. 11, pp. 1372–1374, nov 1999.
- [89] D. G. Revin, M. R. Soulby, J. W. Cockburn, Q. Yang, C. Manz, and J. Wagner, “Dispersive gain and loss in midinfrared quantum cascade laser,” *Applied Physics Letters*, vol. 92, p. 081110, feb 2008.
- [90] C. Sirtori, P. Kruck, S. Barbieri, H. Page, J. Nagle, M. Beck, J. Faist, and U. Oesterle, “Low-loss Al-free waveguides for unipolar semiconductor lasers,” *Applied Physics Letters*, vol. 75, pp. 3911–3913, dec 1999.
- [91] J. Piprek, P. Abraham, and J. Bowers, “Cavity length effects on internal loss and quantum efficiency of multi-quantum-well lasers,” *IEEE Journal of Selected Topics in Quantum Electronics*, vol. 5, no. 3, pp. 643–647, 1999.
- [92] A. Bogdanov and R. Suris, “Theoretical analysis of free carrier absorption in the cavity of a quantum cascade laser,” *physica status solidi (b)*, vol. 249, pp. 885–895, mar 2012.
- [93] C. Sirtori, J. Faist, F. Capasso, D. L. Sivco, A. L. Hutchinson, and A. Y. Cho, “Quantum cascade laser with plasmon-enhanced waveguide operating at 8.4 μm wavelength,” *Applied Physics Letters*, vol. 66, pp. 3242–3244, jun 1995.
- [94] A. Calvar, *Design, engineering and processing of QC Lasers for high frequency modulation*. PhD thesis, Université Paris Diderot - Paris 7, 2013.

Appendix A

Active region designs

A.1 InGaAs/AlInAs based InP949

This design is the only crystal that we could observe light emission. Design and the original wafer was obtained from Prof. Carlo Sirtori and grown by MOCVD. We later get it fabricated by MBE service of IQE. More details of this crystal and MOCVD growth parameters can be found in Dr. Calvar's thesis [94].

Material	Doping	Thickness (Å)
InGaAs** : Si	5E18	1000
InP: Si (5E18)	5E18	8500
InP: Si (5E16)	5E16	25000
InGaAs : Si		2000
InGaAs		29.0
AlInAs		27.0
InGaAs		29.0
AlInAs		27.0
InGaAs		31.0
AlInAs	3,3E+16	23.0
InGaAs	3,3E+16	31.0
AlInAs	3,3E+16	18.0
InGaAs	3,3E+16	33.0
AlInAs		16.0
InGaAs		38.0
AlInAs		18.0
InGaAs		42.0
AlInAs		22.0
InGaAs		44.0
AlInAs		12.0
InGaAs		51.0
AlInAs		9.0
InGaAs		55.0
AlInAs		9.0
InGaAs		58.0
AlInAs		9.0
InGaAs		20.0
AlInAs		40.0
InGaAs : Si	5E16	2000
InP: Si (5E16)	5E16	20000
InGaAs : Si	1E18	500.0
Buffer		
InP substrate	5E18	

Injection region

Active region 40x, Total thickness: 2764nm

Appendix B

Fabrication Lab Flow

1. Sample preparation & cleaving

- (a) Cleave a 12x12 mm wafer using a diamond scribe. To do this, put the sample on a few layers of cleanroom towels epi-down. Mark the point to be cut using the diamond pen and using a plastic tweezers, push the scribed point gently. This method cleave InP easily. GaAs requires more pressure, but cleaves cleanly.
- (b) Put the cleaved sample in acetone in a plastic beaker in the ultrasonic bath for 30 minutes at 60 °C. (Glass beakers should not be used and there should be enough water in the ultrasonic cleaner. Else the wafer may shatter.)
- (c) Take the sample from the beaker holding from the edges. Wash using isopropyl alcohol before the acetone on the sample evaporates. Put the sample on a cleanroom towel and force dry using nitrogen.
- (d) Examine the sampled under the microscope. Most of the grease/dirt should be removed at this point.
- (e) If still there are stains, one may use this recipe: prepare 1:1:10 HF:H₂O₂:H₂O solution in a plastic beaker. Also prepare deionized water for rinsing in another beaker. Put the sample in for 8 seconds in the solution and put it in the rinsing water immediately. Then dry it

with nitrogen. This recipe removes the stains effectively, however, we observed some remaining defects even after this step. We suspected that these defects were there before the crystal growth or deposited during the growth. We avoided these defects when aligning the mask for lithography. Below is an example of such defects.

2. Waveguide lithography

- (a) Put the cleaned sample on a hot plate at 110 °C for a minute. This step is needed to remove the adsorbed water vapor on the surface.
- (b) Put the sample on the spinner and coat the surface with HMDS. Wait for a minute. HMDS is recommended for adhesion of photoresist on SiO₂, however we observed it is very effective for both GaAs and InP wafers. If this step is skipped, photoresist may not adhere properly and lift-off at the etching step.
- (c) Run the spinner at 5200 rpm for 10 seconds to remove HMDS.
- (d) Coat the sample with AZ5214 photoresist. Be aware of any bubbles as they may cause defects. There should not be any photoresist under the chip, or it may cause it to break when aligning at the mask aligner. It is also good practice to filter the photoresist using a filtered syringe and wait for the resist to reach room temperature.
- (e) Run the spinner at 5200 rpm for 55 seconds.
- (f) Put the sample on the hot plate for 55 seconds at 110 °C.
- (g) We designed a square shaped mask for removal of the edge-beads of photoresist. However, the UV source of the mask aligner was not enough to remove the edges for even at 15 min exposure. For this stage an external UV source was used for 1 minute. Then the sample is developed .
- (h) Align the sample and the trench mask at the mask aligner at 3 mW 80 sec. It is important to align the mask with respect to the cleaved edges of the sample so that the waveguides are perpendicular to the cleaved edges. So we designed a special long line as a alignment marker on

the trench etch mask. Another thing to take into account is that there should be enough space between the edge of the sample and the edge of the mask (1mm should be adequate.) This is to cleave the edges of the wafer easily after the process.

- (i) Prepare the developer solution and the rinsing water. We used 3:8 AZ400K:water solution at this stage. Developing time is 45 sec.
- (j) Put the sample on hot plate for 2 min at 120C.
- (k) Measure the photoresist thickness with Dektak profilometer. This value will be needed at the etching step.

3. Trench etching

- (a) We used different methods to make waveguides for InP and GaAs based lasers.
 - i. For InP, use the 1:1:10 HBr:HNO₃:H₂O solution. This solution etches InP, InGaAs and AlInAs at the same rate. It should be aged for at least a week, and can be re-used. As a precaution, it should be kept in a fume hood.
 - ii. For GaAs, mix 150 g citric acid with 150 g deionized water. Stir in a magnetic stirrer for an hour at 80 °C, 200 rpm. Wait until it reached room temperature. Mix with 1:10 H₂O₂ just before using.
- (b)
 - i. We used a PTFE basket to etch InP sample (below). Put a magnetic bar in a glass beaker and insert the PTFE basket into the beaker. Add the etching solution and stir at 1000 rpm. This is to prevent formation of bubbles during etching.
 - ii. There is no need to use magnetic stirrer for GaAs process. A glass beaker may be used.
- (c) Etch for half the time required for estimated total etching time. Measure the etch rate using dektak and from this etch rate, estimate the remaining time and etch again. We measured etch rates as 2.3 μm/min for HBr:HNO₃ and 200 nm/min for the citric acid solution.
- (d) Remove the photoresist with acetone, IPA and blow dry.

- (e) Check for remaining photoresist under the microscope. Sometimes acetone can not remove all the resist due to too much hard-bake. These can be removed in warm acetone in ultrasonic bath.
 - (f) Measure the etch depth one last time.
- After this step we imaged the etched waveguides using SEM.

4. Insulator oxide coating and etching

- (a) We coated the samples with SiO_2 using PECVD. However, usually Si_3N_4 is used due to its high thermal conductivity and electrical breakdown voltage. We used these recipe: i. 180 sccm $\text{SiH}_4:\text{N}_2$ ii. 720 sccm N_2O iii. Substrate temperature: 250 °C iv. Pressure 1 mTorr v. Rf power: 14 W Deposition rate is 50 nm/dk. We coated 200 nm of film in 4 minutes.
- (b) Check the film under the microscope for defects and pinholes.
- (c) Put the sample on a hot plate at 110 °C for 1 min.
- (d) Put the sample on the spinner and coat it with HMDS wait for a minute and run the spinner at 5200 rpm for 10 sec.
- (e) Coat the sample with AZ 5214. For this step, we run the spinner 4000 rpm for 55 sec. This is for the film to coat the trenches evenly.
- (f) Put the sample on the mask aligner. Roughly align the window etching mask. Here is the method I use to align using the alignment markers.
 - i. Sample should be put on the holder so that one corner is at the center of the holder.
 - ii. Find the markers that are farthest (corner marker) and closest (center marker) to the center of the holder.
 - iii. Go to the center marker and use only X-Y translation stage to align the markers.
 - iv. Go to the corner marker and use only the turning knob to align.
 - v. Repeat from step iii until both markers are aligned.
- (g) Expose the sample at 3 mW for 80 sec.
- (h) Develop at 3:8 AZ400K.

- (i) Check if the contact windows are on top of the waveguides. If not, resist should be removed and process should be repeated.
- (j) Measure the photoresist profiles with Dektak. If trenches are not coated evenly, the process should be repeated with slower spinner speed.
- (k) Post-bake at 120 °C 2 min.
- (l) Prepare 1:7 HF:NH₄F in a polypropylene beaker.
- (m) Dip the sample in the HF solution for 2 min and rinse.
- (n) Check if oxide is removed cleanly, if not it should be etched more.
- (o) Remove the resist with acetone+IPA and blow dry.
- (p) Check the sample under the microscope. Below is the image taken after this step:

5. Metallization

We used two different metallization at this stage. Ti/Au 20 nm/200 nm adhere on SiO₂ well, therefore it facilitates wire bonding, however, Ge/Au based contacts are needed for an ohmic contact. Therefore, we used a two-stage metallization; first, only the top of the waveguides were coated with ohmic contact, then, the remaining area was coated with Ti/Au. Below is the steps for metallization:

- (a) Heat the sample at 110 °C for 1 min. Coat it with HMDS and spin.
- (b) Spin AZ5214 4000 rpm for 55 sec.
- (c) Align the first metallization mask for the ohmic contact.
- (d) Expose and develop with the same parameters.
- (e) Put the sample in the box coater and use the recipe:
 - i. 10 nm Ge
 - ii. 10 nm Au
 - iii. 6 nm Ge
 - iv. 23 nm Au
 - v. 10 nm Ni

vi. 50 nm Au

This sequence emulates Ge/Au alloy required for an ohmic contact.

- (f) Soak it with acetone at 50 °C for 30 min.
- (g) Check if the metal is removed properly under the microscope.
- (h) Repeat the steps from a, but with the recipe 20nm Ti/ 200 nm Au.

6. Electroplating

For better thermal dissipation and easier wire bonding, it is required to electroplate approximately 5 μm of gold. Below is the photo of the electroplating setup. We used a platinized titanium mesh as an anode and made a plexiglass cover and holder for the beaker. We measured the temperature while heating with a hot plate. We used a laboratory constant voltage source and monitored the current passing through the circuit.

- (a) Use carbon/silver paste to coat the copper mount.
- (b) Place the sample on the paste and wait for 5 min to dry.
- (c) Coat the edges of the sample with photoresist and wait for it to dry.
- (d) Pour 100 ml TSG-250 solution in the glass beaker.
- (e) Set hot plate to 120 °C. Wait for solution to reach at 60 °C.
- (f) Start stirring the solution at 500 rpm.
- (g) Set voltage source to 0.6 V.
- (h) Fine tune the voltage so that the current density will be 2 mA/cm².
- (i) In 10 minutes approximately 5 μm gold will be plated.
- (j) Clean the sample with acetone+IPA.
- (k) Anneal the sample on hot plate at 200 °C for 10 min.

7. Cleaving

We cut the lasers into 9 parts using the technique described at the first step. Laser cavity length is \approx 2-3 mm. Each part contains 10 laser waveguides.

8. Soldering

We designed various copper holders to solder the chips. Below are the steps for soldering:

- (a) Wash the copper mount using warm water and soap. Use abrasive paper to remove the oxide layer.
- (b) Put 200 ml concentrated phosphoric acid in a glass beaker.
- (c) Use crocodile clips to connect cables to the copper mount and another piece of copper.
- (d) Apply +7 V to the mount and ground the other copper. Wait for 2 minutes.
- (e) Rinse the copper mount with water. Now the surface should be clean and polished.
- (f) Coat the mount 20 nm Ti 100 nm Au.
- (g) Using a blade, cut a piece of indium foil slightly smaller than the chip.
- (h) Place the foil on the copper mount and using plastic tweezers gently push the foil, so that it sticks to the mount.
- (i) Put another small piece of indium elsewhere on the mount to monitor when it melts.
- (j) Place the sample on the copper foil without making contact with the facets.
- (k) Put the mount on the hot plate at 210 °C.
- (l) Wait until the small piece of indium melts. After it melts, wait for another 10 seconds and remove the mount and put it on a metal block to cool.
- (m) At this stage, front facets can be examined under the microscope. Facets should be clean for the laser to work. Due to the cleaving process, some facets have cracks on them and they do not lase.

B.1 Nextnano.QCL input file for InP949

```
<?xml version="1.0" encoding="utf-8"?>
<nextnano.QCL Version="1.1.5">
  <Header>
    <Author>Sinan Gundogdu</Author>
    <Content>
      This input file is modified from Thomas Grange's YuSST2010 file for calculation of InP949
      design
    </Content>
  </Header>
  <SweepParameters>
    <SweepType>Voltage</SweepType> <!-- SweepType: "Voltage" or "Temperature" -->
    <!-- Min, Max and delta values in mV for "Voltage", or in K for "Temperature"-->
    <Min unit="mV">20</Min> <!-- first/min voltage value in mV / period -->
    <Max unit="mV">500</Max> <!-- last/max voltage value in mV / period -->
    <Delta unit="mV">10</Delta> <!-- voltage increment in mV / period -->
  </SweepParameters>
  <Temperature unit="K">100</Temperature> <!-- Temperature of the lattice in Kelvin -->
  <Materials>
    <Material>
      <Name>In(x)Ga(1-x)As</Name>
      <Alloy_Composition>0.566</Alloy_Composition>
      <Alias>well</Alias>
      <Effective_mass_from_kp_parameters>yes</Effective_mass_from_kp_parameters>
    </Material>
    <Material>
      <Name>Al(x)In(1-x)As</Name>
      <Alloy_Composition>0.553</Alloy_Composition>
      <Alias>barrier</Alias>
      <Effective_mass_from_kp_parameters>yes</Effective_mass_from_kp_parameters>
    </Material>
    <NonParabolicity>yes</NonParabolicity>
    <UseConductionBandOffset>yes</UseConductionBandOffset>
  </Materials>
  <Superlattice>
    <Layer> <Material>well</Material> <Thickness unit="nm">2.9</Thickness></Layer>
    <Layer> <Material>barrier</Material> <Thickness unit="nm">2.7</Thickness>/Layer>
    <Layer> <Material>well</Material> <Thickness unit="nm">2.9</Thickness></Layer>
    <Layer> <Material>barrier</Material> <Thickness unit="nm">2.7</Thickness>/Layer>
    <Layer> <Material>well</Material> <Thickness unit="nm">3.1</Thickness></Layer>
    <Layer> <Material>barrier</Material> <Thickness unit="nm">2.3</Thickness>/Layer>
    <Layer> <Material>well</Material> <Thickness unit="nm">3.1</Thickness></Layer>
    <Layer> <Material>barrier</Material> <Thickness unit="nm">1.8</Thickness></Layer>
    <Layer> <Material>well</Material> <Thickness unit="nm">3.3</Thickness></Layer>
    <Layer> <Material>barrier</Material> <Thickness unit="nm">1.6</Thickness></Layer>
    <Layer> <Material>well</Material> <Thickness unit="nm">3.8</Thickness></Layer>
    <Layer> <Material>barrier</Material> <Thickness unit="nm">1.8</Thickness></Layer>
    <Layer> <Material>well</Material> <Thickness unit="nm">4.2</Thickness></Layer>
    <Layer> <Material>barrier</Material> <Thickness unit="nm">2.2</Thickness></Layer>
  </Superlattice>
</nextnano.QCL>
```

```

<Layer> <Material>well</Material> <Thickness unit="nm">4.4</Thickness></Layer>
<Layer> <Material>barrier</Material> <Thickness unit="nm">1.2</Thickness></Layer>
<Layer> <Material>well</Material> <Thickness unit="nm">5.1</Thickness></Layer>
<Layer> <Material>barrier</Material> <Thickness unit="nm">0.9</Thickness></Layer>
<Layer> <Material>well</Material> <Thickness unit="nm">5.5</Thickness></Layer>
<Layer> <Material>barrier</Material> <Thickness unit="nm">0.9</Thickness></Layer>
<Layer> <Material>well</Material> <Thickness unit="nm">5.8</Thickness></Layer>
<Layer> <Material>barrier</Material> <Thickness unit="nm">0.9</Thickness></Layer>
<Layer> <Material>well</Material> <Thickness unit="nm">2.0</Thickness></Layer>
<Layer> <Material>barrier</Material> <Thickness unit="nm">4.0</Thickness></Layer>
<Doping>
  <!-- homogeneous doping between starting and end point -->
  <!-- doping can be in barriers or wells or both -->
  <!-- origin = start of first barrier -->
  <DopingStart unit="nm">14.3</DopingStart> <!-- with respect to origin -->
  <DopingEnd unit="nm">24.8</DopingEnd> <!-- with respect to origin -->
<!-- Integer in order to choose how the doping density is specified:
... 0 = 2D equivalent density per period in [cm^-2]
... 1 = 3D doping density in the doped region in [cm^-3]
... 2 = Averaged 3D doping density over the whole structure in [cm^-3] -->
<Doping_Specification>1</Doping_Specification>
<Doping_Density>3e16</Doping_Density> <!-- Doping in units according to Doping_Specification
-->
</Doping>
</Superlattice>
<Scattering>
  <Material_for_scattering_parameters>well</Material_for_scattering_parameters>
<Interface_Roughness>
  <Amplitude_in_Z unit="nm">0.1</Amplitude_in_Z>
  <InterfaceAutoCorrelationType>0</InterfaceAutoCorrelationType> <!-- Correlation type:
0=Exponential, 1=Gaussian -->
  <Correlation_Length_in_XY unit="nm">8</Correlation_Length_in_XY>
  <Asymmetric_Interfaces>no</Asymmetric_Interfaces>
  <Amplitude_in_Z_Left>0.1</Amplitude_in_Z_Left>
  <Amplitude_in_Z_Right>0.2</Amplitude_in_Z_Right>
</Interface_Roughness>
<!-- Acoustic phonons -->
<Acoustic_Phonon_Scattering>no</Acoustic_Phonon_Scattering> <!-- Comment: Acoustic phonons
are in general not efficient - can be neglected in most cases -->
<AcousticPhonon_Scattering_EnergyMax>3.0</AcousticPhonon_Scattering_EnergyMax> <!-- Maximum
acoustic phonon energy -->
  <!-- Charged impurities -->
  <!-- Effective temperature of the electrons involved in electrostatic screening: 3 models
available -->
  <!-- model #1: Teff = T + Toffset * exp(-T/Toffset) with Toffset specified as
Temperature_Offset_parameter -->
  <!-- model #2: self-consistent calculation (requires several iterations of the all
calculation). The ccuracy specified by Accuracy_Self_consistent_Electron_Temperature -->
  <!-- model #3: Teff is directly specified by Electron_Temperature_for_Screening-->

```

```

    <Model_Temperature_for_Screening>1</Model_Temperature_for_Screening> <!-- integer 1,2 or 3
is required accordingly to the desired model -->
    <Temperature_Offset_parameter>140</Temperature_Offset_parameter> <!-- enter Toffset for
model#1 only such as Teff = T + Toffset * exp(-T/Toffset) -->
<Accuracy_Self_consistent_Electron_Temperature>0.05</
Accuracy_Self_consistent_Electron_Temperature> <!-- for model #2 only: self-consistent
calculation until the effective temperature convergences below the desired accuracy-->
    <Electron_Temperature_for_Screening>200</Electron_Temperature_for_Screening> <!-- for model
#3 only: the effective temperature is directly specified -->
    <ImpurityScattering_Strength>1.0</ImpurityScattering_Strength> <!-- 1.0 is the normal
physical calculation. Other values may be used for testing the importance of impurity
scattering. -->
    <Electron_Electron_Scattering>yes</Electron_Electron_Scattering>
<Alloy_scattering>yes</Alloy_scattering>
</Scattering>
<Poisson>yes</Poisson>
    <Lateral_motion>
        <Material_for_lateral_motion>well</Material_for_lateral_motion>
        <!-- Lateral energy spacing -->
        <Value unit="meV">40</Value>
    </Lateral_motion>
<Simulation_Parameter>
    <!-- PERIODS -->
    <Coherence_length_in_Periods>1</Coherence_length_in_Periods> <!-- 1 -> coherent transport
from one period to the next | N -> coherent transport between N+1 periods -->
    <!-- BASIS STATE CALCULATION -->
    <!-- parameters only affect the basis state calculation time. Not critical for total
calculation time. -->
    <!-- SPATIAL GRID -->
    <!-- defines number of grid points per period -->
    <Spatial_grid_spacing unit="nm">0.2</Spatial_grid_spacing>
    <!-- number of periods used for basis state calculation only: -->
    <!-- corresponds to 2N+1 k points per miniband -->
<Number_of_lateral_periods_for_band_structure>3</Number_of_lateral_periods_for_band_structure>
    <!-- number of grid points/period * (2N+1) should stay below ~10^4 for fast calculation
time -->
    <!-- ENERGY GRID -->
    <!-- critical for calculation time! -->
    <!-- It holds for higher temperatures: More broadening, i.e. less energy grid points are
sufficient. -->
    <Energy_grid_spacing unit="meV">2</Energy_grid_spacing> <!-- homogeneously spaced grid -->
    <Emin_shift unit="meV">0</Emin_shift> <!-- 0 is the default value - a negative value
increases the energy range of the Green functions towards low energies -->
    <Emax_shift unit="meV">0</Emax_shift> <!-- 0 is the default value - a positive value
increases the energy range of the Green functions towards high energies -->
    <Energy_Range_Lateral unit="meV">250</Energy_Range_Lateral> <!-- xy-direction, evaluated from
lowest state -->
    <Energy_Range_Axial unit="meV">400</Energy_Range_Axial> <!-- z-direction, evaluated from
lowest state/miniband -->

```

```

<!-- The self-consistent loop ends successfully if the 2 following convergence factors are
reached for the lesser Green's function and the current (relative difference between two
consecutive iterations) -->
<Convergence_Value_GF>1e-4</Convergence_Value_GF>
<Convergence_Value_Current>1e-4</Convergence_Value_Current>
<!-- Number of maximum iterations if the above convergence values are not reached -->
<!-- Higher values give more accurate results. -->
<N_max_iterations>1000</N_max_iterations>
</Simulation_Parameter>
<Output>
  <!-- In order to output 2D energy resolved graphs-->
  <EnergyResolvedPlots>yes</EnergyResolvedPlots>
<EnergyResolvedPlots_MinimumEnergyGridSpacing>2.0</EnergyResolvedPlots_MinimumEnergyGridSpacing>
  <!-- Energy resolved gain for a specified photon energy-->
  <EnergyResolved_Gain>yes</EnergyResolved_Gain>
</Output>
<Gain>
  <!-- GainMethod:
          -1 .. no gain calculation
           0 .. gain without self-consistency only
           1 .. gain with self-consistency only
           2 .. gain with and without self-consistency
  -->
  <GainMethod>1</GainMethod>
  <!-- without self-consistency: -->
<dE_Phot unit="meV">2</dE_Phot> <!-- energy spacing between two photon energies -->
  <Ephoton_Min unit="meV">100</Ephoton_Min>
<Ephoton_Max unit="meV">170</Ephoton_Max>
  <!-- with self-consistency: -->
  <dE_Phot_Self_Consistent unit="meV">2</dE_Phot_Self_Consistent> <!-- energy spacing between
two photon energies -->
  <Ephoton_Min_Self_Consistent unit="meV">100</Ephoton_Min_Self_Consistent>
  <Ephoton_Max_Self_Consistent unit="meV">170</Ephoton_Max_Self_Consistent>
  <MaxNumber_SelfConsistent_Iterations>1000</MaxNumber_SelfConsistent_Iterations>
  <ConvergenceFactor_Gain_SelfConsistent>1e-4</ConvergenceFactor_Gain_SelfConsistent>
  <!-- Calculation of gain only between the following values of potential drop per period -->
  <Vmin unit="mV">100</Vmin>
  <Vmax unit="mV">500</Vmax>
</Gain>
</nextnano.QCL>

```